WELL-BALANCED AND CONSISTENT ALGORITHMS FOR THREE-DIMENSIONAL SIMULATIONS OF BINARY IMMISCIBLE FLOWS

A thesis submitted in partial fulfillment of the requirements for the degree of

DOCTOR OF PHILOSOPHY

By

JAI MANIK

DEPARTMENT OF MECHANICAL ENGINEERING
INDIAN INSTITUTE OF TECHNOLOGY GUWAHATI
GUWAHATI - 781 039, INDIA
November 2017

WELL-BALANCED AND CONSISTENT ALGORITHMS FOR THREE-DIMENSIONAL SIMULATIONS OF BINARY IMMISCIBLE FLOWS

A thesis submitted in partial fulfillment of the requirements for the degree of

DOCTOR OF PHILOSOPHY

By

JAI MANIK
(Roll Number: 11610329)

DEPARTMENT OF MECHANICAL ENGINEERING
INDIAN INSTITUTE OF TECHNOLOGY GUWAHATI
GUWAHATI - 781 039, INDIA
November 2017

CERTIFICATE

It is certified that the work contained in the thesis entitled **"Well-balanced and consistent algorithms for three-dimensional simulations of binary immiscible flows"**, by **Jai Manik** has been carried out under my supervision and that this work has not been submitted elsewhere for a degree.

November 2017

(Amaresh Dalal)
Associate Professor
Department of Mechanical Engineering
Indian Institute of Technology Guwahati

ABSTRACT

With a view to compute three-dimensional multi-component fluid flows in complex geometry encountered in many industrial applications, a novel finite volume method over hybrid unstructured meshes is proposed for the solution of the Navier-Stokes and advection equations. Among the several numerical approaches put forward by various research groups, finite volume method over unstructured meshes offers a promising technique for simulating fluid flow problems in a complex domain. Multi-component fluid flow problems, in particular those involving two fluids distinguished by sharp interface are of practical importance in many engineering applications including mould filling, liquid sloshing, pipeline drainage and fuel injection in an internal combustion engine etc.. Although a considerable amount of work has already been carried out to simulate the multi-component flows, efforts are still going on to handle the complexities associated with different phases. The challenges are mainly due to the jump in fluid properties, the presence of interfacial and large body forces. With the passage of time, a class of algorithms based on force balancing have been evolved. The primary concern of these algorithms is to discretely treat the forcing terms in an identical way. In the recent past, methodologies has been proposed for achieving force balancing over uniform/non-uniform structured meshes, but work on hybrid unstructured meshes is limited.

Considering the aforementioned fact, the present doctoral thesis focuses on the development of a generalized robust computer code for simulating binary fluid flow problems having large property variations across the interface over three-dimensional hybrid unstructured meshes that can handle different types of source term in a simple and efficient way. The code development started from the scratch. Starting from pure diffusion, convection-diffusion, then Navier-Stokes solver is validated against several benchmark problems. The final developed solver for binary fluid flow problems is the outcome after several rigorous testing at different stages during the development of the solver. A hybrid mesh is used with a collocated arrangement of the dependent variables. The diffusion fluxes are computed in a novel and natural way and the pressure-velocity decoupling is avoided by using momentum interpolation. In order to maintain the phase interface as sharp as possible,

separate testing has been performed for volume fraction equation. In the transport equation for the volume fractions, the convective term plays a major role. Knowing the fact that upwind scheme suffers from numerical diffusion and the higher order schemes (central differencing) results in numerical dispersion, in the present solver, high resolution scheme including CUBISTA and CUIBS has been implemented and tested over unstructured meshes. In order to validate the methodology and the computer code, several benchmark problems have been solved. The predicted results are compared with those available in literature. The comparisons are satisfactory.

Working within the algebraic volume of fluid framework, the initial efforts were on the development of a well balanced formulation within a collocated arrangement of variables over hybrid unstructured meshes. Knowing the fact that there is a sharp jump in material properties across the interface, a least squares based gradient calculation technique has been adopted. The benefit of least squares method over the traditional Green Gauss method lies in the fact that the cell centroid gradient is reconstructed from the respective values of gradients at each of its faces. Employing the least squares method and considering all the competing forcing terms in the pressure Poisson equation, actually resulted in a well balanced algorithm, which is then tested and validated against various problems. Apart from these discrete force balancing, we also looked on to the effect of using similar and dissimilar convective schemes among different equations and termed them as consistent and inconsistent treatment, respectively. It has been noticed that, for the problems including the well known static droplet, static tank, filling of a column, convection of an inviscid droplet and the benchmark case of rising of a bubble, the consistent treatment together with the well balanced algorithm gives correct results for almost every cases irrespective of the density ratio chosen.

Subsequently, an alternative approach for binary fluid flows has also been developed, which is based on a variant of the traditional Green Gauss approach. This methodology, which is referred to as modified Green Gauss method is an interpolation free approach and the implementation of this method is relatively easy as compared to the least squares method. The resultant gradient obtained with this approach is as accurate as those of the outcome of least squares based balanced force strategy as described earlier. To demonstrate the ability of the balanced force algorithm described in this particular work, wherein both least squares and modified Green Gauss have been employed, several test cases both in two- and three-dimensional have been carried out over orthogonal and non-orthogonal unstructured meshes. Typically, test cases involving marangoni stresses, surface tension forces, gravity in hydrostatic and piezometric formulation have been solved and results show the proper achievement of force balancing even on unstructured meshes. Later, the solver has also been validated for three dimensional problems whose experimental and numerical data are available in the literature. These include the impingement of a droplet over thin liquid film and dam break over an obstacle. The results show

a reasonably good agreement with the published data.

In the next part of the thesis, the algorithm has been applied to solve two pertinent problems related to two-components fluids.

Firstly, the dynamics of droplet dripping and detachment process from a horizontal solid substrate have been simulated numerically. This problem finds application in the fuel cell technology. The investigations have been carried out to explore the fascinating dynamics of droplets by studying the effect of various parameters including density ratio, viscosity ratio, surface wettability, Weber number (We) and the presence of surrounding droplet. It has been observed that, for the cases having low density ratio together with lower value of We number, force due to gravitational pull is not sufficient enough to overcome the effect of wall adherence, leading to the sticking of droplet on the surface itself. However, later in the study it has been shown that the same droplet which remained stick to the surface, got detached from the wall, when the We number is increased or if the wall wettability is changed or with the merger occurring due to the presence adjacent droplet.

In the second problem, the dynamics of the droplet impingement over thin liquid film with varying thickness has been considered. This problem is a subject of interest to spray coating industries. The thickness of the film has been varied by considering a sinusoidally varying bottom wall with an amplitude of 0.5. It has been observed that, in comparison to the base case (straight horizontal surface), the velocity with which the crown is spreading actually get decreased when the bottom wall is considered to vary sinusoidally. Similar behavior has been observed irrespective of the location of drop fall i.e. either falling over crest or over the trough. Also it has been noted that, in the case when droplet is falling over crest, the thickness of the lower portion of the crown rim also gets increased. Apart from these, the effect of droplet impingement at an angle has also been explored. Two different angles have been considered and the results are then compared with the case when droplet hits the liquid film vertically.

Finally, the thesis concludes with a summary of the main findings and recommendations for future work.

Dedicated to my Mother

Acknowledgements

If I would have worked single-handedly on the research reported in this thesis, I would have never been able to complete it. Herein, I would like to acknowledge the help and support of various people during the last six years of my stay at IIT Guwahati.

First of all, I would like to express my sincere gratitude towards my supervisor Dr. Amaresh Dalal for his continuous support and guidance during my thesis work. His advice has been invaluable on both an academic and a personal level, for which I am extremely grateful. Also, I must acknowlwdge his kind and amicable nature which takes away our worries within seconds. The words can never be enough to thank his kindness.

I am also highly indebted and grateful to Dr. Ganesh Natarajan for being ever so kind to show interest in my research and for giving his precious and kind advice regarding the topic of my research. His knowledge in this field and the discussions which I had with him have truly helped me to improve my work. Also, his passionate approach in doing numerical science truly inspires me and is worth emulating.

I would also like to acknowledge helpful suggestions from my doctoral committee members: Dr. Anoop K. Dass, Dr. Arnab Kumar De and Dr. Subrata K Majumder. My special thanks goes to the faculty members of our department with whome I learnt the basics of fluids and thermal engineering. I would like to make a special mention about an advanced course on CFD taught by Dr. Arnab Kumar De. His strictness and the rigorous lab sessions made me to overcome my coding fear. I also extend my thanks to the individuals in the Department who have helped me one way or another. In addition to this, I would also like to acknowledge the partial funding provided by DAE-BRNS, Government of India.

These acknowledgements would not be complete without mentioning my research lab colleagues: Mukul, Subrat, Preeti, Vinod, Saurabh and all the M. Tech students of Anupravaha lab. It was a great pleasure working with them. Special thanks goes to my seniors Dr. Pitambar Randive and Dr. Sathisha H. M. with whome I spent my early days of research. I never felt the need to ask for their help, because they were always been there before I even had to ask. I would also take this as an opportunity to thank Mrs. Dalal for providing us a homely atmosphere here in the IITG Campus away from home.

I am also grateful to the numerous people who have through shared experiences become both my colleagues and my friends. Specially Dr. Vijay Mishra and Dr. Mohitlal Sahu, their hands on my shoulder is ever comforting.

Finally, I take the opportunity to thank the almighty and my family members for each and every thing they did for me. Specially my mother, for her I don't know where to start and what to say. Thank you is a very small word for all the sacrifices she made for me. I can never thank God enough for blessing me a mother like her.

Jai Manik

Contents

List of Figures

List of Tables

Nomenclature

English Symbols

Symbol	Definition
f	Volume fraction
Fr	Froude number
$\mathbf{g}$	Gravitational vector
p	Pressure
Re	Reynolds number
$\mathbf{S}_f$	Surface area vector
$\mathbf{u}^*$	Provisional velocity
u, v, w	Velocity components in x, y, z directions respectively
V_P	Volume of cell P
We	Weber number
x, y, z	Cartesian coordinates
$\mathbf{x}$	Vector quantity
$\hat{\mathbf{x}}$	Unit vector

Greek Symbols

γ	Density ratio
κ	Interfacial curvature
μ	Dynamic viscosity
ρ	Density
σ	Coefficient of surface tension
ϕ	General variable representing u, v, T

Subscripts

b	Value at the boundary face
C	Refers to upwind grid point
D	Refers to downwind grid point
f	Value at cell face
N	Value at the centroid of neighbor cell
P	Value at cell centroid of a cell
U	Refers to far upwind cell

Abbreviations

CDS	Central differencing scheme
CLSVOF	Combined level set and volume of fluid
LS	Level set
SCLSVOF	Simple coupled level set and volume of fluid
UDS	Upwind scheme
VOF	Volume of fluid
VOSET	Coupled volume of fluid and level set

Chapter 1

Introduction

Multiphase flows are encountered in various industrial applications including spray painting, ink-jet printers, condensation/removal of liquid droplets from fuel cells, mould filling, liquid sloshing, pipeline drainage, fuel injection in an internal combustion engine and control of droplet size in pesticide spray etc.. In order to simulate these complex three-dimensional fluid flow problems numerically, a fast, robust, accurate and generic solution methodology is needed. Among the several approaches put forward by researchers, unstructured finite volume methods offer a cost effective alternative. Unlike structured curvilinear meshes, unstructured meshes are easier to generate over complex configurations. These meshes may also be locally refined to increase the solution accuracy at selective regions and are ideal to handle complicated geometries with relative ease. The flexibility associated with unstructured grids allows the construction of hybrid meshes as well. While unstructured grid generation manages the complex geometry, it is imperative to develop a multiphase flow solver that can handle arbitrary polyhedra resulting from such meshes in an efficient and generic manner.

Multiphase flows based on the phases involved are broadly classified as gas-liquid (bubbly flows, slug flows), liquid-solid (slurry flow, sedimentation transport) and gas-solid flows (particle laden flow, fluidized bed), while on the basis of flow configuration they are classified either as dispersed flow or as a separated flow. Binary fluid flow, in particular, is a separated flow and is described by the simultaneous flow of two fluids distinguished by a sharp interface. The interface separating the

two phases is deformable and it can account for topological changes due to breakup and coalescence. The prediction of binary fluid flow is beneficial in process design or in the diagnosis of problems in an established process. Although a considerable amount of work has already been carried out to simulate the binary fluid flows correctly, efforts are still going on to handle the complexities associated with different phases. The difficulties are mainly due to the following issues,

1. fluid properties may change across the interface substantially,
2. the presence of interfacial and large body forces,
3. the interface location has to be captured/tracked as it evolves,
4. the sharpness of the interface has to be maintained throughout the computations.

Considering the aforementioned challenges, in the past, various interface capturing techniques have been proposed together with the focus on handling large body forces in the context of practical and realistic density and viscosity ratios. We now present a detailed literature survey on these methodologies to simulate binary fluid flows.

1.1 Review of Literature

In this section, initially we present a detailed literature on the techniques available to capture the interface followed by the a comprehensive outlook on the available balanced force algorithms. Later in this section, we also present various available literatures on the droplet detachment process as well as on the impingement of droplet over thin liquid film.

1.1.1 Interface capturing techniques

A majority of the current research in modelling interfacial flows adopts either the volume of fluid (VOF) method [7, 8, 9], the level set (LS) method [10, 11, 12] or hybrid variant of the two, such as CLSVOF [13], SCLSVOF [14] and VOSET [15]. The VOF method is essentially an Eulerian approach to track the phase interface

which can account for various topology changes including merging and breakup. In this method, the value of volume fraction function f varies between zero and unity. The value of f is unity for the computational cells fully occupied by fluid 1 and for the cells which are fully occupied by fluid 2, its value is zero. The value of f in computational cells through which interface passes lies in-between zero and unity. This method is again broadly classified into two groups, one with the geometric reconstruction of the interface (line in 2D and plane in 3D), while in the other method the volume fraction equation is directly solved with special attention given to reduce the amount of numerical diffusion and numerical dispersion associated with various convective schemes. The former approach is the traditional VOF, while the later method is commonly known as algebraic VOF.

Different interface-reconstruction schemes have been developed in the past. The first algorithm is being described by DeBar [16] and later by Noh and Woodward [17], who named their method as SLIC (for simple line interface calculation). Shortly after the introduction of the SLIC method, a piecewise constant/stair-step VOF method was proposed by Hirt and Nichols [18], who were the first to propose the term "volume of fluid". In these methods, interfaces are forced to align with mesh coordinates, but are additionally allowed to "stair-step"within each cell.

A major contribution in VOF methods was later made by Youngs [19], where, a truly piecewise linear approximation to the interface has been developed. Each interface line within a cell is denoted by a slope and an intercept. This method is mainly called as PLIC (for piecewise linear interface calculation). Several other methods for interface construction have also been developed such as piecewise parabolic reconstruction by Renardy et al. [7], and piecewise spline reconstruction by Ginzburg et al. [20]. Scardovelli and Zaleski [21] developed interface reconstruction methods based on a least squares fit. These methodologies are primarily based on Eulerian advection of volume fractions f on Cartesian meshes with either a split scheme or an unsplit scheme. However, one can find considerable difficulties while implementing these schemes on unstructured grids.

In the second approach, the governing equation for the transport of volume fraction is meticulously treated so as to reduce the numerical diffusion associated with different convective schemes. In the past, various high resolution schemes have been

proposed to capture the interface as sharp as possible. Recently, attempts have been made to use a combination of high resolution scheme together with a compressive scheme, which not only preserves the sharpness of the interface, but also is easier to implement even on unstructured meshes.

The initial attempts began with the work of Ubbink and Issa [22] and Jasak et al. [23]. They proposed a high resolution scheme for accurately capturing the phase interface on arbitrary meshes. Ubbink and Issa [22] proposed CICSAM (Compressive Interface Capturing Scheme for Arbitrary Meshes) scheme, while Jasak et al. [23] named their scheme as GAMMA. The former method modified the ULTIMATE-QUICKEST scheme, while the later method used a combination of CDS (central difference scheme) and UDS (upwind scheme) as a base for the prediction of normalized face values. These are based on the finite volume technique and are fully conservative. The method proposed in both of these works are capable of handling interface rupture and coalescence.

In order to improve the iterative convergence properties, Alves et al. [24] proposed a scheme called Convergent and Universally Bounded Interpolation Scheme for the Treatment of Advection (CUBISTA). The enhancement in iterative convergence properties is achieved by incorporating total variation diminishing constraints into the scheme.

A novel approach of blending high resolution scheme with a bounded downwind scheme has been put forward by Tsui et al. [25]. They reported that, their scheme, named as FBICS (Flux-Blending Interface-Capturing Scheme), performed better when compared against the outcome of CICSAM and HRIC. Also, their method maintains the high accuracy performance for Courant number upto 1. Another scheme, by the name STACS, was proposed by Darwish et al. [26]. It is also based on the switching strategy. The result has been compared with different high resolution schemes and it is reported that the results obtained by employing their scheme are far more accurate and less diffusive at all Courant number. Cassidy et al. [27] recently presented an overview of interface steepening schemes based on compressive flux formulations. They primarily focused on algebraic interface-capturing strategies that fit directly within a finite volume MUSCL-type framework.

Recently, So et al. [28] proposed anti diffusive method to control the amount of diffusion occurred while transporting volume fractions. In addition to the other governing equations for binary fluid flows, they solved an additional equation just after the transport of volume fraction. The strategy was then tested over two and three-dimensional structured and unstructured meshes. Another work in the direction of employing the blending of a high resolution scheme together with the bounded downwind scheme is proposed by Patel and Natarajan [29]. Their work presents necessary guidelines to design and develop interface capturing schemes in a unified framework.

Apart from the above mentioned VOF methods, another class of methods under the aegis of level set method have also gained much popularity in the scientific community. The method was first introduced by Osher and Sethian [30] and later it has been employed by Sussman et al. [31] to simulate immiscible binary fluid flows. The level set method employs a signed distance function to identify the two different fluids and a zero level set is assigned to the interface itself, while the VOF uses the concept of volume fraction. The former suffers from mass conservation issues unlike the later, but the distance function allows for a more smoother variation of properties across the interface compared to the volume fractions. More sophisticated and mass conserving versions of level set method have also been proposed by various research groups. One can find a detailed description about these methods in [32, 33, 34].

Due to the individual short comings of various methods, attempts have been made to combine the strength of different methods and approaches such as CLSVOF [13], VOSET [15], SCLSVOF [35] and many more had been put forward. In particular, CLSVOF [13] method combines some of the features of the volume of fluid method with the level set method. The resulting hybrid method showed better performance in comparision to either method alone. Their computational examples stressed mainly on flows in which surface tension forces and features such as changes in topology are dominant. Several articles on CLSVOF can be found in [36, 37, 38, 39, 40, 41]. Another hybrid method has been proposed by Aulisa et al. [42] as mixed marker and volume of fluid method for two phase and free boundary flows. Menard et al. [43] also proposed coupled level-set/VOF/ghost fluid methods for simulating primary break-up of a liquid jet. Similarly, various other hybrid methods can be found in [44, 45, 46].

Along with this, other popular approaches including lattice Boltzmann and diffuse interface methods also find considerable attention among the research community. In particular, Bao and Schaefer [47] have proposed a novel approach using lattice Boltzmann method for simulating high density ratio multi component multiphase flows. Similarly, Ding et al. [48] conducted the investigations on the applicability of the diffuse interface method for simulating binary fluid flows with large property variations.

1.1.2 Balanced force algorithms

The modelling of surface tension forces and body forces play a major role in simulations of multiphase flows. The most common approach to handle interfacial tension is to employ the CSF (continuum surface force) model of Brackbill et al. [49], which converts the singular interfacial force into a volumetric force acting in a small region in the vicinity of the interface. There are also other approaches such as the ghost fluid method [50] and continuum surface stress method [51, 52] to handle surface tension force.

Simulating interfacial flows using CSF approach relates to its implementation, that can generate spurious currents unless special care is taken during discretization. One of the potential sources of the spurious currents is the numerical imbalance between the surface tension force and the pressure gradient at the discrete level. With the passage of time, a class of algorithms based on force balancing have been evolved. The primary concern of these algorithms is to discretely treat the forcing terms in an identical way. In this regard, Francois et al. [53] proposed a balanced force algorithm within the VOF framework on Cartesian meshes. They incorporated both the sharp representation of surface tension force and the continuous surface tension force into their balanced force framework and showed that machine zero values of spurious currents could be achieved for a known constant curvature at the interface. Based on their balanced force framework, Herrmann [54] presented a balanced force refined level set grid method over structured and unstructured meshes [54]. This work employed the force balancing concept in conjunction with level set method with a novel least squares approach [55] which is used to construct gradients at cell

centers, thereby it captures the necessary force balance. Mencinger and Žun [56] also emphasized on the need for achieving force balancing at the discrete level and demonstrated the strength of their algorithm by numerically simulating stationary and moving bubble.

The second source of spurious currents in interfacial flow studies is due to the calculation of curvature, which cannot be completely eliminated but can be minimized by employing more accurate approaches to evaluate interface curvature. While the simplest approach for curvature calculation was proposed by Ubbink [22], more accurate methods have been devised in the recent past, which include using height functions [57, 58] and higher order accurate gradients [59].

The handling of body forces does not pose as much difficulties as that of the interfacial tension. It is however easy to see that the lack of discrete balance between body force and pressure gradient can lead to spurious currents [60] and therefore one needs to carefully treat the body force terms at the discrete level as well. Montazeri and Ward [61] have shown that the definition of piezometric pressure as opposed to hydrostatic pressure is the ideal way to treat gravity in a balanced force framework. The traditional method of cell centroid gradient calculation, as shown in the work of Dalal et al. [62], is prone to produce force unbalancing for multiphase flows. In order to achieve perfect balancing, the cell centroid quantities should be reconstructed from the respective face values. In these lines, Perot [63] had shown the reconstruction of cell centroid velocity vector using the face normal velocities. This centroidal quantity calculation from the respective face values has been named as MGG in the present work.

An equally important challenge for multiphase flow solver is the need to handle large and realistic density and viscosity ratios of the associated fluids and the authors believe that there has been little emphasis on this topic in the framework of VOF/level set methods. The earliest effort in this direction came from Rudman [57], who used dual grids to enforce a consistent transport of mass and momentum. Bussmann et al. [64] modified this approach for unstructured meshes to handle large density ratio flows. Recently, Ghods and Herrmann [65] as well as Denner and Van Wachem [59] have proposed algorithms on structured and unstructured collocated meshes to handle fluid flows with arbitrary large density ratios. In particular,

the framework in [65], proposed a consistent rescaled momentum transport method, where the same volume flux is used in transporting density and momentum. They employ level set method to handle interfaces and recompute the density fields from level set equation, thereby incurring finite but identical conservation errors in mass and momentum.

Apart from the focus on solver development activities (which are indeed a primary forcus of the present work), we would also like to study the behavior of droplet under various circumstances. In the following two subsections, we present a detailed literature review on the droplet dynamics in two different scenarios.

1.1.3 Droplet detachment from a solid substrate

Droplet detachment process is a crucial phenomenon occurring in various engineering applications including spray painting, ink-jet printers, condensation/removal of liquid droplets from fuel cells, self cleaning or lotus effect and control of droplet size in pesticide spray etc [66, 67, 68]. Although, the behavior of liquid droplets over solid surface appears to be a simple phenomenon, but the complexities arise due to the movement of contact line (intersection of liquid-liquid interface on to the solid surface). A considerable amount of literature can be found out on studies including droplet dynamics using experimental, theoretical as well as numerical techniques. Droplet behavior over solid surfaces depends on various factors including density ratio, viscosity ratio and surface conditions etc. In particular, surface wettability plays a major role on the droplet motion over solid substrate. For hydrophobic surface, liquid droplet has less affinity towards it and hence the droplet tries to leave the surface, while for hydrophilic surface, liquid droplet tries to wet it out.

In the past, various numerical studies have been performed to reveal the fascinating dynamics of droplets. Schleizer and Bonnecaze [69] studied the behavior of a two-dimensional droplet placed between two parallel plates. The droplet in their case is attached to the lower plate and the study was performed for various capillary numbers, viscosity ratio, surface wettabilities and droplet sizes. Kang et al. [70] also studied the dynamics of a two-dimensional droplet, but instead of simulating inside a pressure driven channel, they studied the droplet behavior considering the effect of gravitational pull, which was however neglected in the study of Schleizer

and Bonnecaze. To account for different wall wettabilities, Kang et al. [70] has employed a static contact angle model. Various other models have also been proposed in the past to predict the moving contact lines. In this regard, Sui et al. [71] has presented an exhaustive review on the availability and applicability of different contact angle models. Similarly, a comparitive study of various dynamic and static contact angle models has been presented by Legendre and Maligo [72]. In a dynamic contact angle model, the contact angle is usually a function of contact line velocity (Cox [73], Afkhami et al. [74]), whereas, in a static contact angle model, a geometric relation has to be satisfied at the contact point.

Effect of wettability gradients and superhydrophobicity on the droplet displacement process inside a vertical channel has later been considered by Randive et al. [75]. They showed that at higher capillary number and for superhydrophobic surfaces, the droplet does not break while detaching from the surface. Again, Randive et al. [76] numerically studied the effect of inclined channel on the droplet behavior. Their study revealed that the influence of channel inclination is more significant on hydrophobic surface as compared to hydrophilic surface. Later, Norman and Miksis [77] used level set method to track the motion of a two-dimensional bubble inside an inclined channel. They showed that there exists a critical angle of inclination, beyond which the bubble dynamics changes from bouncing to steady rising. Again, level set method was used by Spelt [78] in order to examine the behavior of a pinned or moving two-dimensional droplet subjected to shear flow. For the case, when the droplet is pinned, their study revealed the existence of a critical Weber number beyond which the droplet does not remain steady and this critical Weber number depends on the value of Reynolds number. Ahmed et al. [79] presented a mathematical formulation describing the spreading characteristics of the droplet over inclined surfaces. They also considered some special situations where the droplet splits to yield satellite droplets while moving down an inclined plane. Lately, Zhang et al. [80] performed various numerical studies over a two-dimensional drop placed inside a channel for varying Re and Ca numbers. The study was concluded by presenting a curve on Re-Ca plane, depicting the zones where either steady/oscillatory translation or breakup of the droplet will occur.

Apart form these wall bounded droplet examinations, several authors have focussed on the droplet dripping process from a nozzle. Zhang and Basaran [81]

performed an experimental study to elucidate the dynamics of droplet formation through a vertically placed nozzle. Their results showed that the length of the liquid bridge before the droplet pinch-off depends on various parameters including drop viscosity, flow rate of the liquid and outer radius of the nozzle. Later, Henderson et al. [82] revealed that the actual droplet pinch-off takes place after the formation of secondary liquid thread and not by the instabilities of the primary liquid thread. They also reported that the speed with which the liquid bridge recoils nearly follows a power law.

Liquid removal through the gas diffusion layer in fuel cells is a critical process and its numerical investigations can be found in [83, 84, 85, 86]. Zhu et al. [84] in particular reported the effect of channel geometry and pore size on the removal of liquid from gas diffusion layer. The study was performed in two-dimensions using volume of fluid method. They also considered single and double pores geometrical arrangements through which the water droplets emerge. An increase in the removal of droplets from the micro-channel has been reported for the geometry having two pores. Cho et al. [66] presented an analytical expression for the droplet deformation and its detachment velocity inside a micro gas flow channel. The analytical solutions were compared against numerical and experimental findings as well. A relatively smaller deformation of the droplet has been reported for lower velocities. Dimitrakopoulos and Higdon [87] numerically investigated the yield condition of a two-dimensional droplet placed over a solid substrate in the presence of gravitational body force. They showed the dependence of critical shear rate on various factors including viscosity ratios, capillary number, Bond number and contact angles.

Surfaces in nature sometimes exist with significant wettability gradient and thus there exist numerous studies wherein, wettability gradient has been considered. Huang et al. [88] conducted several numerical experiments in two-dimensions to reveal the behavior of droplet over a surface with stepwise wettability gradient. Effect of Reynolds number, viscosity ratio and wettability gradient were considered and it is shown that in majority of the cases, the droplet initially got some acceleration, but ultimately, it reached a steady state. Zu and Yan [89] used lattice Boltzmann method to study the spreading characteristics of a three-dimensional droplet over a partial wetting surface. Their method could actually predict the results for a binary fluid flow with a density ratio of 1000. Using different arrangements of

the hydrophobic surfaces, they observed various phenomenon including spreading, breakup and also the droplet migration. With the single hydrophobic strip arrangement, the droplet breaks up into two part, whereas, with a cross strip arrangement, the droplet took the shape of four-leaved flower. Again, lattice Boltzmann method was used by Randive et al. [90] to study the effect of channel geometry on the mobilization of trapped blob. They observed that, when the surfaces are hydrophobic in nature and the channel geometry is uniform, maximum displacement of the blob occurs.

The effect of the contact angle on the behavior of a buoyancy driven liquid droplet placed over a wall was later studied by Lamorgese and Mauri [91]. They used phase field method and reported that for hydrophilic surfaces, the droplet detaches after the formation of double cone like structure, while for hydrophobic surfaces, only a single cone structure is formed before the droplet pinch-off. Recently, Tilehboni et al. [92] studied the behavior of a single droplet, placed on either top (ceiling) or side wall. They performed various studies over hydrophobic as well as hydrophilic surfaces and also reported the effect of Evotos number on the droplet shape. They reported that, at lower contact angles ($\theta < 45°$) together with the lower values of Evotos number, the droplet remained stick to the ceiling. However, if the Evotos number is increased beyond a certain limit, keeping other parameters constant, the droplet will ultimately get detached from the ceiling.

1.1.4 Droplet impingement studies

Droplet impact on dry and wet surfaces finds application in various industrial processes and natural phenomenon. Some important engineering applications include ink-jet printing, spray cooling on hot surfaces, spray coating and fuel injection in internal combustion engines. The behavior of droplet impact over a thin liquid film is a complex phenomenon with strong interface deformations, which may sometimes result in the formation of multiple secondary and tertiary droplets. In this regard, Cossali et al. [93] performed experimental studies on the impact of a single droplet over wetted and solid surfaces. They proposed a correlation for determining the splashing/deposition limit and showed that the accuracy of this limit is around 10 % when compared with their experimental findings. Also, in accordance

with the theoretical predictions of Yarin and Weiss [94], they confirmed that the increase in the radius of the crown is directly proportional to the square root of the physical time. Later, Weiss and Yarin [95] numerically investigated the splashing phenomenon using boundary-integral method. In their simulations, they considered the surface tension and gravitational forces, but the effect of viscosity was not taken into account. For the drop impact over deep liquid pools together with lower impact velocity of the drop, they observed the entrapment of tiny bubbles. While, for the impacts with much larger velocities over shallow liquid films, a crown rim has been observed whose radius increases with the increase in time.

The effect of Weber number and film thickness on the evolution of crown diameter and its height was later been studied by Cossali et al. [96] experimentally. They found out that the crown height has a strong dependence on the impact velocity but at the same time, it is very weakly dependent on film thickness. In order to investigate the effect of drop viscosity on the splashing dynamics, Nikolopoulos et al. [3] performed axisymmetric numerical simulations using volume of fluid method. They reported that there is a marginal effect of drop viscosity during initial stages of crown formation, but later, its effect can not be neglected. Mukherjee and Abraham [97] employed lattice Boltzmann method for studying the effect of gas density and its viscosity on the formation of crown. Their simulations revealed that the rate with which the crown radius increases, gets reduced with the increase in either the density or viscosity of the surrounding medium. Shetabivash et al. [98] also performed axisymmetric numerical studied to explore the effect of gas density and viscosity on the crown formation. In addition to this, they also investigated the effect of initial shape of the droplet just before the impact. They observed that the rate of increase of crown radius is increased when the droplet shape is prolate just before impact.

Apart from the above mentioned studies wherein the droplet hits the film perpendicularly, few literatures are also available on the oblique impact of the drop. Zhbankova and Kolpakov [99] conducted numerous experiments for finding out the dependence of coalescence probability on the Weber number as well as on the angle of impact. They observed various phenomenon including bouncing and coalescence, but due to the use of lower Weber number in their studies, no splashing had been observed. Focusing on this droplet splashing during an oblique impact, Okawa et

al. [100] experimentally investigated the effect of droplet impact angle on the production of secondary droplets. They observed the formation of secondary droplet only for lower values of impingement angle and when the angle is increased beyond 70°, no secondary droplet has been noticed. In all the aforementioned oblique impact studies, the impingement angle was varied in between 0°-75° only. In order to explore the crown dynamics for even higher impact angles, Ray et al. [101] numerically simulated the oblique impact of droplet over deep and shallow liquid in two-dimensions. They performed the simulations for a very high value of impingement angle even upto 90°. Recently, Cheng and Lao [102] employed lattice Boltzmann method for studying the dynamics due to oblique impact over thin films in three dimensions. They observed the suppression of the splashing on the downstream side of the crown formation when the angle of impact is increased beyond a critical value.

Considering all the above mentioned literatures (balanced force algorithms, studies on droplet detachment and its impingement over thin liquid film), we now discuss about the motivations of the present thesis.

1.2 Motivation

A careful study of the literature presented in the previous section reveals that there are certain issues regarding the development of a well balanced formulation over unstructured grid for simulating binary fluid flows. It has been noticed that, either the algorithms developed so far are proposed on Cartesian meshes or the types of source term considered in their work is very limited. Also, very less attention has been given to the algorithm development over hybrid unstructured meshes using algebraic volume of fluid method. However, in the majority of industrial oriented multiphase flow problems, the flow domains are complex in nature and hence, in order to save time for meshing, unstructured grid flow solvers are usually adopted. This is where the motivation to develop a robust binary fluid flow solver over hybrid unstructured meshes comes from. Moreover, the algorithm proposed in the past are either very complex to implement or the straight away extension to unstructured grid is not possible. Hence in addition to the robustness of the solver, there is a need to develop an algorithm which can be easily adopted in any of the existing Cartesian or unstructured grid solvers.

Apart from the solver development, a detailed literature survey on the droplet detachment has been carried out and it has been found that there is very less amount of work available on the numerical prediction of droplet placed on the lower surface of a horizontal substrate. Although, there exist studies wherein some of the major aspects of droplet detachment have been considered, but the study is limited to a single density ratio. Hence, there is a need to focus on the effect of various parameters on the droplet dripping and detachment process.

Along with the droplet detachment study, an equally important phenomenon is the impinging of a droplet on to a thin liquid film. Various studies have already been performed to unveil the dynamics associated with the droplet impinging over films with a constant thickness. To the best of authors knowledge, no study has been performed for variable film thickness. Thus, in the present work, we would also like to focus our attention towards the deformation of a single droplet falling over thin liquid film with variable thickness.

1.3 Objectives

With the primary motivation to develop a robust three-dimensional multiphase solver over a hybrid unstructured grid, the objectives of this thesis have been set as follows.

Algorithm development

We propose to develop a robust algorithm for multiphase flow simulations over three-dimensional hybrid unstructured grid by incorporating the ideas of force balancing and the concept of consistent mass momentum transport. In the framework of an algebraic volume of fluid method, the emphasis will essentially be on the methodologies that can be easily implemented over unstructured meshes. The robustness of the algorithm will then be tested by considering the presence of large interfacial and/or body forces through a set of numerical experiments.

Apart from the solver development activities, attention will also be focussed to explore the dynamics of liquid droplet in the following two circumstances.

Droplet detaching from a horizontal solid substrate

Using the developed solver, more insights into the droplet dripping and detachment characteristics will be looked in detail, and the effect of various parameters including density ratio, surface wettabilities and Weber number will be explored. The effect of the presence of an adjacent droplet will also be studied separately.

Droplet impingement over thin liquid film

The effect of the impingement of droplet over variable film thickness has largely been overlooked. Hence, we would like to focus our attention on the dynamics of a droplet impinging over sinusoidally varying thin liquid films. At last, the effect of the angle with which the droplet hits the film will also be explored.

1.4 Thesis Overview

The work is presented in terms of following self contained chapters.

A detailed literature review on the available techniques to capture the phase interface together with different formulations proposed in the past to achieve force balancing has been presented in chapter 1. In addition to this, literature survey regarding the droplet detachment process and impingement of a droplet over thin liquid film has also been shown. The chapter is concluded by presenting the objectives of the present thesis.

Chapter 2 deals with the governing equations and discretization procedure adopted in the context of consistency and force balancing. As the work has been started from scratch, initial testing of the Navier-Stokes equation and the volume fraction equation has also been shown separately.

Chapter 3 present the results of force balancing achieved by employing least squares method and its comparison with the unbalanced force algorithm. It also shows the importance of consistent treatment of convective term appearing in the

governing equations of different variables.

Chapter 4 focusses on the results of force balancing achieved due to the implementation of a novel strategy, which in the present work has been named as Modified Green Gauss (MGG) method. Considering various interfacial and body forces, the present modified strategy has been compared against the results obtained by the traditional Green Gauss method.

In chapter 5, using the present solver, an investigation has been carried out to reveal the dynamics of droplet attached to a horizontal solid substarte. Various factors influencing the droplet behavior including density ratio, contact angle and Weber number has been considered. Along with this, the effect of the presence of an adjacent droplet has also been shown later in the chapter.

Chapter 6 discusses various cases wherein a droplet impinges over a thin liquid film with variable thickness. The results are also compared against the case when the droplet impinges over a liquid film with constant thickness. Later, the effect of the droplet impinging angle on the behavior of crown structure has also been reported.

Chapter 7 concludes the present work together with the recommendations for future work.

Chapter 2

Governing Equations and Discretization Procedure

2.1 Governing Equations

In the present work, two different fluids separated by interface are assumed to be incompressible and follow the same set of governing equations describing mass and momentum conservation.

Momentum Transport Equation :

$$\frac{\partial(\rho \mathbf{u})}{\partial t} + \nabla \cdot (\rho \mathbf{u}\mathbf{u}) = -\nabla p + \nabla \cdot \left[\mu\left(\nabla \mathbf{u} + \nabla \mathbf{u}^T\right)\right] + \mathbf{S}_\phi \tag{2.1}$$

Continuity Equation :

$$\nabla \cdot \mathbf{u} = 0 \tag{2.2}$$

where $\mathbf{u}$ is the velocity vector, ρ is the density, p is the mechanical pressure and $\mathbf{S}_\phi$ collectively represent the body and interfacial forcing terms. In VOF method, for capturing the interface, an additional volume fraction equation is solved along with the conservation of mass and momentum. The volume fraction equation is given by,

$$\frac{\partial f}{\partial t} + \mathbf{u} \cdot \nabla f = 0 \tag{2.3}$$

where f is the fraction of liquid present in the cell under consideration. Using the continuity constraint, volume fraction equation in divergence form can be written as,

$$\frac{\partial f}{\partial t} + \nabla \cdot (\mathbf{u}f) = 0 \tag{2.4}$$

Fluid properties can be expressed as a function of volume fraction f and can be written in the following way.

$$\rho = \rho_1 f + \rho_2(1 - f) \tag{2.5}$$

$$\mu = \mu_1 f + \mu_2(1 - f) \tag{2.6}$$

Here, subscripts 1 and 2 represent fluid 1 and fluid 2, respectively. The value of f is unity for the computational cells fully occupied by fluid 1 and for the cells which are fully occupied by fluid 2, its value is zero. The value of f in computational cells through which interface passes lies in-between zero and unity (Fig. 2.1).

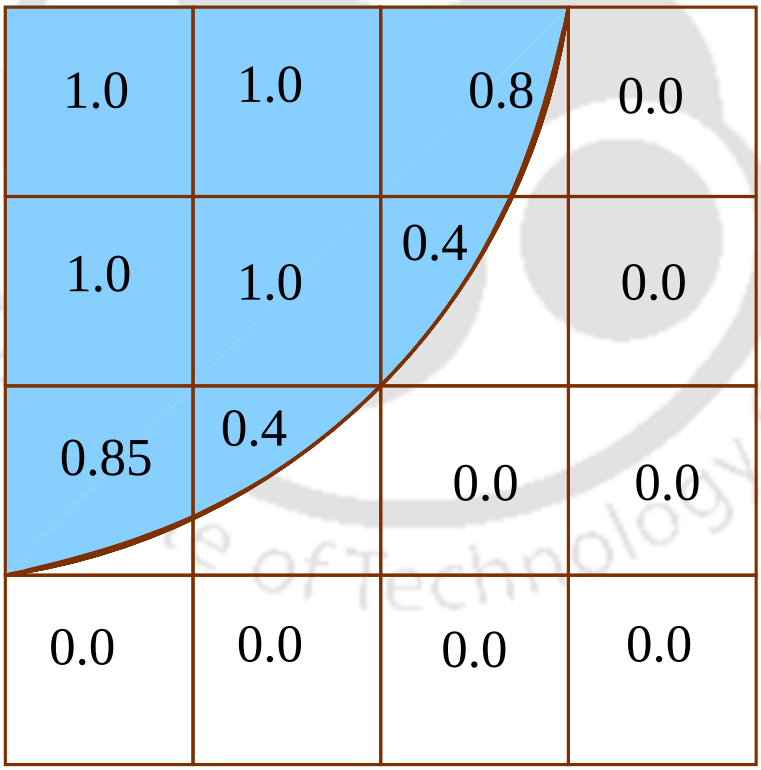

Figure 2.1: Volume fraction field

2.2 Numerical Methods

In order to solve these coupled higher order partial differential equations, numerical techniques such as finite difference method (FDM), finite volume method (FVM) and finite element method (FEM) are usually employed. Finite volume method due to their conservative properties are generally adopted for simlating fluid flow problems. Herein, in this work, we also employ finite volume method to solve these set of partial differential equations.

The finite volume flow solver works on discrete control volumes and this necessitates the decomposition of a closed domain into several non–overlapping cells. This process is referred to as grid generation and in this work, the unstructured grid generation software GAMBIT is utilised for this purpose. The geometric information pertaining to the grid needs to be derived to be used in the finite volume framework and this is precisely the role of the preprocessor. The preprocessor calculates all geometric information pertaining to the grid, such as the volume, face areas and surface normals as well as the centroids, which appear in the discrete form of the governing equations. In the present work, the focus being on a generic solver, all elemental topologies are handled in a unified manner. The cell shapes could be arbitrary convex polygons but largely consist of tetrahedra, hexahedra, prisms and pyramids or a combination thereof (refer Fig. 2.2). Figure 2.3 (a) shows a typical representation of a hybrid grid where a centrally located tetrahedral cell is surrounded by three prisms and one another tetrahedral cell. The area normal for a polygonal face with n vertices can be calculated as the sum of the cross product of the coordinate vectors of its nodes $\mathbf{V}$ in a cyclic manner.

$$\mathbf{S}_f = \sum_{i=1}^{n} \mathbf{V}_i \times \mathbf{V}_{i+1} \tag{2.7}$$

A general approach for volume calculation is also adopted which defines the cell volume as,

$$V = \frac{1}{3} \sum_{i=1}^{nf} \mathbf{x}_i \cdot \hat{\mathbf{n}}_i \; A_i$$

where nf represents the number of faces, and $\mathbf{x}_i$ is the face center, $\hat{\mathbf{n}}_i$ is its unit normal vector and A_i is the area magnitude of the i^{th} face. The cell centroids are calculated as average of the vertex coordinates and the distance between cell centers

sharing a face as well as the normal distance between the center of each cell and its faces are also calculated and stored a priori.

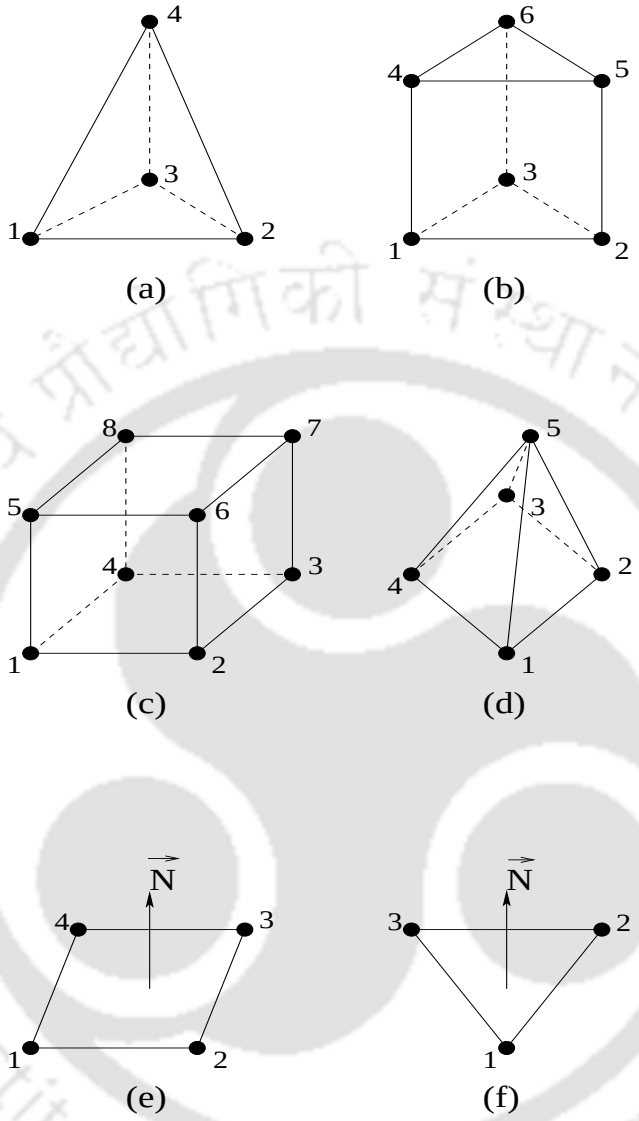

Figure 2.2: Different types of cell. (a) Tetrahedron (b) Prism (c) Hexahedron (d) Pyramid (e) Quadrilateral (f) Triangle

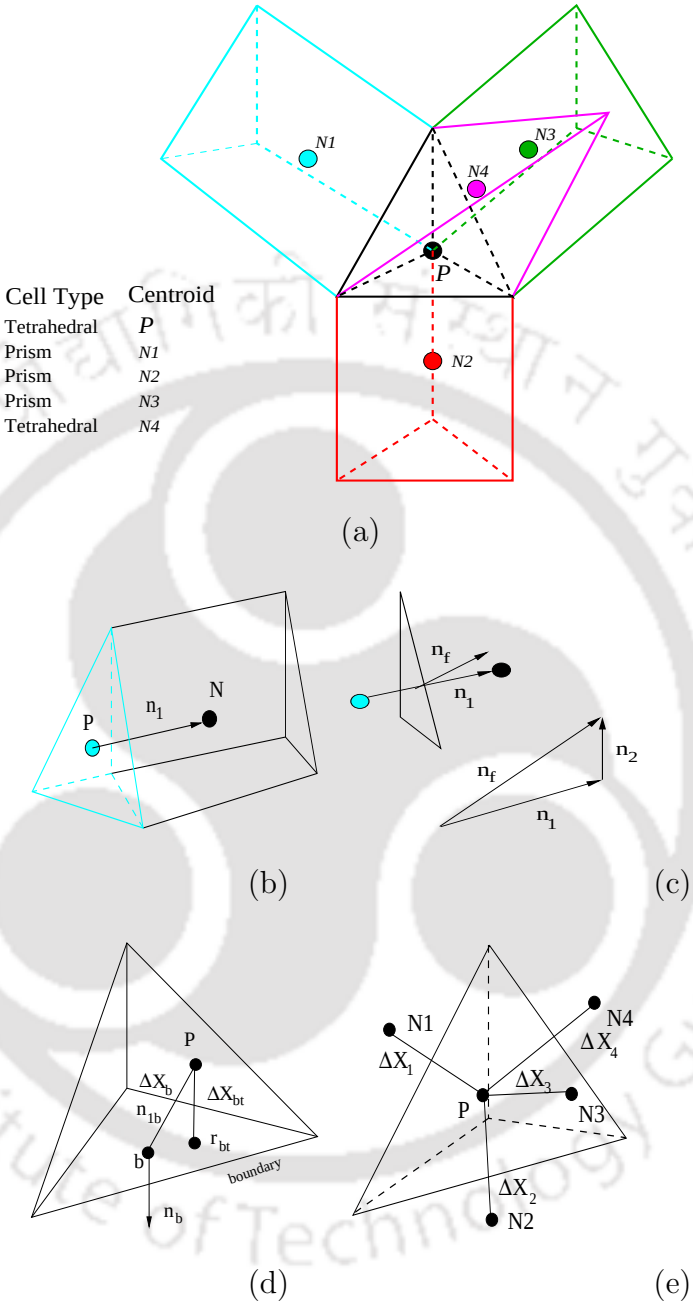

Figure 2.3: (a) Control volume and its neighbors (b) Main and neighbor control volumes (c) Unit vectors (d) Boundary cell (e) Geometrical parameters.

2.3 Discretization of The Governing Equations

The numerical approach adopted in this work is similar in the lines of Dalal et al. [62], wherein the computational domain is subdivided into a large number of cells (control volumes). Collocated grid arrangement has been followed, where all the solution variables are defined at the centroid of each cell. Integrating Eqs. 2.3 and 2.1 over the control volume and applying Gauss's theorem to the convective and diffusive part, semi-discrete form of the advection and momentum equations with Euler implicit time scheme can be written as:

$$V_{\mathrm{P}}\frac{f_{\mathrm{P}}^{n+1}-f_{\mathrm{P}}^{n}}{\Delta t}+\sum_{f}F_{f}^{n}f_{f}^{n+1}=0 \tag{2.8}$$

$$V_{\mathrm{P}}\frac{(\rho\mathbf{u})_{\mathrm{P}}^{n+1}-(\rho\mathbf{u})_{\mathrm{P}}^{n}}{\Delta t}+\sum_{f}F_{f}^{n}(\rho\mathbf{u})_{f}^{n+1}-\sum_{f}F_{d\mathbf{u}f}^{n+1}=\mathbf{S}_{\phi}\mathrm{V}_{\mathrm{P}} \tag{2.9}$$

where, F_f^n and $F_{d\mathbf{u}f}^{n+1}$ represent the explicit and implicit treatment of volume fluxes and diffusive fluxes, respectively. It is to be noted that the subscripts "P"and "f"represent values at cell centroid and faces, respectively. Discretization of convection, diffusion and source terms are done in the following way.

2.3.1 Convective flux treatment

Integrating the convective term appearing in momentum and volume fraction equations over the control volume and applying Gauss divergence theorem, the convective fluxes, for any variable ϕ, can be written as:

$$\int_{\mathrm{V}}\nabla\cdot(\mathbf{u}\phi)\,\mathrm{dV}=\int_{S}(\mathbf{u}\phi)\cdot\mathrm{d}\mathbf{S}\approx\sum_{f}(\phi\mathbf{u})_{f}\cdot\mathbf{S}_{f}=\sum_{f}F_{f}\phi_{f}$$

where

$$F_f=\mathbf{u}_f\cdot\mathbf{S}_f\quad\text{and}\quad\phi=\rho\mathbf{u}\ \text{ or }\ f$$

It is to be noted that we linearize the convective terms (see Eqs. 2.8 and 2.9) by calculating the F_f from the known previous time step values. Now, ϕ_f can be found out by utilizing different convective schemes.

In the present work, a linear combination of upwind scheme and central differencing scheme is employed for transporting the momentums, while for volume fractions,

a high resolution scheme CUBISTA [24] has been used. The benefit of using high resolution scheme for advecting the volume fraction is shown later in this chapter.

Linear combination of upwind and central differencing schemes

The convective fluxes using this scheme can be expressed as,

$$F_f\phi_f = (F_f\phi_f)^{\mathrm{UDS}} + \gamma[(F_f\phi_f)^{\mathrm{CDS}} - (F_f\phi_f)^{\mathrm{UDS}}] \tag{2.10}$$

where, UDS and CDS represents upwind and central difference schemes. Expanding these terms will result in,

$$F_f\phi_f = \phi_{\mathrm{P}}[|F_f, 0|] - \phi_{\mathrm{N}}[|-F_f, 0|] + \gamma\{F_f\left(\frac{V_{\mathrm{N}}}{V_{\mathrm{N}}+V_{\mathrm{P}}}\phi_{\mathrm{P}} + \frac{V_{\mathrm{P}}}{V_{\mathrm{N}}+V_{\mathrm{P}}}\phi_{\mathrm{N}}\right)$$

here F_f denotes volume flux at a particular face of the cell and the value of γ varies between 0 and 1.

CUBISTA

For implementing the CUBISTA scheme over unstructured meshes, normalized variable approach of Jasak et al. [23] is followed and the final form of the scheme in terms of normalized variable $\left(\widetilde{\phi} = \frac{\phi-\phi_{\mathrm{U}}}{\phi_{\mathrm{D}}-\phi_{\mathrm{U}}},\right.$ where subscript U and D refer to the far upwind and downwind cells$\left.\right)$ can be written as below.

$$\widetilde{\phi}_f = \begin{cases} \frac{7}{4}\widetilde{\phi}_{\mathrm{C}} & 0 < \widetilde{\phi}_{\mathrm{C}} < \frac{3}{8} \\ \frac{3}{4}\widetilde{\phi}_{\mathrm{C}} + \frac{3}{8} & \frac{3}{8} \leq \widetilde{\phi}_{\mathrm{C}} \leq \frac{3}{4} \\ \frac{1}{4}\widetilde{\phi}_{\mathrm{C}} + \frac{3}{4} & \frac{3}{4} < \widetilde{\phi}_{\mathrm{C}} < 1 \\ \widetilde{\phi}_{\mathrm{C}} & \text{elsewhere} \end{cases}$$

In case of unstructured grid as shown in Fig. 2.4, far upwind point is not clearly defined. Using the approach of Jasak et al. [23], the value at the far upwind point is replaced by the known values of upwind and downwind grid points. They showed that,

$$\widetilde{\phi_{\mathrm{C}}} = \frac{\phi_{\mathrm{C}} - \phi_{\mathrm{U}}}{\phi_{\mathrm{D}} - \phi_{\mathrm{U}}} = 1 - \frac{\phi_{\mathrm{D}} - \phi_{\mathrm{C}}}{2(\nabla\phi)_{\mathrm{C}} \cdot \mathbf{n}_f} \tag{2.11}$$

2.3.2 Diffusive flux treatment

Using Gauss divergence theorem, the diffusive fluxes for variable Φ $\left(\Phi = \frac{\phi}{\rho}\right)$ is discretized in the following manner.

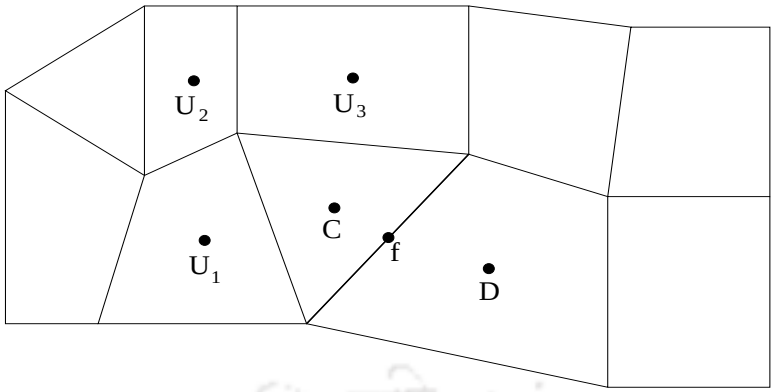

Figure 2.4: Unstructured grid showing upwind, downwind and far upwind cells.

$$\int_{\mathrm{V}} \nabla \cdot (\mu \nabla \Phi)\, \mathrm{dV} = \int_{S} (\mu \nabla \Phi) \cdot \mathrm{d}\mathbf{S} \approx \sum_{f} (\mu \nabla \Phi \cdot \mathbf{S})_f = \sum_{f} F_{d\Phi f}$$

where $\mathbf{S}_f$ is the face area vector with a magnitude of A_f and its direction is given by unit vector $\hat{\mathbf{n}}_f$. For non orthogonal grids, the surface vector is inclined to the line joining adjacent cell centres and thus giving rise to the non-orthogonal component of diffusive fluxes. To understand it, let us consider a geometrical arrangement as shown in Fig. 2.5, where a face "abc" is shared by two neighboring tetrahedral cells with centers marked as P and N. The face unit normal is represented by $\hat{\mathbf{n}}_f$. Projecting the cell centres over the surface normal will result in two more points P′ and N′. Now, we can write

$$\overrightarrow{ON} + \overrightarrow{NN'} = \overrightarrow{ON'}$$
$$\overrightarrow{OP} + \overrightarrow{PP'} = \overrightarrow{OP'}$$

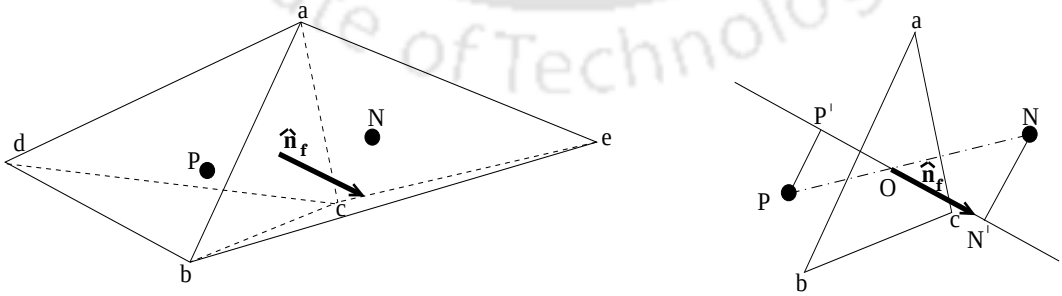

Figure 2.5: Non-orthogonal contribution of diffusive fluxes.

For a particular face, the diffusive fluxes can now be calculated as,

$$(\nabla\Phi)_f \cdot \mathbf{S}_f = A_f (\nabla\Phi)_f \cdot \hat{\mathbf{n}}_f = A_f \frac{(\Phi_{\mathrm{N}'} - \Phi_{\mathrm{P}'})}{\Delta n} \tag{2.12}$$

where Δn is the distance between points P′ and N′. Using Taylor series expansion, $\Phi_{\mathrm{N}'}$ and $\Phi_{\mathrm{P}'}$ can be expressed as (neglecting higher order terms),

$$\Phi_{N'} = \Phi_N + \overrightarrow{\nabla\Phi_N} \cdot \overrightarrow{NN'} \tag{2.13}$$

$$\Phi_{P'} = \Phi_P + \overrightarrow{\nabla\Phi_P} \cdot \overrightarrow{PP'} \tag{2.14}$$

Substituting Eqs. 2.13 and 2.14 in Eq. 2.12, finally we get

$$(\nabla\Phi)_f \cdot \mathbf{S}_f = A_f \frac{(\Phi_{\mathrm{N}} - \Phi_{\mathrm{P}})}{\Delta n} + \frac{(\nabla\Phi_{\mathrm{N}} \cdot \mathbf{NN'} - \nabla\Phi_{\mathrm{P}} \cdot \mathbf{PP'})A_f}{\Delta n} \tag{2.15}$$

The value of $\overrightarrow{NN'}$ and $\overrightarrow{PP'}$ can be obtained by following the procedure as shown below,

$$\overrightarrow{NN'} = \overrightarrow{ON'} - \overrightarrow{ON}, \qquad \overrightarrow{ON'} = (\overrightarrow{ON} \cdot \hat{\mathbf{n}_f})\hat{\mathbf{n}_f}$$

$$\overrightarrow{PP'} = \overrightarrow{OP'} - \overrightarrow{OP}, \qquad \overrightarrow{OP'} = (\overrightarrow{OP} \cdot \hat{\mathbf{n}_f})\hat{\mathbf{n}_f}$$

The first part of Eq. 2.15 is the orthogonal component of diffusive fluxes while the second part is mainly appearing due to non-orthogonality of the grids. It is to be noted that for calculating value at the face for any variable ϕ, inverse volume weighted interpolation technique employed by Dalal et al. [62] is used unless otherwise stated.

2.3.3 Source term

As far as binary fluid flows are concerned, handling of source term plays a major role in force balancing. The traditional approach of handling all the source terms using Green Gauss reconstruction method may result in an unphysical flow field near to the interface. In the present work, instead of using Green Gauss method, we propose to employ modified Green Gauss and least squares based reconstruction techniques. These formulations are discussed in details in chapters 3 and 4.

As the solver has been developed form scratch, we initially employed Green Gauss method and the results were satisfactory as far as single phase is concerned. We have solved various problems of single phase flows both in two and three dimensions and few of the results are shown later in this chapter. For single phase laminar incompressible fluid flows, usually the source term consists of only pressure gradient. Using Green Gauss approach, the reconstruction of pressure gradient at each cell center can be expressed as,

$$\int_{\mathrm{dV}} \nabla p \ \mathrm{dV} \approx \int_S p \ \mathbf{dS} \approx \sum_f p_f \mathbf{S_f} \tag{2.16}$$

2.4 Pressure Velocity Coupling

Here we explain the momentum interpolation technique applied for simulating single fluid flows. However, for handling binary fluid flows, we propose a change in the momentum interpolation formula used here. These details are shown later in chapters 3 and 4, where complete balanced force strategy is discussed.

In order to avoid the pressure checker board problem on collocated meshes, we use momentum interpolation technique which is similar to the method proposed by Rhie and Chow [103]. Initially, in order to calculate the provisional momentum, we drop the pressure gradient term from the momentum equation. The resultant momentum equation in semi discrete form can be written as,

$$V_{\mathrm{P}} \frac{(\rho \mathbf{u})^*_{\mathrm{P}} - (\rho \mathbf{u})^n_{\mathrm{P}}}{\Delta t} + \sum_f F^n_f (\rho \mathbf{u})^*_f - \sum_f F^*_{d\mathbf{u}f} = 0 \tag{2.17}$$

To get the pressure field, we solve pressure Poisson equation (PPE), which is obtained by subtracting the provisional momentum equation from the full momentum equation and then taking the divergence. In general the PPE can be written as,

$$\nabla \cdot \left(\frac{\nabla p}{\rho} \right) = \frac{\nabla \cdot \mathbf{u}^*}{\Delta t} \tag{2.18}$$

In discrete form, it can be written as,

$$\Delta t \sum_f \left(\frac{\nabla p^*}{\rho} \right)_f \cdot \mathbf{S}_f = \sum_f F^*_{0f} \tag{2.19}$$

where

$$F_{0f}^{*} = \mathbf{u}_{f}^{*} \cdot \mathbf{S}_{f} \tag{2.20}$$

The discrete form of the pressure Poisson equation generates system of linear equations, which are iteratively solved by ILU pre-conditioned krylov solver using [104]. Once the pressure field is obtained, convective fluxes at each face is then corrected by following,

$$F_{f}^{n+1} = F_{0f}^{*} - \Delta t \left(\frac{\nabla p^{*}}{\rho} \right)_{f} \cdot \mathbf{S}_{f} \tag{2.21}$$

Finally, we update the cell centroid velocities in the following way.

$$\mathbf{u}_{\mathrm{P}}^{n+1} = \mathbf{u}_{\mathrm{P}}^{*} - \Delta t \left(\frac{\nabla p}{\rho} \right)_{\mathrm{P}} \tag{2.22}$$

In order to get the cell centroidal momentum, the obtained velocities are multiplied by density of the respective cells. The stepwise solution procedure followed in this work is summarized as follows.

2.5 Solution Algorithm

The overall solution procedure is as follows.

1. Initialize all the variables suitably.
2. Assume F_{f}^{n+1}=F_{f}^{n}
3. Solve Eq. 2.17 iteratively to get provisional velocities.
4. Calculate provisional fluxes and iterate Eq. 2.18 upto desired tolerance level to get pressure field.
5. Update the fluxes at faces and calculate all the cell centroid velocities using Eq. 2.22
6. For the next time step calculations, go back to step 3 and repeat the same procedure until stopping criterion is met.

2.6 Validations

During the development of the solver, the code is validated in each and every step to check its accuracy. For the single phase solver, the benchmark problems of lid driven cavity and flow over a backward facing step are simulated and compared against the benchmark solutions. In order to capture the phase interface as sharp as possible, in this work for advecting the volume fractions, two high resolution schemes are employed. The performance of these schemes is checked by simulating a well known solid disc rotation problem and shearing flow test. In the following subsections, the results of these test cases are presented in detail.

2.6.1 Lid driven flow in a square cavity

The three-dimensional lid–driven cavity flow problem is solved using 2,71,320 tetrahedral cells in a $1 \times 1 \times 1$ cubical cavity with a moving lid at the top and stationary walls at the sides and the bottom. The top lid moves with a non-dimensional velocity of unity and simulations are carried out for Reynolds numbers of 100, 400 and 1000, ensuring a laminar regime for the flows. The velocity variation along the vertical and horizontal centerline of the cavity are shown in Figures 2.6 (a) and (b) with the results of Ku et al. [105]. It shows very good agreement with the literature.

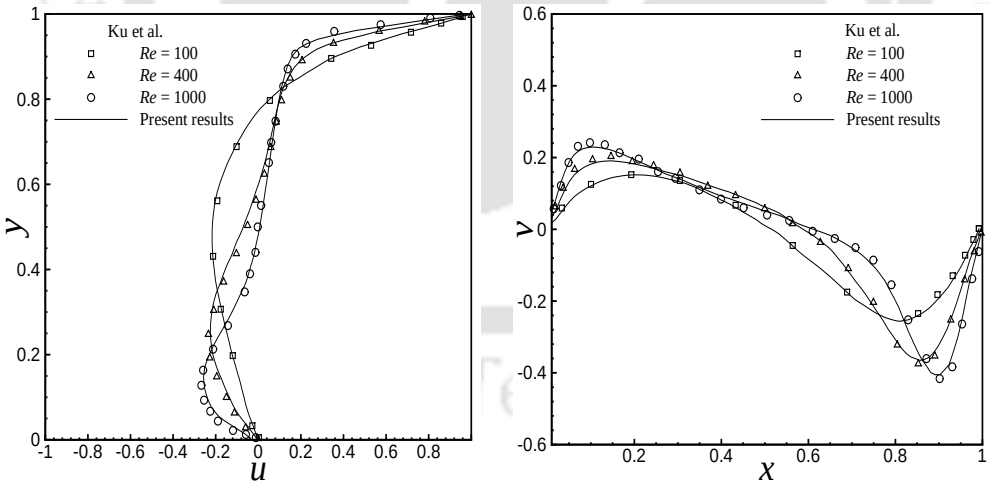

(a) (b)

Figure 2.6: (a) u–velocity along vertical centerline, (b) v–velocity along horizontal centerline

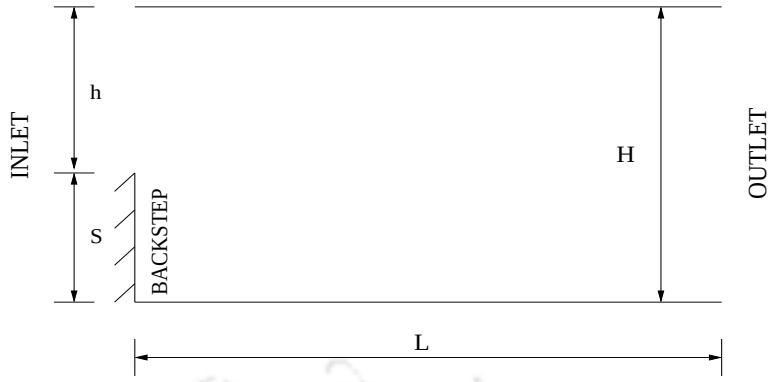

Figure 2.7: Geometry of backward facing step flows.

2.6.2 Two–dimensional channel flow over a backward facing step

A more challenging test case for internal flows is the flow over a two-dimensional backward facing step. The geometry considered for the study is shown in Figure 2.7, where the expansion ratio (H/h) is chosen as 1.9423 to compare the results with Biswas et al. [106]. A fully developed parabolic velocity profile is assumed at the inlet and the Reynolds number based on twice the step height is varied to study the recirculation length and flow structure. At the outlet, a zero normal gradient have been imposed for velocities while homogeneous Dirichlet boundary condition is applied for pressure. No slip boundary condition has been imposed for all the channel walls. The channel length is taken to be 20 times the step height, which is chosen to be unity. The velocity in the domain has been initialized with average velocity at the inlet.

Simulations are carried out on a hexahedral grid with 36000 cells at Reynolds numbers of 50, 100, 400, 600 and 800. The comparison of non-dimensional recirculation length (L_r/S, where S is the step height) with the numerical results in Biswas et al. [106] is shown in Figure 2.8 (a) and is in good agreement. Also, a streamline plot has been shown in Fig. 2.8 (b) for the case of Reynolds number $Re_D = 200$.

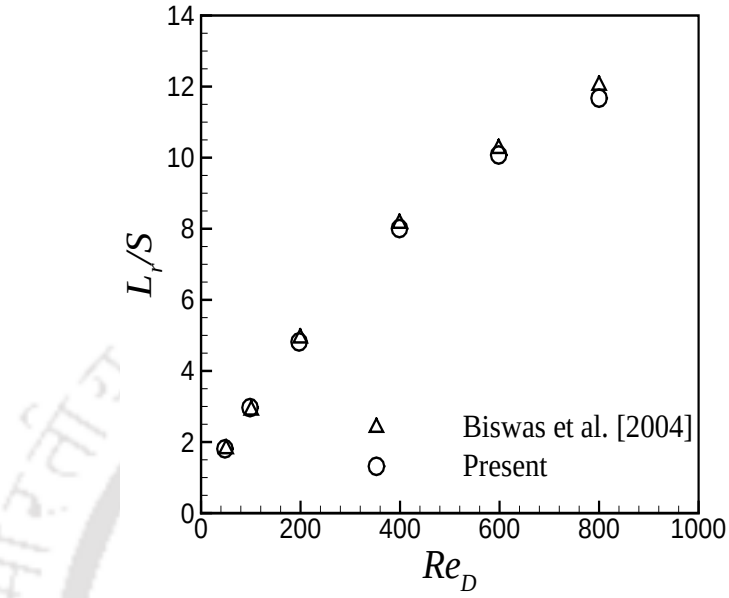

(a)

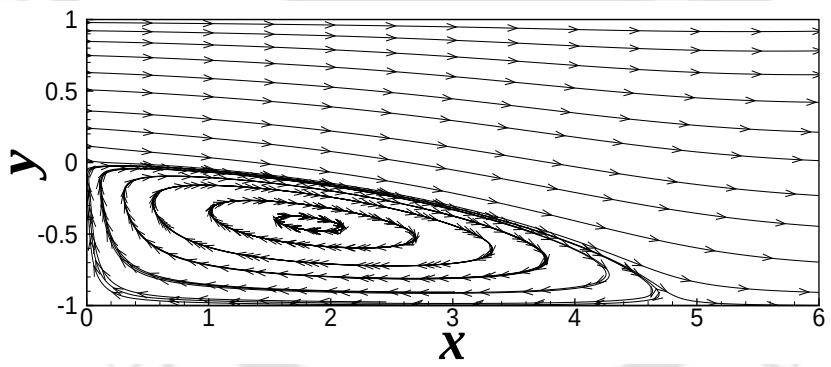

(b)

Figure 2.8: (a) Comparison of the recirculation bubble length for different Reynolds numbers. (b) Streamlines for the case of $Re_D = 200$.

2.6.3 Advection of slotted circle in a rotational flow field

In order to test the performance of various schemes to advect the phase interface as accurate as possible, Zalesak's [107] solid-body rotation is widely accepted by the research community. The test case considers the rotation of a slotted circle by a vortex flow centered at the mid point of the domain. The computational domain chosen is a square with dimensions 4×4 and is decomposed into 90,000 non-uniform hexahedral cells and 89,992 prism cells. The center of the slotted disk of diameter $D = 1$ is at (2.0, 2.65) and is cut by a slot of width 0.12 units. Simulations are carried out upto two complete revolutions using a constant time step of 0.005 and the results are shown in Fig. 2.9 and 2.10 for hexahedral and prism cells, respectively. It can be easily noticed that the results produced by upwind scheme is highly diffused, while the performance of both the other schemes i.e CUIBS and CUBISTA are within acceptable limits.

2.6.4 Circular disc in a shear flow

In the previous test case, the slotted circle does not undergo any topological changes and hence there is a need to check the applicability of the high resolution scheme to predict the flows where the interface experiences shear. In order to account for such shearing effect, a test case with a circle placed in a single vortex [108] is generally adopted. In this test case, a circle is subjected to a shearing flow fields as indicated by the following velocity definitions,

$$u = \sin(x)\cos(y) \qquad v = -\cos(x)\sin(y) \tag{2.23}$$

The computational domain chosen for this test case is a perfect square having an edge length of π in each directions and is discretized by 100×100, 200×200 and 300×300 control volumes. Initially, a circle with a radius of $\pi/5$ is placed inside the domain at $(x, y) = (\frac{\pi}{2}, \frac{\pi}{4})$. With a fixed time step of $t = \pi/400$, the circle is allowed to rotate in clockwise direction for 1000 time steps and again it is rotated back to its initial position by reversing the flow directions. Ideally, the circle should regain back its initial position with negligible loss of mass. The results acheived for this case by employing CUBISTA scheme is shown in Fig. 2.11. A small deviation is noticable at the bottom of the circle. Table 2.1 shows the mass conservation error (refer Eq. 2.24) for this case and Fig. 2.12 shows its temporal variation. As can be

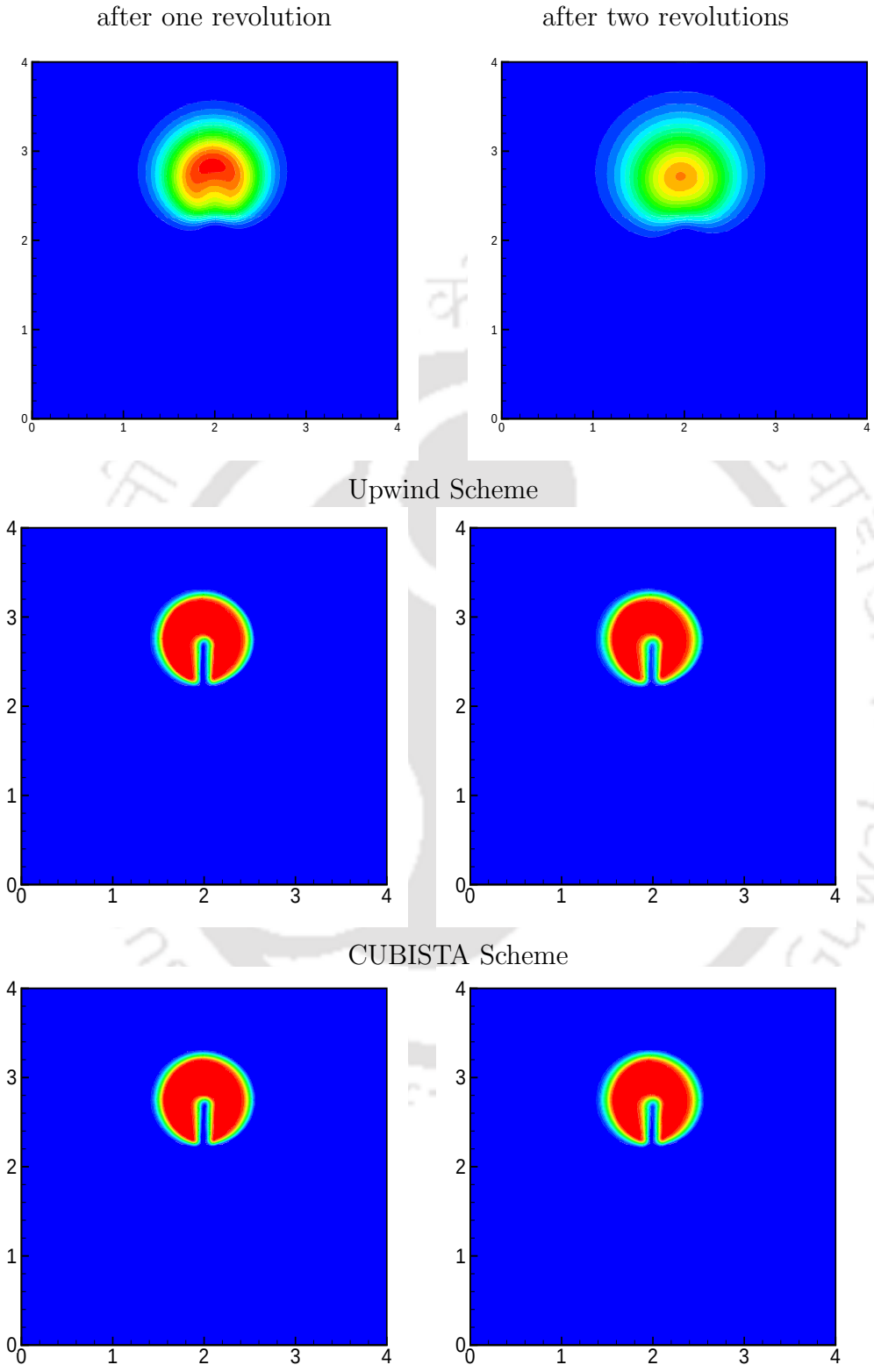

Figure 2.9: Rotation of a slotted circle using non-uniform hexahedral cells.

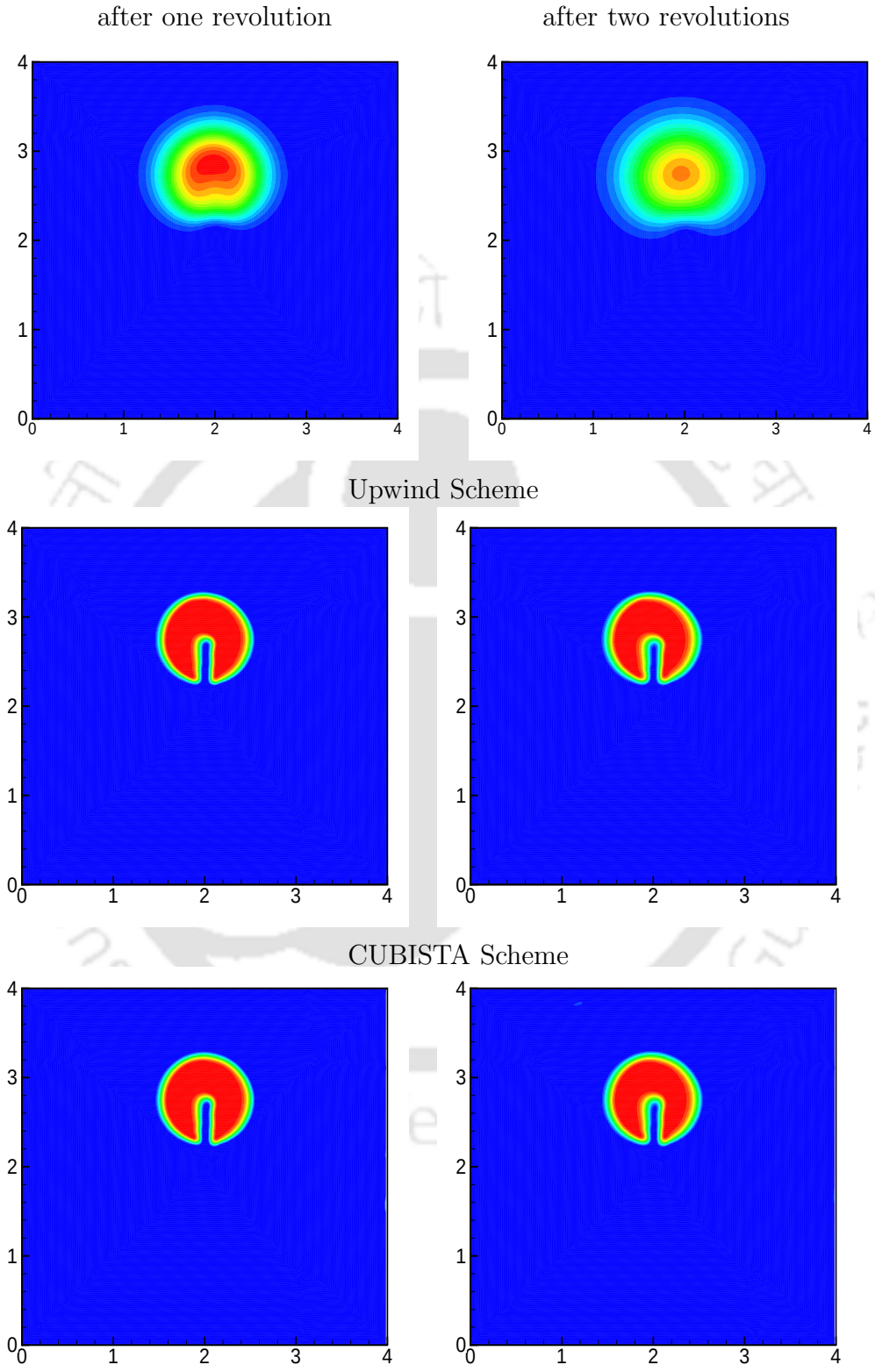

Figure 2.10: Rotation of a slotted circle using prism cells.

seen from Table 2.1, the value of mass conservation error reduces with the increase in mesh resolution.

$$\epsilon_{mass} = \frac{|\sum_{cell} f_{\mathrm{P}}^{final} - \sum_{cell} f_{\mathrm{P}}^{exact}|}{\sum_{cell} f_{\mathrm{P}}^{initial}} \times 100 \tag{2.24}$$

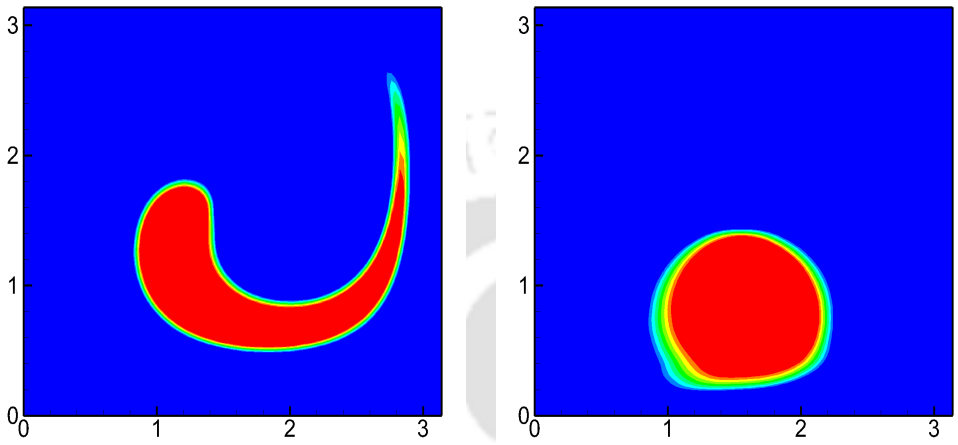

(a) (b)

Figure 2.11: Rotation of a circle in the presence of a single deforming vortex. Contour plots of volume fraction after (a) clockwise 1000 Δt and then (b) 1000 Δt in anti-clockwise direction.

grid	$\epsilon_{mass}(2000\ \Delta t)$
100×100	0.79
150×150	0.71
200×200	0.70

Table 2.1: Mass conservation error for shearing test.

2.7 Closure

As the solver has been developed from scratch, herein, in this chapter we presented some of our early results for single phase flows. Another case for testing the advection

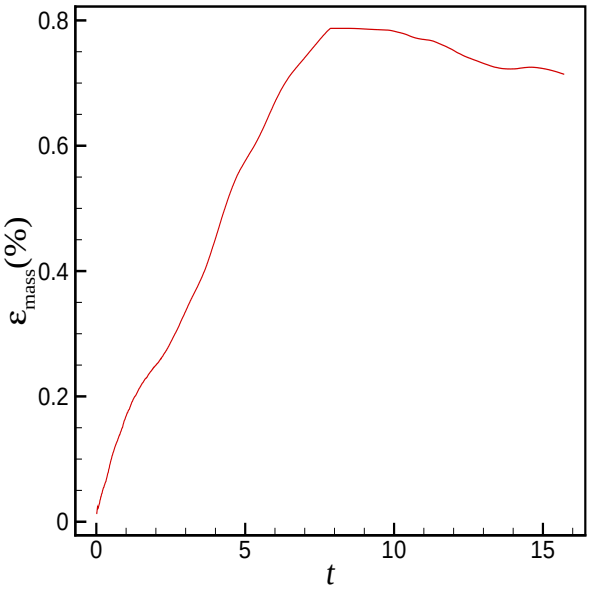

Figure 2.12: Temporal variation of mass conservation error for the case of shearing of a circle in the presence of a single vortex. The grid is 200 × 200.

equation has also been presented with the aid of slotted disc rotation test. For single phase flows, the gradient reconstruction technique doesn't matter much and we could get good comparison of our results with some of the benchmark problems. But, how the gradient reconstruction technique will hamper the solutions of binary fluids flows will be shown in the subsequent chapters.

Chapter 3

A Well Balanced and Consistent Algorithm For Multiphase Flows

We further carried our development activities to combine the Navier-Stokes solver with the advection equation to simulate some of the benchmark problems in binary fluid flows. But, as already pointed out that the handling of source terms in these kind of flows sometimes introduces unphysical flow field if not properly treated. Herein, in this chapter, we explain the way by which force balancing is achieved in the present work. Along with this, we also highlight the importance of consistent mass momentum transport within a VOF framework.

3.1 Balanced Force Strategy

In order to achieve proper balance between competing forces like surface tension force and the associated pressure gradient, treatment of source term at discrete level plays a major role. Although one can apply the Green Gauss reconstruction method (explained in Section 2.3.3) to calculate the cell centroid values of these source terms, but in the context of binary fluid flows, one needs to take necessary precautions while handling them. The handling of source terms, momentum interpolation and the solution algorithm are now discussed in details.

3.1.1 Source terms and their discretization

Source term appears only in the momentum equations and consists of pressure gradient, gravity and surface tension terms. The surface tension term appearing in the momentum equations is modelled by employing the continuum surface force (CSF) formulation of Brackbill et al. [49] and piezometric treatment of the gravity term is adopted similar to [60]. The numerical treatment of pressure gradient, gravitational force and the surface tension term are as follows.

Pressure gradient

In the proposed algorithm on multiphase flows, we chose to adopt a different approach for the calculation of cell centroid gradients. This approach ensures that the cell centroid gradients are obtained from the face centered directional derivatives of pressure using the least squares approach as in Mahesh et al. [55]. We very briefly discuss their approach of gradient calculation. Let $\frac{\delta p}{\delta n}$ be the discrete representation of normal pressure derivative at each face. A similar directional derivatives may be obtained for other quantities like velocities, density and volume fraction if necessary. With the known values of directional derivatives of pressure at the faces, the cell centroid pressure gradient is obtained by implementing the face area weighted least squares method as done in [65], which minimizes

$$\epsilon_{\mathrm{P}} = \sum_{f} (\mathbf{P}_{\mathrm{P}} \cdot \hat{\mathbf{n}}_f - \mathrm{P}_f)^2 A_f \tag{3.1}$$

where

$$\mathbf{P}_{\mathrm{P}} = \frac{1}{\rho_{\mathrm{P}}} \nabla p \tag{3.2}$$

and

$$\mathrm{P}_f = \frac{1}{\rho_f} \frac{\delta p}{\delta n} \tag{3.3}$$

where $\hat{\mathbf{n}}_f$ is the face unit normal and subscripts "P"and "f"represent values at cell centroid and faces, respectively. Finally this will lead to the solution of a 3×3 matrix to give the centroidal gradients.

Gravitational body force

As already mentioned that we consider the piezometric treatment of the gravity term similar to [60]. In piezometric approach, gravitational forcing term contains the gradient of density and hence, the two competing terms viz. pressure gradient

and the gravity can be treated in a similar way at discrete level. The piezometric pressure is defined as,

$$p' = p + \rho \mathbf{g} \cdot \mathbf{x} \tag{3.4}$$

The modified momentum equations can now be re-written as

$$\frac{\partial (\rho \mathbf{u})}{\partial t} + \nabla \cdot (\rho \mathbf{u}\mathbf{u}) = -\nabla p' + \nabla \cdot \left[\mu \Big(\nabla \mathbf{u} + \nabla \mathbf{u}^T \Big) \right] + \mathbf{g} \cdot \mathbf{x} \nabla \rho + \mathbf{F}_{st} \tag{3.5}$$

where $\mathbf{F}_{st}$ is the source term due to surface tension. The treatment of the gravitational body force term will depend on the way the gradients are discretized. While one could use a least squares based approach similar to pressure as shown in Eqs. 3.1-3.3, an alternate calculation of the gradient using Green Gauss approach may also be adopted. In such a case, the gravity term can be discretized as,

$$\begin{aligned} \int_{\mathrm{V}} \mathbf{g} \cdot \mathbf{x} \nabla \rho \mathrm{dV} &\approx \mathbf{g} \cdot \mathbf{x}_{\mathrm{P}} \sum_f \rho_f \mathbf{S}_f \approx \mathbf{g} \cdot \mathbf{x}_{\mathrm{P}} \sum_f \Big(\rho_1 f + \rho_2 (1 - f) \Big)_f \mathbf{S}_f \\ &\approx \mathbf{g} \cdot \mathbf{x}_{\mathrm{P}} \big(\rho_1 - \rho_2 \big) \sum_f f_f \mathbf{S}_f \end{aligned} \tag{3.6}$$

However, the use of dissimilar approaches for the calculation of gradients, such as Green Gauss reconstruction for gravity and/or surface tension and a least squares approach for the pressure is prone to introduce significant amount of spurious currents, which is a trademark of an unbalanced formulation.

On the other hand, a well balanced algorithm is the one, in which all the forcing terms are treated using identical gradient calculation procedure, which involves the least squares method in this study as described earlier. This is important because the pressure appears as a face normal gradient in the PPE, but takes the form of centroidal gradient during momentum update. Any imbalance between the normal derivative of pressure used in the PPE and its centroidal gradients which appear in momentum update can introduce significant amount of spurious currents.

Surface tension

For modelling the surface tension force, we follow the work of Brackbill et al. [49], where the force which was ideally acting only at the interface is modelled as a

smooth volumetric force acting over a small region near to the interface. Using their approach, surface tension force can be written as,

$$\mathbf{F}_{st} = \sigma\kappa\nabla f$$

where, $\mathbf{F}_{st}$ is the force due to surface tension. As the surface tension term inherently involves the gradient of volume fraction, it can be discretized in a way similar to the pressure gradient term. Importantly, the surface tension term also involves the calculation of curvature which has to be computed in most cases using numerical techniques in the following way.

$$\kappa = -\nabla \cdot \mathbf{n}, \qquad \mathbf{n} = \frac{\nabla f}{|\nabla f|}$$

where $\mathbf{n}$ is the vector normal to the phase interface. The volume fraction field f $(0 \leq f \leq 1)$, which differentiates the two fluids is not a continuous field and needs to be smoothed for the curvature calculation [49]. Here, for the calculation of curvature, we have closely followed the work of Ubbink [109], where they define a Laplacian filter which transforms the existing volume fraction field into a smooth field. For a discrete mesh, it is written as below.

$$\Im(f)_{\mathrm{P}} = \frac{\sum\limits_{f} f_f \;\; |\mathbf{S}_f|}{\sum\limits_{f} |\mathbf{S}_f|}$$

This filter is applied 2-3 times repeatedly over the volume fraction field and finally this smoothed field is used for the calculation of the curvature in the following manner.

$$\kappa_{\mathrm{P}} = -\nabla \cdot \left(\frac{\nabla f}{|\nabla f|}\right)_{\mathrm{P}} \qquad \approx \qquad \frac{-1}{V_{\mathrm{P}}} \sum_{f} \left(\frac{\nabla f}{|\nabla f|}\right)_{f} \cdot \mathbf{S}_f$$

Studies have been previously carried out on the need for using sophisticated algorithms for calculation of curvature, specially from the view point of reducing spurious currents. We mention that curvature calculation effects the spurious currents in any algorithm and it is an inevitable evil. And the spurious currents would occur not only because of the numerical error of the curvature, but also because of unbalanced treatment of surface tension term and the associated pressure gradients. Therefore, we emphasize that, although we use a simple approach to calculate the

curvature, the use of balanced force algorithm ensures that the present methodology gives results with very low spurious currents. For practical engineering problems, the present strategy may be considered as a cost effective alternative and it also has a generic application on hybrid unstructured meshes. We however remark that, the present balanced force algorithm can indeed be combined with other sophisticated approaches [53, 59, 110] to obtain lower spurious currents but at a higher computational cost.

3.1.2 Pressure velocity coupling

In order to avoid the pressure checker board problem on collocated meshes, we use momentum interpolation proposed by Rhie and Chow [103]. Initially, to calculate the provisional momentum, we drop the pressure gradient term from the momentum equation by following the work of Dalal et al. [62]. However, apart from the pressure gradient term, we also drop out the gravitational and the surface tension terms similar to [64]. Because they are competing terms as we have already explained in the previous sub-section, and since the pressure gradient is dropped, the surface tension and the gravitational terms are also dropped to calculate the provisional momentum. However, the methodology proposed by Francois et al. [53] adopted a different technique wherein they do not drop out the source terms for the calculation of provisional velocities, and hence ultimately correct the face velocities by solving a pressure correction equation. But, in the present work, we calculate the provisional momentum by solving the following equations.

$$\frac{\partial (\rho \mathbf{u})}{\partial t} + \nabla \cdot (\rho \mathbf{u}\mathbf{u}) - 2\nabla \cdot [\mu \mathbf{D}] = 0 \tag{3.7}$$

where $\mathbf{D}$ is the rate of deformation tensor. In semi-discrete form, the above mentioned equation can be written as

$$V_{\mathrm{P}} \frac{(\rho \mathbf{u})^{*}_{\mathrm{P}} - (\rho \mathbf{u})^{n}_{\mathrm{P}}}{\Delta t} + \sum_{f} F^{n}_{f} (\rho \mathbf{u})^{*}_{f} - \sum_{f} F^{*}_{d\mathbf{u}f} = 0 \tag{3.8}$$

Then the standard approach in incompressible flows is followed where the divergence is taken and we end up in getting a variable coefficient pressure Poisson equation (PPE).

$$\nabla \cdot \left(\frac{\nabla p}{\rho} \right) = \frac{\nabla \cdot \mathbf{u}^{*}}{\Delta t} + \nabla \cdot \left(\frac{\mathbf{g} \cdot \mathbf{x} \nabla \rho}{\rho} \right) + \sigma \nabla \cdot \left(\frac{\kappa \nabla f}{\rho} \right) \tag{3.9}$$

It must be noted that, a similar variable coefficient pressure Poisson equation is solved even in the work of Ghods and Herrmann [65], however, their PPE does not have additional gravitational and surface tension forces. Actually, they consider these two forces while predicting the provisional velocities and hence these two terms do not appear in their PPE. We now discretize the PPE (Eq. 2.18) suitably over every control volume and the final discrete form can be written as,

$$\Delta t \sum_f \left(\frac{\nabla p^*}{\rho}\right)_f \cdot \mathbf{S}_f = \sum_f F_{0f}^* + \Delta t \sum_f \left(\frac{\mathbf{g}\cdot\mathbf{x}\nabla\rho}{\rho}\right)_f \cdot \mathbf{S}_f + \sigma \Delta t \sum_f \left(\frac{\kappa \nabla f}{\rho}\right)_f \cdot \mathbf{S}_f \tag{3.10}$$

where

$$F_{0f}^* = \mathbf{u}_f^* \cdot \mathbf{S}_f \tag{3.11}$$

$\left(\frac{\nabla p^*}{\rho}\right)_f \cdot \mathbf{S}_f$ may then be discretized in a way similar to handling the diffusive flux.

After discretizing the PPE, we ultimately get a system of linear equations, which is solved by ILU pre-conditioned Krylov solver using [104]. It is be noted that the other gradient terms appearing on the right side of the pressure Poisson equation are also handled in a similar fashion and the treatment of these terms are identical. After getting the pressure field, we correct the fluxes at the faces as below.

$$F_f^{n+1} = F_{0f}^* - \Delta t \left(\frac{\nabla p^*}{\rho}\right)_f \cdot \mathbf{S}_f + \Delta t \left(\frac{\mathbf{g}\cdot\mathbf{x}\nabla\rho}{\rho}\right)_f \cdot \mathbf{S}_f + \sigma \Delta t \left(\frac{\kappa \nabla f}{\rho}\right)_f \cdot \mathbf{S}_f \tag{3.12}$$

Unlike the approaches in Mencinger and Žun [56] as well as Denner and Van Wachem [59], we do not have to add additional correction terms within the momentum interpolation to specifically account for a balanced force formulation. This is because, all our cell centroidal gradient quantities are calculated using their respective values at the cell faces themselves. Finally, we update the cell centroid velocities in the following way

$$\mathbf{u}_{\mathrm{P}}^{n+1} = \Delta t \left(\frac{\mathbf{u}_{\mathrm{P}}^*}{\Delta t} - \frac{\nabla p}{\rho} + \frac{\mathbf{g}\cdot\mathbf{x}\nabla\rho}{\rho} + \frac{\kappa\nabla f}{\rho}\right)_{\mathrm{P}} \tag{3.13}$$

It must be noted that, for a well balanced algorithm, all the centroidal gradient quantities used in updating the cell centroid velocities, must be obtained by employing least squares procedure.

3.1.3 Solution algorithm

The overall solution procedure is as follows.

1. Initialize all the variables suitably.
2. Assume $F_f^{n+1}=F_f^n$
3. Solve Eq. 3.7 iteratively to get provisional velocities.
4. Calculate provisional fluxes and iterate Eq. 3.9 upto desired tolerance level to get pressure field.
5. Update the fluxes at faces and calculate all the cell centroid velocities using Eq. 3.13
6. Advect the volume fraction by solving Eq. 2.4 iteratively and then calculate the fluid properties.
7. For the next time step calculations, go back to step 3 and repeat the same procedure until stopping criterion is met.

3.2 Consistent Treatment

In the present work, we emphasize on the need to use similar convective discretization technique in both momentum as well as volume fraction equations, and this is termed as consistent implementation (equation level consistent treatment) in our algorithm. In algebraic volume of fluid method, the convective term of advection equation is discretized by using some high-resolution scheme. The usage of high-resolution scheme limits the amount of numerical diffusion while ensuring convective boundedness criterion. Several high-resolution schemes [22, 23, 24, 29, 111] had been proposed in the past by various research groups. In the present work, CUBISTA proposed by Alves et al. [24] is employed for discretizing convective terms appearing in the volume fraction equation. Use of different schemes for discrete convection of volume fraction and momentum can be detrimental for particularly high density ratio convective flows which will be demonstrated later in the study. Therefore, from the view point of ensuring that the mass and momentum are handled at a discrete level in an identical fashion, we chose the same scheme to calculate the face values of

transported quantities namely momentum and volume fraction. Although one can use a first order upwind scheme as in [65] which would however lead to a considerably diffuse interface, thereby affecting the flow physics. In order to achieve consistency, instead of using CUBISTA scheme in the advection and momentum equations, the high resolution part of a similar interface capturing scheme proposed by Patel and Natarajan [29] can also be used and we believe that the results produced by this scheme will not change the solution considerably.

In the present study, we consider both balanced and unbalanced formulations. In contrast to the unbalanced algorithm, the balanced force algorithm always handles the dominant competing forces in an identical fashion at the discrete level. While this appears similar to the consistent approach, it must be noted that while consistency refers to discrete treatment of terms appearing across the equations, whereas, balanced formulation refers to the discrete treatment of terms appearing only in the momentum equations. In order to differentiate these aspects, we refer to the identical treatment of source terms appearing in the momentum equations as the balanced algorithm [53, 54, 56, 60].

3.3 Comparison With Alternative Algorithms

In this section, we summarize the major differences of our approach with some of the recent available algorithms for high density multiphase flows. Focussing on some of the key features of the present balanced force algorithm, we present the following points where our work has a clear distinction with some of the other approaches in open literature.

1. Unlike the approaches used in Francois et al. [53], Ghods and Herrmann [65] and Monatzaeri et al. [60], we employ an algebraic VOF method over three-dimensional unstructured meshes, which does not require any explicit interface reconstruction, making it a computationally cheaper method.

2. This methodology can be easily implemented in an unstructured grid framework, unlike those in [53, 60], which are restricted for uniform and non-uniform orthogonal meshes. The present methodology is similar to the lines of [59].

3. In the context of consistent treatment, the present work and the work presented by Denner and Van Wachem [59] are very different. We emphasize on the usage of similar convective scheme for discretizing the convective terms appearing in momentum as well as advection equations. But, in the work of Denner and Van Wachem [59], they employ CICSAM scheme for advecting volume fractions and central differencing scheme for transporting momentum.

4. In contrast to the work of Ghods and Herrmann [65], we use a mass conserving VOF approach and do not solve an additional equation (continuity) for getting provisional density fields. This ensures that the mass and momentum errors remain small, and hence mimicking an approximate discrete conservation.

5. In order to calculate provisional momentum, apart from the pressure gradient term, we also drop out the gravitational and the surface tension terms from the momentum equations. This constructs a Poisson equation involving pressure, gravitational and surface tension effects, similar to the work in [64].

We now investigate the effects of force balancing and consistent treatment in binary fluid flows through a variety of test cases in the following section.

3.4 Results and Discussion

The methodology and algorithm presented in previous sections are implemented in an in-house code, which is build on a fully three-dimensional hybrid unstructured grid finite volume framework. In the studies below, we consider the effects of both inconsistent and unbalanced approaches, and studies are carried out using "Balanced & Consistent" (BC), "Balanced & Inconsistent" (BI), "Unbalanced & Consistent" (UC) and "Unbalanced & Inconsistent" (UI) algorithms. The word "balanced" represents force balancing between corresponding source terms at discrete level and "consistent" is for using same convective discretization technique (CUBISTA) for advection as well as momentum equations. It is to be noted that, for balanced framework, we have implemented the same least squares approach for the calculations of all gradient quantities appearing in the source term of the momentum equations. For an unbalanced approach, we adopt the least squares method for pressure gradient calculation, but the calculation of gradient quantities appearing in gravitational as well as surface tension terms are carried out using Green Gauss reconstruction.

We now present a number of test cases of varying complexities in the viscous and inviscid regime, to illustrate the ability of the present approach in handling high density ratio multiphase flows.

3.4.1 Static droplet

In order to demonstrate the benefits of force balancing, we present this numerical test case of a three-dimensional static inviscid bubble, earlier performed by Williams et al. [6] and adopted by different research groups [53, 54]. Ideally, in this particular case, given the exact value of curvature, surface tension force should exactly balance the pressure drop, resulting in machine precise values of velocities in the entire domain and a pressure jump of "$\sigma\kappa$" across the interface. The test case includes a computational domain of size $8 \times 8 \times 8$ with a bubble of radius $R = 2$ placed exactly at its center. Density inside the bubble is 1, while the density of the surrounding fluid is varied from 10^1 to 10^5. Surface tension coefficient σ is set to 73, which ideally should result in a pressure jump of $\Delta P_{exact} = 73$ across the interface. Two types of computational grids are chosen, one with $40 \times 40 \times 40$ orthogonal hexahedral cells and another with approximately 77000 non-orthogonal tetrahedral cells. For evaluating the performance of different algorithms, the maximum magnitude of spurious currents and the error in pressure jump are examined. The simulated pressure jump is evaluated by taking the difference between maximum and minimum value of pressure in the entire domain and is given by

$$\Delta p_{max} = p_{max} - p_{min}$$

and the relative error is calculated as:

$$E(\Delta p)_{max} = \frac{|\Delta p_{max} - \Delta p_{exact}|}{\Delta p_{exact}}$$

Employing BI and UI algorithms, the results are presented in Tables 3.1 and 3.2 for orthogonal and non-orthogonal cells, respectively. It must be noted that in this study, our focus is only on the amount of force balancing achieved by different algorithms and hence only an inconsistent approach is used in either case. The results clearly indicate the superiority of balanced force algorithm over the unbalanced counterpart. Machine precise values of spurious currents clearly indicate the effectiveness of the proposed balanced framework. Simulations are performed in both structured as well as unstructured meshes and the performance is equally

well even with extremely high-density ratio of 10^5. Also Figs. 3.1(a) and 3.1(b) show the jump in pressure after time $t = 50\Delta t$ along the $x - z$ plane at $y = 4$ i.e mid plane of the computational domain with a density ratio of 10^3. In case of UI algorithm, the maximum and the minimum values of pressure are 82.26 and -16.34, whereas for BI algorithm, these are 73.0 and -9.00 $\times 10^{-11}$, respectively. As a result of perfect balance achieved between surface tension term and the associated pressure gradient, we noticed that the exact value of pressure jump has been obtained with the balanced framework. The grid independent results for this case have been shown in Table 3.3. Next, we performed the same test again for a density ratio of 10 over $20 \times 20 \times 20$ orthogonal hexahedral meshes, but instead of specifying the exact value of curvature, we chose to calculate it numerically. Table 3.4 shows the amount of spurious currents generated after one and 50 time steps employing BI and UI algorithms and the result is compared against the work of Francois et al.[53], where they used convolution technique for curvature estimation. The trend of the spurious currents generation for BI algorithm is almost the same as that of Francois et al. [53]. But for UI algorithm, an increase in the amount of spurious currents is noticed both after single and 50 Δt, when compared against the outcome BI algorithm.

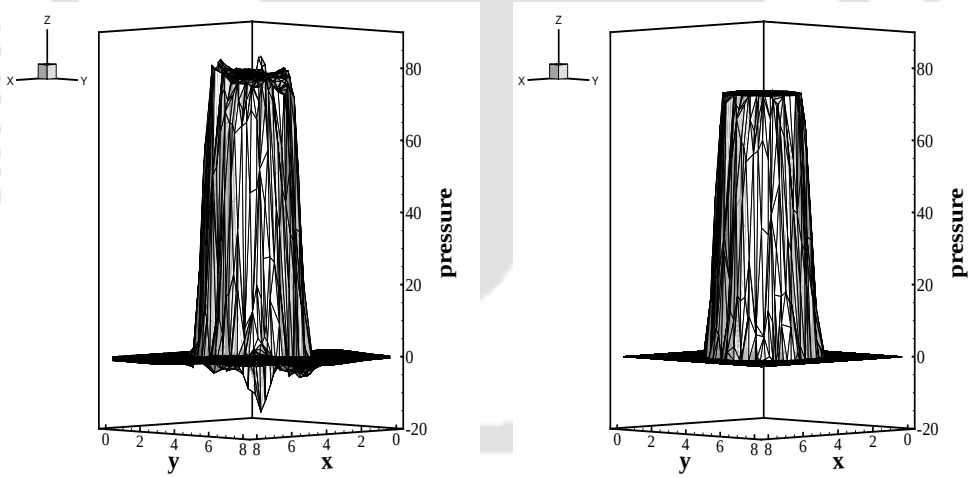

(a) (b)

Figure 3.1: Computed pressure jump after 50 Δt for static inviscid bubble along the mid plane of the computational geometry by employing (a) UI and (b) BI algorithms. The domain is $8 \times 8 \times 8$ with approximately 77000 tetrahedral cells.

Time		ρ_2/ρ_1	$\|\mathbf{u}\|_{\mathbf{max}}$	$E(\Delta p_{max})$
$t = \Delta t$	Unbalanced Formulation	10^1	2.58×10^{-4}	8.30×10^{-14}
		10^3	3.15×10^{-4}	8.90×10^{-12}
		10^5	3.16×10^{-4}	3.63×10^{-12}
	Balanced Formulation	10^1	1.11×10^{-17}	8.30×10^{-14}
		10^3	4.50×10^{-16}	8.90×10^{-12}
		10^5	7.70×10^{-16}	3.63×10^{-12}
$t = 50\Delta t$	Unbalanced Formulation	10^1	0.011	1.087
		10^3	0.013	1.527
		10^5	0.013	1.533
	Balanced Formulation	10^1	1.27×10^{-17}	9.00×10^{-14}
		10^3	5.09×10^{-16}	9.85×10^{-12}
		10^5	7.00×10^{-16}	4.52×10^{-12}

Table 3.1: Magnitude of maximum velocity and error in pressure for a three-dimensional static inviscid bubble after time $t = \Delta t$ and $t = 50\Delta t$ with varying density ratios and when exact curvature is specified. The computational grid is 40 $\times$ 40 $\times$ 40 orthogonal hexahedral cells.

Time		ρ_2/ρ_1	$\|\mathbf{u}\|_{\mathbf{max}}$	$E(\Delta p_{max})$
$t = \Delta t$	Unbalanced Formulation	10^1	8.67×10^{-4}	7.13×10^{-11}
		10^3	9.56×10^{-4}	4.09×10^{-10}
		10^5	9.57×10^{-4}	3.07×10^{-10}
	Balanced Formulation	10^1	2.08×10^{-14}	7.13×10^{-11}
		10^3	2.48×10^{-13}	4.09×10^{-10}
		10^5	2.57×10^{-13}	3.07×10^{-10}
$t = 50\Delta t$	Unbalanced Formulation	10^1	0.0315	2.38
		10^3	0.0365	2.98
		10^5	0.0366	3.00
	Balanced Formulation	10^1	6.14×10^{-14}	9.34×10^{-11}
		10^3	7.60×10^{-13}	6.28×10^{-10}
		10^5	7.12×10^{-13}	6.80×10^{-10}

Table 3.2: Magnitude of maximum velocity and error in pressure for a three-dimensional static inviscid bubble after time $t = \Delta t$ and $t = 50\Delta t$ with varying density ratios and when exact curvature is specified. The computational grid is $\approx 77 \times 10^3$ non-orthogonal tetrahedral cells.

Time	grid	$\|\mathbf{u}\|_{\mathbf{max}}$	$E(\Delta p_{max})$
$t = \Delta t$	20^3	2.47×10^{-17}	2.08×10^{-13}
	40^3	4.50×10^{-16}	8.90×10^{-12}
	80^3	6.30×10^{-16}	1.70×10^{-12}
$t = 50\Delta t$	20^3	7.56×10^{-17}	1.35×10^{-13}
	40^3	5.09×10^{-16}	9.85×10^{-12}
	80^3	8.63×10^{-16}	3.50×10^{-12}

Table 3.3: Grid Independence results for three dimensional static droplet case.

	Balanced (BI)	Unbalanced (UI)	Francois et al. [53]
$t = \Delta t$	0.005	0.13	0.00487
$t = 50\Delta t$	0.208	1.8	0.163

Table 3.4: Maximum spurious currents $|\mathbf{u}|_{\mathbf{max}}$ generated after one and 50 time steps for the case of a three-dimensional static inviscid bubble. Density ratio is 10 and the curvature is calculated numerically.

3.4.2 Partially filled static tank

Previous test case demonstrated the force balancing between surface tension term and the associated pressure gradient using different algorithms. In this case, the intention is to check the balancing achieved between gravitational body force term and the associated pressure gradient. Computational domain chosen for this test case is a two-dimensional square cavity of size 1×1, and it is discretized into 4682 hybrid cells (combination of hexahedral and prism cells) and 8120 prism cells as shown in Fig. 3.2. Initially the domain is half filled with heavier fluid and all the boundaries are treated as walls, except for the top one, which is open to atmosphere. Ideally, after single time step, one can expect the development of pressure field inside the computational domain with negligible velocity fields. In order to check the performance of different algorithms, we measure the maximum magnitude of spurious currents and the relative error in the values of pressure jump across the interface (similar to test case 1).

Analytically, the exact jump in the pressure field across the interface (when the ground level is at the bottom of the domain of size 1×1 and the fluid interface is at 0.5) is

$$\Delta p_{max} = 0.5\ g\ (\rho_1 - \rho_2)$$

where g is the acceleration due to gravity in the negative y-direction and ρ_1 and ρ_2 are the densities of heavier and lighter fluids, respectively. Tables 3.5 and 3.6 show the results for two different grids using UI and BI algorithms. Similar to the previous test case, our focus is only on evaluating the force balancing achieved by different algorithms, and hence in this case as well, an inconsistent approach is used in either case. Results are showed after Δt and $50\Delta t$. It should be noted that the pressure field after the first time step is identical for balanced and unbalanced framework.

This is because of the fact that the actual unbalancing occurs only after the solution of pressure Poisson equation, i.e when the final velocities are updated. From the table we can observe that a huge amount of spurious currents are generated in case of an unbalanced framework, and it can also be seen that the magnitude of these spurious currents increases with the increase in the density ratio of the two fluids. Figure 3.3 shows the distortion occurring at the fluid interface after a time of $50\Delta t$, when unbalanced algorithm is used along with a density ratio of 10^5 : 1. On the other hand, as expected, balanced framework generates machine precise values of the spurious currents with negligible errors in the pressure jump across the interface.

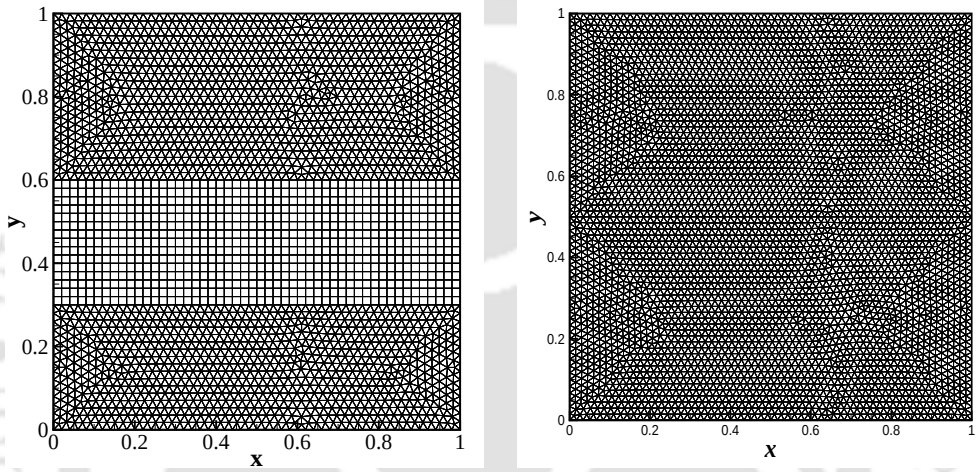

(a) (b)

Figure 3.2: Computational grid for simulating partially filled static tank. (a) 4682 hybrid cells and (b) 8120 prism cells.

3.4.3 Droplet convection

In this numerical experiment, the motivation is to study the impact of consistent formulation in handling variable density flows. This test case is initially proposed by Bussmann et al. [64], wherein a three-dimensional droplet is being convected through a lighter medium in the absence of gravitational pull and surface tension forces. Both the fluids are assumed to be inviscid and the computations are performed in a $3 \times 3 \times 3$ cubical enclosure with two different grid arrangements viz. an orthogonal $75 \times 75 \times 75$ hexahedral cells and another with approximately 1.6

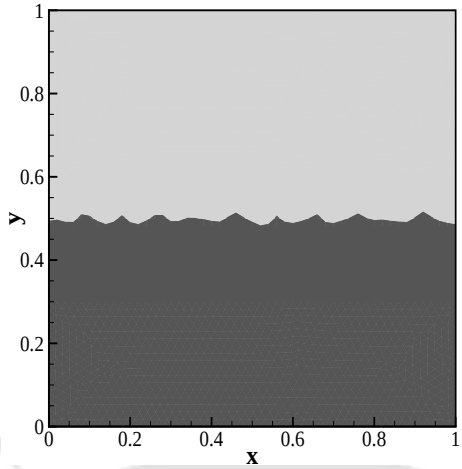

Figure 3.3: Distortion of the interface (volume fraction $f = 0.5$) after $t = 50\Delta t$, using UI algorithm and with a density ratio of 100000:1.

Time		ρ_2/ρ_1	$\|\mathbf{u}\|_{max}$	$E(\Delta p_{max})$
Δt	Unbalanced Formulation	10^1	0.92	2.72×10^{-18}
		10^3	124.708	5.38×10^{-17}
		10^5	125.074	1.20×10^{-19}
	Balanced Formulation	10^1	2.55×10^{-15}	2.72×10^{-18}
		10^3	2.42×10^{-15}	5.38×10^{-17}
		10^5	1.11×10^{-15}	1.20×10^{-19}
$50\Delta t$	Unbalanced Formulation	10^1	13.46	0.72
		10^3	271.39	1.094
		10^5	734.94	0.988
	Balanced Formulation	10^1	3.56×10^{-15}	4.89×10^{-15}
		10^3	2.50×10^{-15}	6.85×10^{-16}
		10^5	3.00×10^{-15}	3.97×10^{-19}

Table 3.5: Magnitude of maximum velocity and maximum pressure difference for a two-dimensional static tank after Δt and $50\Delta t$ with varying density ratios. The time step Δt is 10^{-3} and the grid is composed of 4682 hybrid cells.

Time		ρ_2/ρ_1	$\lvert\mathbf{u}\rvert_{max}$	$E(\Delta p_{max})$
Δt	Unbalanced	10^1	3.18	1.00×10^{-15}
	Formulation	10^3	425.00	7.37×10^{-16}
	Balanced	10^1	4.09×10^{-15}	1.00×10^{-15}
	Formulation	10^3	1.35×10^{-14}	7.37×10^{-16}
$50\Delta t$	Unbalanced	10^1	20.09	0.96
	Formulation	10^3	2125.0	1.56
	Balanced	10^1	5.74×10^{-14}	2.85×10^{-15}
	Formulation	10^3	1.61×10^{-14}	6.94×10^{-16}

Table 3.6: Magnitude of maximum velocity and maximum pressure difference for a two-dimensional static tank after Δt and $50\Delta t$ with varying density ratios. The time step Δt is 10^{-3} and the grid is composed of 8120 prism cells.

million non-orthogonal tetrahedral cells (refer Fig. 3.4). Initially, the droplet is positioned in a quiescent medium at $x, y, z = (1.0, 1.5, 1.5)$ and is given an initial velocity $\mathbf{u} = (1.0, 0.0, 0.0)$. Simulations are performed with two different sets of density ratio (10^3 and 10^6), until the droplet has travelled a unit distance in the x direction. This test case emphasizes on the need to have consistent treatment of the convective fluxes across different equations and hence we performed the simulations using BI and BC algorithms. Final droplet shape for a density ratio of 10^3 and 10^6 are shown in Figs. 3.5 and 3.6, respectively using hexahedral cells and in Fig. 3.7 for tetrahedral cells. Wiggles on the rear end of the droplet can be clearly seen with the inconsistent algorithm for both the density ratios, while for the consistent algorithm, even for a very high-density ratio of 10^6, very minimal amount of surface deformation has been noticed. One of the possible reasons behind the appearance of wiggles is the erroneous momentum transfer between lighter and heavier fluids. Table 3.7 shows the shape error (refer Eq. 3.14) for different grids using BC algorithm. As it can be seen from the table, the shape error converges with mesh refinement for hexahedral as well as tetrahedral meshes.

$$\varepsilon(\%) = \frac{\sum\limits_{Ncells}\left(f_i V_i\right)_{initial} - \sum\limits_{Ncells}\left(f_i V_i\right)_{final}}{\sum\limits_{Ncells}\left(f_i V_i\right)_{initial}} \times 100 \tag{3.14}$$

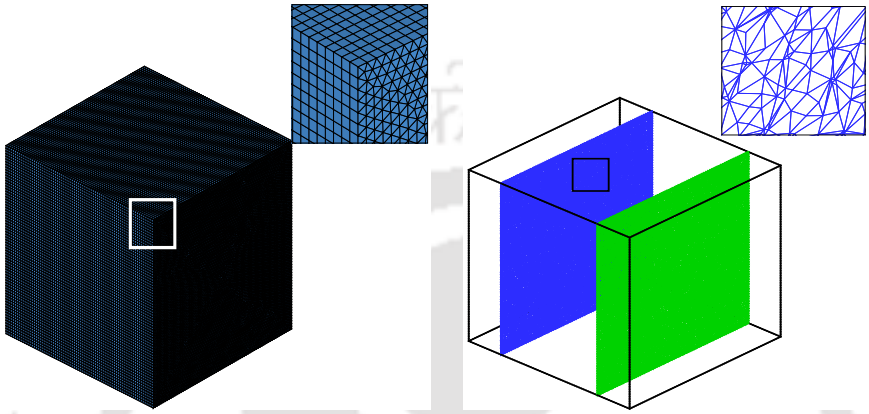

(a) (b)

Figure 3.4: Hybrid mesh used for the droplet convection case. In the inset view, zoomed portion of the grid is shown.

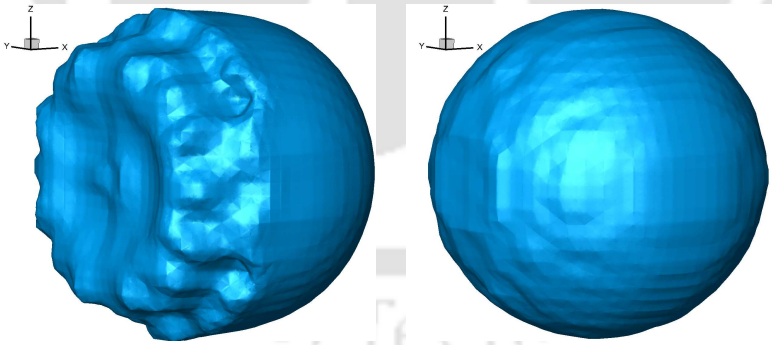

(a) (b)

Figure 3.5: Iso-surface of volume fraction $f = 0.5$ for inviscid droplet convection after time $t = 1.0$ with density ratio $= 10^3$ over hexahedral cells. Results are shown by employing (a) BI and (b) BC algorithms.

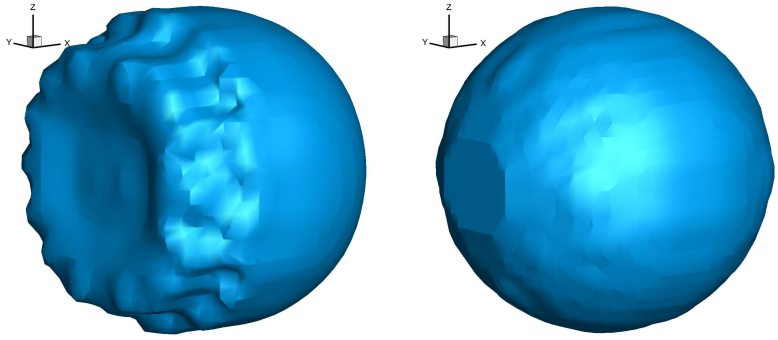

(a) (b)

Figure 3.6: Iso-surface of volume fraction $f = 0.5$ for inviscid droplet convection after time $t = 1.0$ with density ratio $= 10^6$ over hexahedral cells. Results are shown by employing (a) BI and (b) BC algorithms.

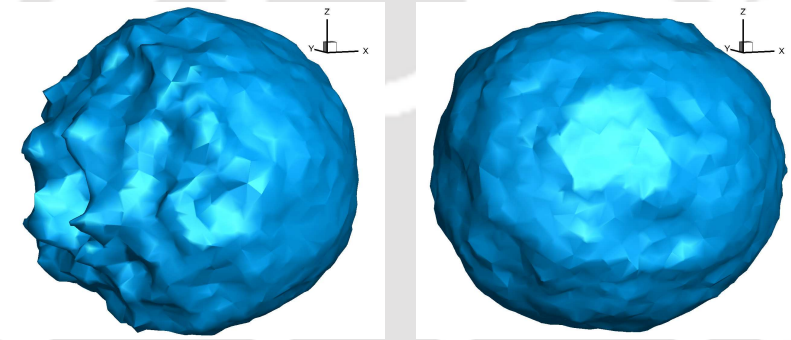

(a) (b)

Figure 3.7: Iso-surface of volume fraction $f = 0.5$ for inviscid droplet convection after time $t = 1.0$ with density ratio $= 10^3$ over tetrahedral cells. Results are shown by employing (a) BI and (b) BC algorithms.

	grid	ε
Orthogonal	50^3	0.0125
	100^3	0.00384
Non-orthogonal	4 lac (approx.)	1.94
	8 lac (approx.)	1.54

Table 3.7: Shape error for droplet convection test.

3.4.4 Column filling

This is another test case, where we highlight the need for consistent treatment of convective terms under the effect of gravitational pull. Filling of the liquid column with heavier fluid against the gravity is among one of the typical test cases in this regard. Herein, we selected a column with aspect ratio 1:2. It is being filled with heavier fluid from the bottom as shown in Fig. 3.8(a). Both the fluids are considered to be inviscid with slip boundary conditions applied to the side walls. The computational domain is discretized into 6400 graded non-uniform hexahedral cells as shown in Fig. 3.8(b), so that the flow actually passes through different mesh spacings. Initially, the level of heavier fluid in liquid column is up to 0.1 units, while rest of the domain is occupied by lighter fluid. The column is then allowed to be filled from the bottom side with heavier fluid entering at a velocity $\mathbf{u} = (0.0, 1.0, 0.0)$. Simulations are performed until the domain is completely filled with heavier fluid. As the fluids under consideration are inviscid with slip boundary condition applied to the side walls, ideally both the fluids should move up with constant inlet velocity. Computations are carried out with two different density ratios and the contour of volume fraction (f=0.5) with velocity vectors are shown in Fig. 3.9. The results are shown at a time instance, when the fluid interface is about to reach a level of 1.7 in the column. In order to highlight the differences in results, only small portion of the computational domain, which is near to the interface is shown. From the results, we noticed that for low-density ratio, the outcome of all the three algorithms are almost identical. But in case of higher density ratio, a noticeable difference between the results of consistent and inconsistent formulation can be seen. It is observed that the BC algorithm performed equally well, irrespective of the density ratio chosen, but for BI algorithm, a maximum deviation of 10% in the velocity is noticed. As the erroneous velocities are on the lighter side of the fluid, the interface, however, remains straight in both the cases. The simulations are also performed on an irregular triangular mesh with density ratio of 1000 and the vector plot is shown in Fig. 3.10 for BC and BI algorithms. While the error in velocity for consistent schemes is around 1-2 % and higher than for a hexahedral mesh, the results of inconsistent schemes show a distorted interface and leads to physically incorrect solutions. The reader must also note the contrast of the present results with the static tank case, wherein the consistent or inconsistent formulation plays no role at all.

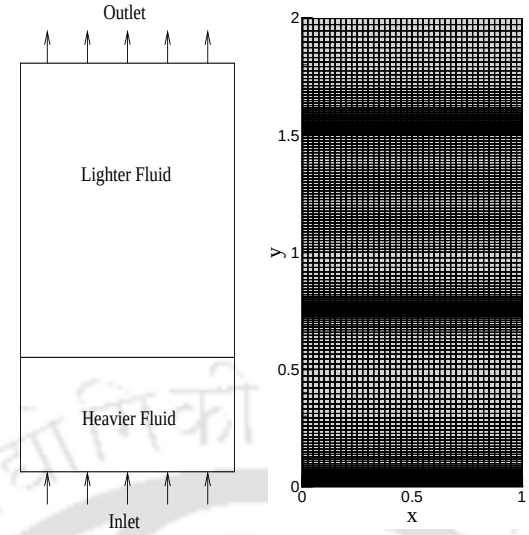

(a) (b)

Figure 3.8: (a) Schematic diagram and (b) computational mesh for column filling case.

3.4.5 Droplet detaching from wall

In the previous two test cases, the effect of surface tension force was not considered. Hence, in order to highlight the effects of consistency in the presence of both surface tension as well as gravitational forces, we present this test case, wherein a droplet is being detached from the solid wall under the influence of gravity. The schematic diagram along with the initial and boundary conditions are shown in Fig. 3.11. The computational domain is discretized into 10000 hexahedral cells. Physical parameters for this case are $\mu_1 = 10$, $\mu_2 = 0.1$, $g = 0.98$ and $\sigma = 1.96$. Static contact angle $\theta = 50^\circ$ has been imposed on the top wall and the other three walls are open to atmosphere. Figures 3.12 and 3.13 show the temporal evolution of the droplet using two different density ratios of 100 and 10000, respectively. Results shown in Figs. 3.12 (a) and 3.13 (a) are the outcomes of the simulations performed using the BI algorithm, whereas Figs. 3.12 (b) and 3.13 (b) are the simulation outcomes corresponding to the BC algorithm. In the case of low density ratio computations, the differences are unnoticeable for both the algorithms, while for the higher density ratio case, the differences can be clearly noticed. The differences in the results of consistent and inconsistent algorithms in the later case is due to the dominant convective currents. We can easily notice that the inconsistent algorithm is unable

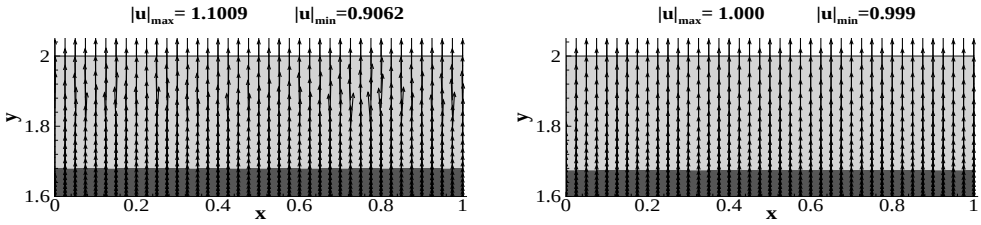

(a)

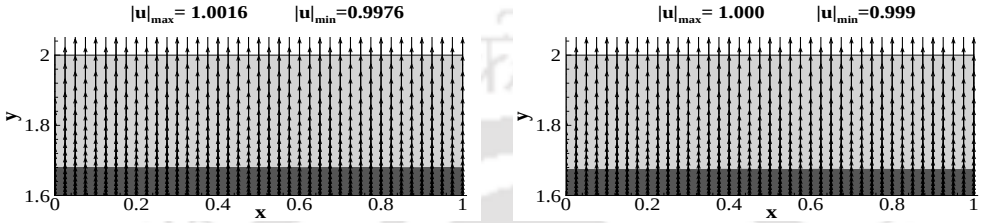

(b)

$\rho_1/\rho_2 = 1000$ $\rho_1/\rho_2 = 5$

Figure 3.9: Contour of volume fraction $f = 0.5$ and velocity vector for column filling case with two different density ratios. Darker and lighter shade represent the heavier and lighter fluids, respectively. Results are shown by employing (a) BI and (b) BC algorithms, when the fluid interface is about to reach a level of 1.7 m.

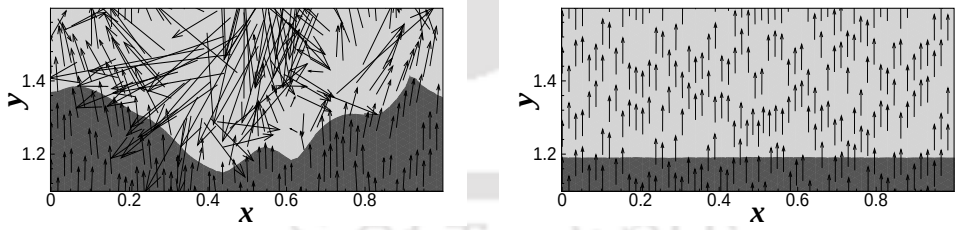

(a) (b)

Figure 3.10: Contour of volume fraction $f = 0.5$ and velocity vector for column filling case using triangular meshes. Darker and lighter shade represent the heavier and lighter fluids, respectively. Results are shown by employing (a) BI and (b) BC algorithms.

to maintain the sphericity of the droplet. Thus, not only the force balancing, but in some cases, consistency also plays an important role for getting accurate results.

After comparing all the above test cases using different algorithms, we now conclude that in almost all practical cases in multiphase flows, in addition to the dominant convection currents, it routinely involves forces due to surface tension and gravity, therefore, it is important for an algorithm to account for both, a consistent formulation and a balanced algorithm. Importantly, as we have shown, it is only in the high density ratio regimes that there could be differences between the two algorithms because of the dominant nature of the convective currents. However, this is indeed not true universally, and we now discuss problems wherein either of the algorithm may sometimes give ideally correct solution.

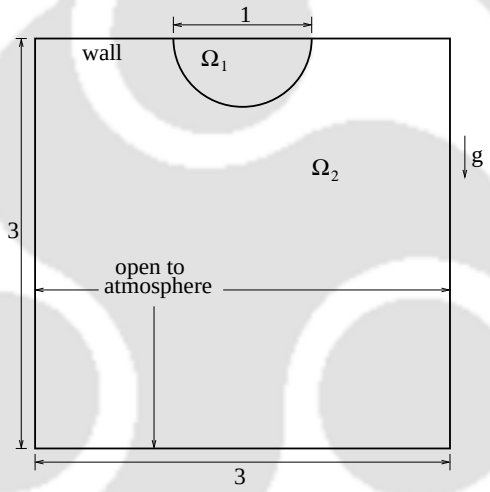

Figure 3.11: Schematic diagram and boundary conditions for a 2D droplet detaching from solid wall. Ω_1 and Ω_2 are the regions of heavier and lighter fluids, respectively.

3.4.6 Two-dimensional bubble rise

This test case is presented as an algorithm validation against a benchmark problem, where consistency and force balancing do not effect the results significantly. The problem defines a two-dimensional bubble with an initial radius of 0.25, centered at $(x, y) = 0.5, 0.5$ in a quiescent medium as shown in Fig. 3.14. The size of the computational domain is 1×2 and is discretized into 5000 hexahedral cells with a uniform

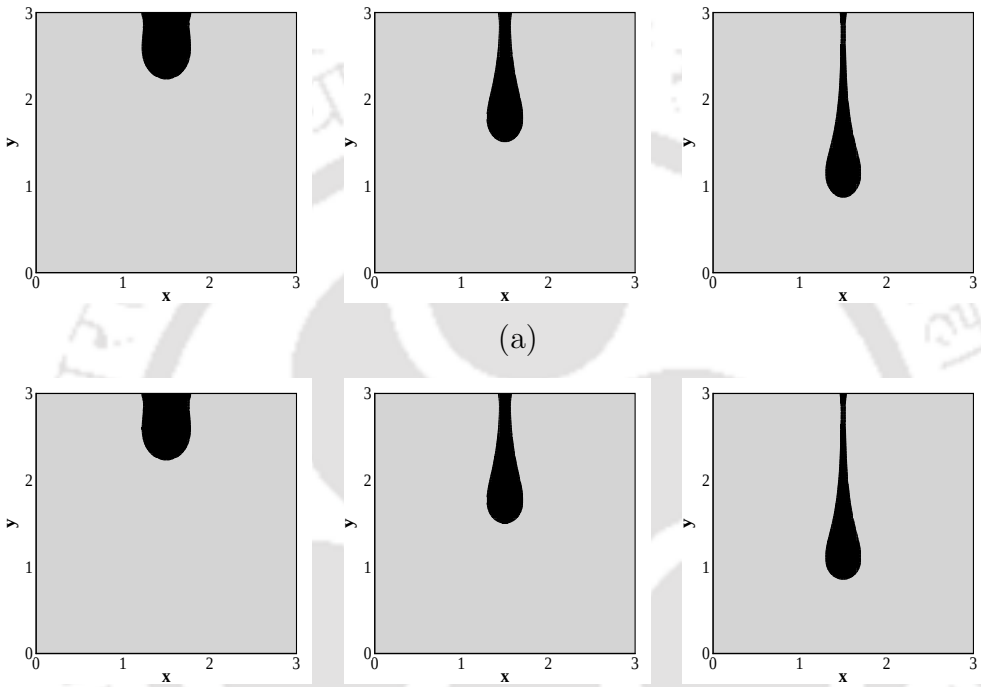

Figure 3.12: Temporal evolution of a single droplet detaching from the wall at time $t = 2.5$, 5.0 and 6.250, with a density ratio of 100. Simulations are performed using (a) BI and (b) BC algorithms.

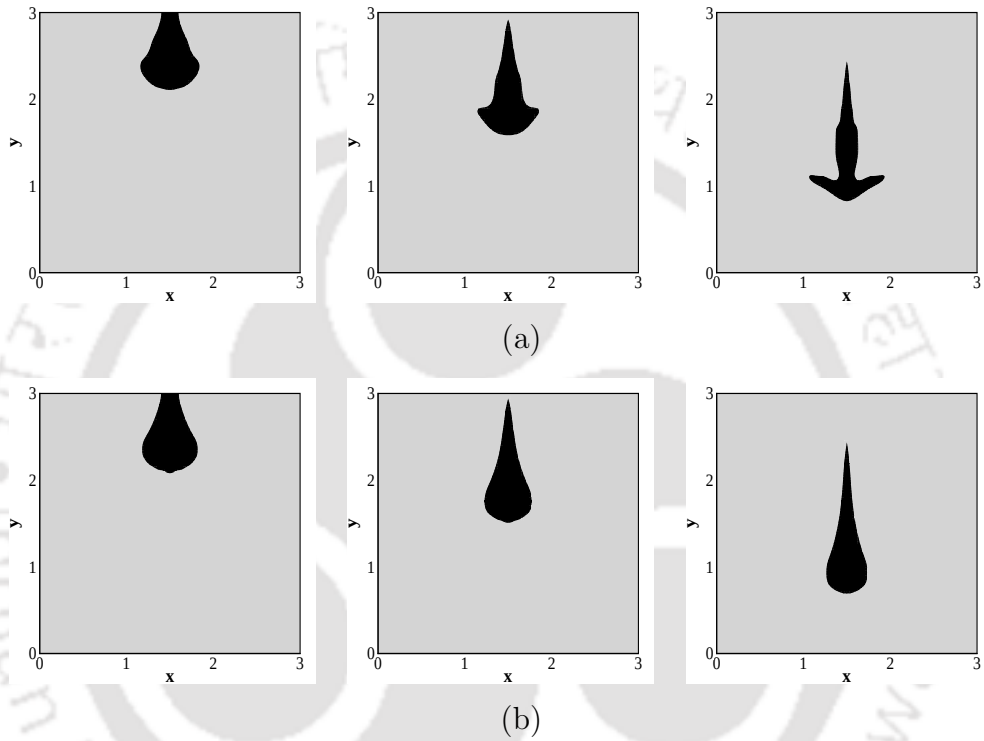

Figure 3.13: Temporal evolution of a single droplet detaching from the wall at time $t = 2.0$, 3.0 and 4.0, with a density ratio of 10000. Simulations are performed using (a) BI and (b) BC algorithms.

grid spacing of 1/50. Hysing et al. [1] performed this numerical experiment with two different sets of properties, one with a large variation in density and viscosity ratio, while the other one is for a lesser property variation. Here, we present the results for the case with higher density ratio, as it is more significant as compared to the one with lesser property variations. Physical parameters for this case are $\rho_1 = 1000$, $\rho_2 = 1$, $\mu_1 = 10$, $\mu_2 = 0.1$, $g = 0.98$ and $\sigma = 1.96$. Results are presented in terms of temporal variation of the rising velocity of the bubble and the vertical position of its center of mass. For all the four algorithms (UI, UC, BI and BC), results are plotted in Fig. 3.15. As compared to the outcome of balanced algorithms (where negligible initial spurious currents are produced), the results of unbalanced algorithm show a sharp increase in the rise velocity during the initial stages of bubble rise. However, with time, as the bubble gains momentum, these spurious currents are overcome by its inertia. Apart from this, it is also observed from the rise velocity plot, that there is a variation in the terminal velocity achieved by the bubble using different algorithms. However, terminal velocity is not mentioned as the benchmark quantity, but from the plots presented in the work of Klostermann et al. [5] and Hysing et al. [1], it can be observed that the terminal velocity is more than 0.175. In the present work, using unbalanced formulation, the terminal velocity achieved by the bubble is less than 0.175. And it can be noticed from the plot, that its value is approximately 0.15 and 0.16 for UC and UI algorithms, respectively. But in case of balanced algorithm, the terminal velocities are more than 0.175 and also no initial abrupt rise in velocities can be seen.

The benchmark quantities are listed in Table 3.8. As far as benchmark quantities are concerned, although there are not much differences between all the four algorithms, but the lower value of terminal velocity and the initial abrupt values of rise velocity generated in the case of unbalanced algorithm clearly emphasizes on the need for force balancing. Figure 3.16 shows the comparison of the bubble shape using BC algorithm at time $t = 3.0$ with the published results of Hysing et al. [1]. Table 3.9 shows the grid independent study using BC algorithm. In addition to this, the mass conservation error is also calculated for this case using BC algorithm and its value has been found to be less than 0.03 %.

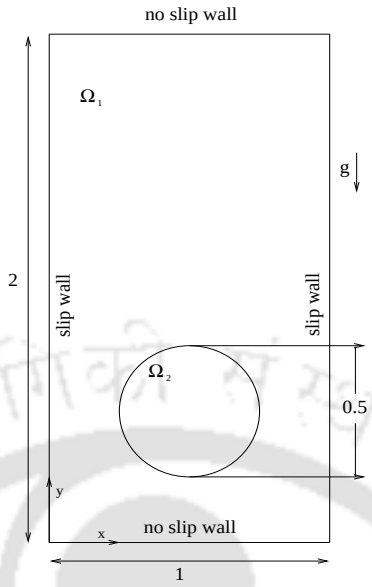

Figure 3.14: Computational domain for 2D bubble rise problem with initial set up and boundary conditions. Ω_1 and Ω_2 are the regions of heavier and lighter fluid, respectively.

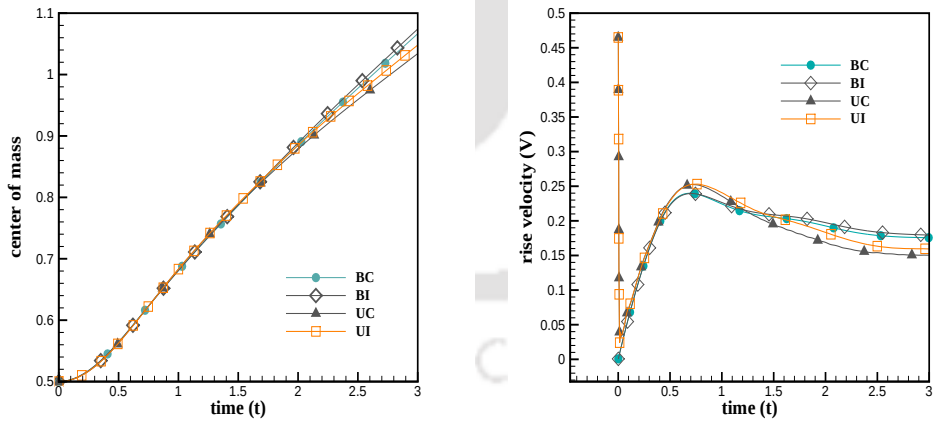

(a) (b)

Figure 3.15: Temporal evolution of (a) center of mass and (b) rising velocity for 2D bubble rise problem.

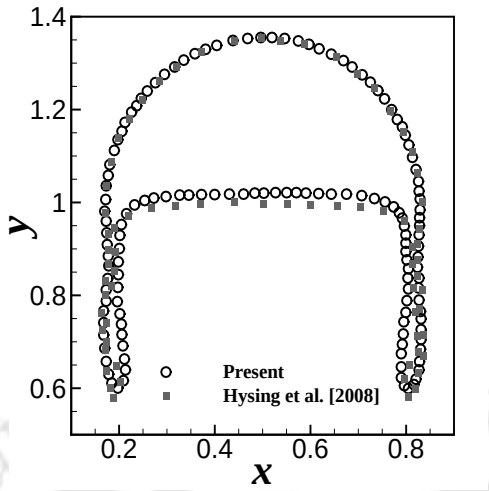

Figure 3.16: Comparison of the bubble shape at time $t = 3.0$ with the benchmark solution of Hysing et al. [1].

	a	b	c	d	e	f
V_{max}	0.2530	0.2525	0.2394	0.2398	0.2388	0.2514
$t(V_{max})$	0.761	0.707	0.705	0.692	0.6875	0.7281
$y_c(t = 3)$	1.0478	1.034	1.0742	1.0665	1.0862	1.1249

Table 3.8: Comparison of various benchmark quantities by (a) UI, (b) UC, (c) BI and (d) BC algorithms with the published results of (e) Klostermann et al. [5] and (f) Hysing et al. [1]

grid	V_{max}	$t(V_{max})$	$y_c(t = 3)$
50×75	0.2398	0.692	1.066
75×100	0.2470	0.721	1.087
100×200	0.2478	0.722	1.094

Table 3.9: Grid independent study for two-dimensional bubble rise problem using BC algorithm.

3.4.7 Three-dimensional collapse of water column with obstacle

After demonstrating the importance of force balancing and consistency in the previous test cases, we now test the capability of "Balanced & Consistent" algorithm for simulating experimental problems. In this test case, a water column is allowed to collapse against an obstacle [112] inside an enclosure. Problem setup with initial condition is shown in Fig. 3.17. The computational domain is of size $3.22 \times 1 \times 1$ which is discretized into non-uniform 595953 hexahedral cells. All the boundaries are treated as no-slip walls except for the top one, which is open to atmosphere. Initially, a water column is maintained at a height of 0.55 m on the right side of the domain as shown in Fig. 3.17, and then suddenly it is allowed to flow and strike the obstacle and the other end of the enclosure. Simulations are carried out for 6 seconds using BC and UI algorithms and the snapshots of the water front are shown in Fig. 3.18 at time 1.2 and 2 seconds. It can be clearly observed from the contour plots that at time $t = 2.0$ sec, a void has been noticed with the UI algorithm (Fig. 3.18(b)), which is not the case with experimental results as reported in [112]. Water column height at three different locations has been plotted for BC algorithm and is compared with the published results as shown in Fig. 3.19. We remark here, that although the computed results do not show excellent agreement with the experimental findings, similar deviations have been reported in numerical investigations in the past [113, 114, 115, 116, 117, 118, 119, 120]. The present test case demonstrates the efficacy of the proposed BC solver to handle problems driven by large body forces in three-dimensions with the results from the present solver showing a fair agreement in terms of water column height with experimental measurements. However, the fluid flow in this problem is mainly driven by the gravitational force and hence the ability of the solver to handle surface tension dominant flows can not be demonstrated by this test case. Therefore, in the next and final test case, we present the simulation of a three-dimensional droplet impact over thin liquid film, where both gravitational and surface tension forces are of equal importance.

3.4.8 Three-dimensional droplet falling over thin liquid film

Finally, we numerically investigate the impact of a three-dimensional liquid droplet falling over thin liquid film. This typical test case has dominant surface tension and

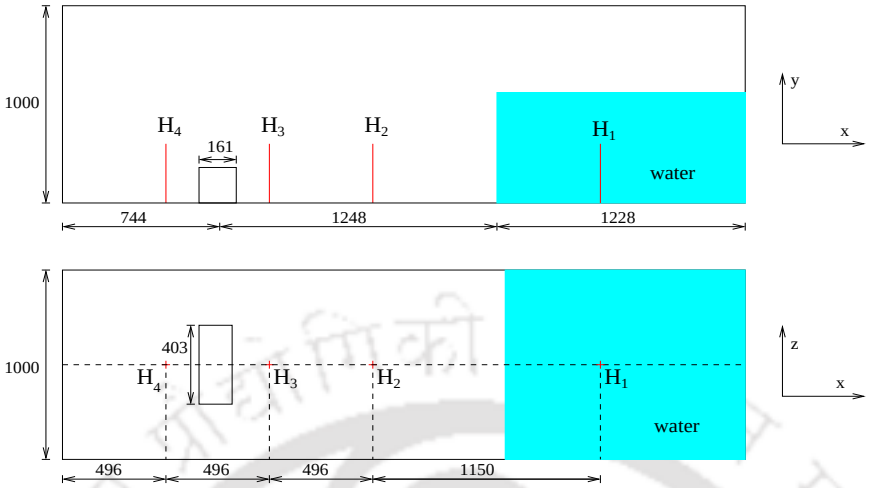

Figure 3.17: Schematic diagram for three-dimensional collapse of water column against an obstacle. (units: mm)

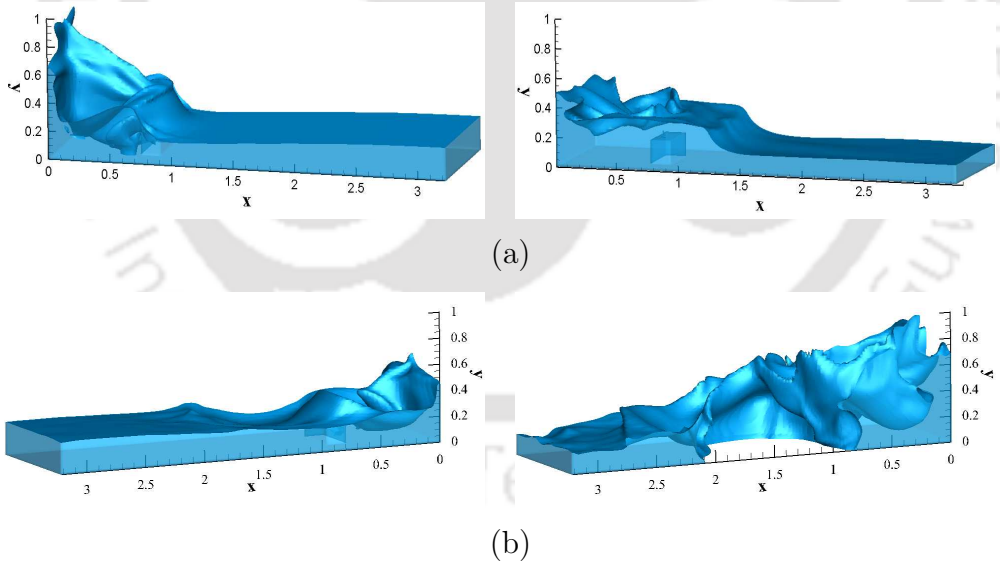

Figure 3.18: Temporal evolution of three-dimensional water column collapsing against an obstacle at time $t = 1.2$ and 2.0 using (a) BC and (b) UI algorithms.

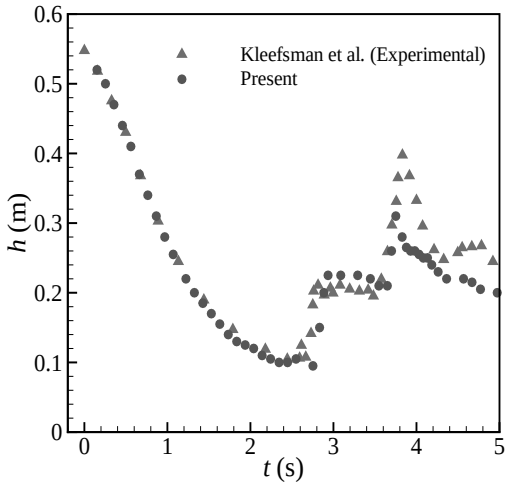

(a)

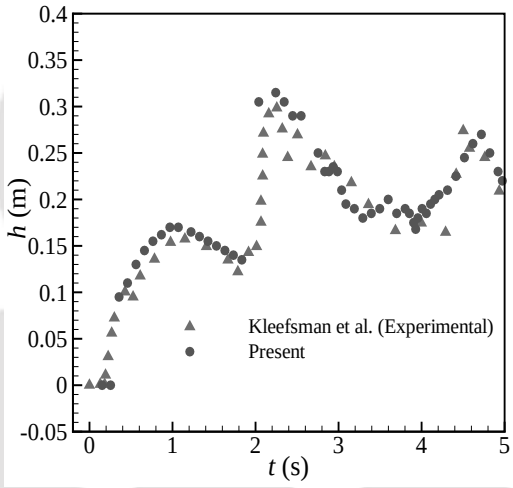

(b)

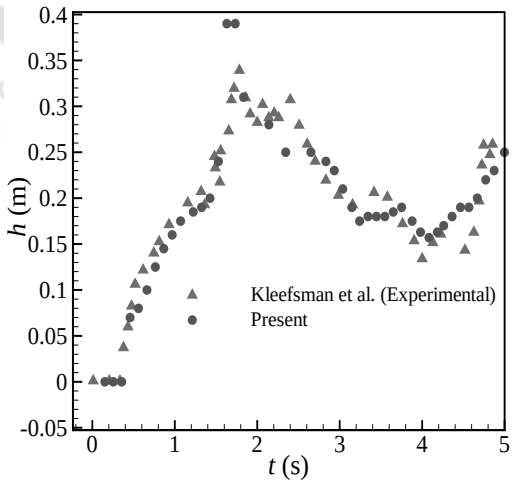

(c)

Figure 3.19: Comparison of water column height with the published literature using BC algorithm at locations (a) H1, (b) H2 and (c) H3 .

gravitational effects and we choose the values of different non-dimensional parameters viz. Weber number (We), Reynolds number (Re), Froude Number (Fr) and non-dimensional film thickness (H) according to [3, 4].

Initially, the droplet is placed 2.8 diameters above the liquid film with a uniform velocity U_o. The computational domain chosen for this test case is of size $6D_o \times 6D_o \times 6D_o$, which is discretized into 512000 non-uniform hexahedral cells. Top boundary is open to atmosphere while the remaining boundaries are treated as walls. Simulations are performed with We=250, Re=11294, Fr=363 and H=0.116. Iso-surface plots of volume fraction f=0.5 at different time instance is shown in Fig. 3.20 using UI and BC algorithms. We noticed that, in the case of UI algorithm, even before the droplet could reach the liquid film, the film already got disrupted and instead of hitting the liquid film, the droplet got exposed to the dry bottom surface. We also noticed that, in case of UI formulation, the droplet while travelling towards the liquid film, got deformed and ultimately it took the shape of a cone before hitting the bottom wall. The major reason behind this is the amount of spurious currents generated as shown in Fig. 3.21. The figure shows the sectional view in $x-y$ plane at z=3D_o of the droplet when it is about to reach the liquid film. We can clearly notice that the amount of spurious currents generated in the case of UI algorithm are sufficient enough to displace the liquid film even before the droplet could actually reach there. But, in the case of BC algorithm, the droplet smoothly impinges on to the liquid film and a crown like shape is also formed, which moves out with time. Comparison of the radial distance at the bottom of the rim and height of the lamella using BC algorithm are shown in Fig. 3.22. Despite of the use of a relatively coarse mesh, we see that for the case of BC algorithm, the comparison of the geometrical quantities related to the droplet splashing (shown in the Fig. 3.22) are in well agreement with the published literature [2, 3, 4].

3.5 Closure

In this chapter, we present a balanced force strategy together with consistent treatment for simulating interfacial flows with large density contrast. In order to achieve proper force balancing, we modified the pressure definition by incorporating piezometric pressure and instead of using Green Gauss method, we opted for a variant

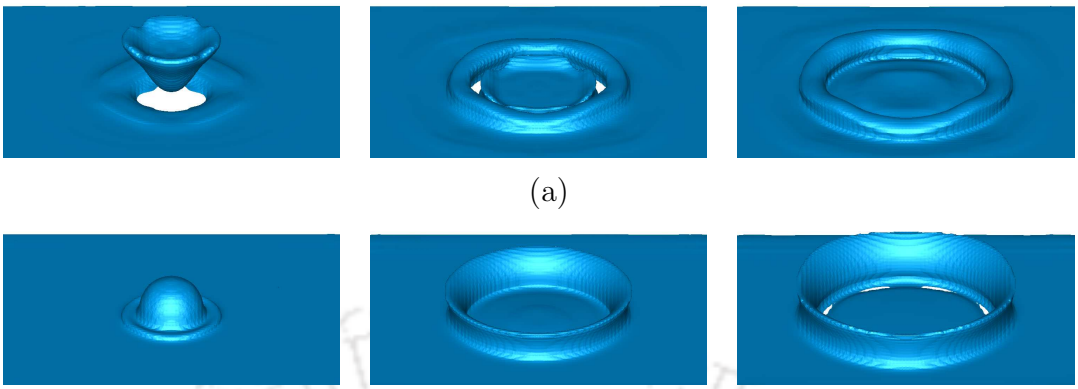

(a) (b)

Figure 3.20: Iso-surface of volume fraction $f = 0.5$ for droplet falling over thin liquid film at time $t = 0.3$, 1.7 and 2.7. Results are shown by employing (a) UI and (b) BC algorithms.

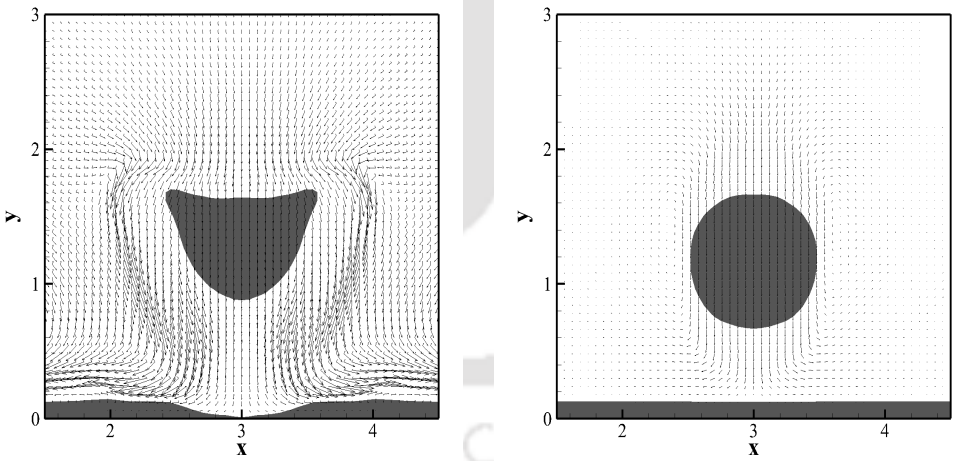

(a) (b)

Figure 3.21: Cut sectional view (mid $x - y$ plane) of droplet falling over thin liquid film at time $t = 1.75$. Results are shown by employing (a) UI (b) BC algorithms.

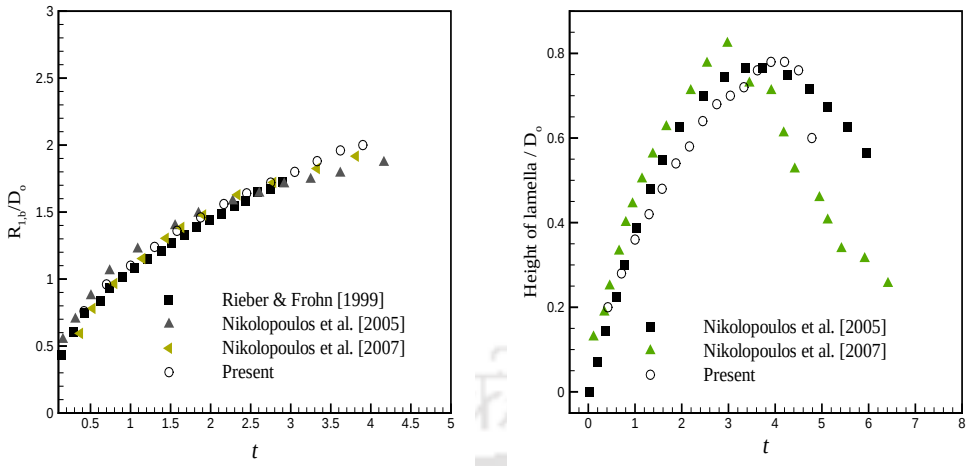

Figure 3.22: Comparison of the radial distance at the bottom of the rim and height of the lamella with the published results [2, 3, 4] using BC algorithm.

of the least squares method with a compact stencil for cell centroid gradient calculation. We also looked on to the effect of using similar and dissimilar convective schemes among different equations and termed them as consistent and inconsistent treatment, respectively. With the help of several test cases, both in two/three-dimensions, we compared the balanced and unbalanced force algorithm along with the effect of consistency. We found out that the balanced and consistent formulation essentially gives correct results for all cases irrespective of the density ratio, unlike either unbalanced or inconsistent formulations which might face significant difficulties. However, it is possible that depending upon the problem, the lack of balancing and/or consistency may or may not lead to unphysical solutions. Nevertheless, our studies provide strong evidence that favors the use of a well–balanced and consistent formulation for cost–effective, accurate and stable simulations of multiphase flows.

Chapter 4

An Alternative Balanced Force Algorithm For Multiphase Flows

In the previous chapter, we explained a balanced force strategy obtained by employing least squares approach together with an emphasis on the usage of similar discretization techniques applied to the convective terms appearing in momentum as well as advection equations. In the present chapter we discuss an alternative strategy to achieve force balancing. The present strategy is novel in the context of multiphase flows and is easy to implement as compared to the least squares approach.

4.1 Balanced Force Strategy

From the previous gradient reconstruction methodology (least squares), we can conclude that any imbalance between the normal derivative of any variable at face and its centroidal gradient which appears in momentum update can introduce significant amount of spurious currents. In the present strategy as well, we propose a gradient reconstruction technique in which the cell centroidal quantity is constructed from its respective value at each faces. This methodology is a variant of traditional Green Gauss method and hence we termed it modified Green Gauss approach. The methodology is now discussed in detail.

4.1.1 Source terms and their discretization

In addition to the source terms considered in the previous chapter, the following additional source terms are also tested using the present algorithm.

Gravity in volumetric form

In this form, the traditional way of handling the gravity force (volumetric body force) is adopted and mathematically it can be represented as,

$$\mathbf{S}_\phi = \rho \mathbf{g}$$

Thermo-capillary

Along with the gravity and surface tension terms, we consider the source terms due to marangoni stress as well. With the assumption that the surface tension coefficient is a linear function of temperature having gradient σ_t, we can write,

$$\sigma = \sigma_o + \sigma_t(T - T_0)$$

where σ_o is the surface tension defined at an appropriate reference temperature T_0 . The final form of the source term corresponding to thermo-capillary stress is

$$\mathbf{S}_\phi = \sigma\kappa\nabla f + \sigma_t(T - T_0)\kappa\nabla f + \sigma_t \nabla T|\nabla f| - \sigma_t \frac{\nabla T \cdot \nabla f}{|\nabla f|}\nabla f$$

It is to be noted that, due to the jump in density across the interface, there is a jump in the value of this force as well. This form of the gravitational forcing term does not hold any similarity with the pressure gradient term, as one appears to be in gradient form, while the other one has a volumetric appearance.

Each one of these terms are either present in gradient form or in the form of a volumetric body force. Here we explain a general way by which any of these source terms or any other source term can be discretized within a well-balanced framework. The methodology we describe here is not limited only to a particular form of the source term and hence there is no need to change the form of the source term to maintain proper force balancing. Considering the source terms with two different nature as,

$$\mathbf{S}_\phi = \boldsymbol{\eta} + \psi\nabla\chi \tag{4.1}$$

In order to calculate these source terms at cell centroid, we propose to use the following relation:

$$\mathbf{S}_\phi \mathrm{V_P} = \sum_f \{(\boldsymbol{\eta} \cdot \hat{\mathbf{n}})_f \ (\mathbf{x}_f - \mathbf{x}_\mathrm{P})|\mathbf{S}_f|\} + \sum_f \left\{ \psi_f \left(\frac{\partial \chi}{\partial n} \right)_f (\mathbf{x}_f - \mathbf{x}_\mathrm{P})|\mathbf{S}_f| \right\} \tag{4.2}$$

where subscripts "P"and "f"represents values at cell centroid and faces, respectively. This approach of calculating the centroidal quantities are taken from the work of Perot [63], wherein they utilize face normal velocities to calculate the cell centroidal velocity vector. We have utilized their concept, but instead of calculating cell centroid velocity vector, we have employed it for the calculation of cell centroid gradients as well as other relevant centroidal quantities. With the help of various test cases, the accuracy of this method in the context of multiphase flows is presented in Section 4.2.

This approach of calculating the centroidal quantities using their respective face values ensures necessary force balancing and is termed as Modified Green Gauss (MGG) method in the present work. The method is equally applicable to volumetric terms as well as the terms appearing in gradient form. Any source terms appearing in these two forms can be easily moulded in a balanced framework and hence there is no explicit requirement of converting one form of the source term into other. The benefit also lies in the fact that, as compared to least squares method [54], the present formulation does not need the solution of a matrix local to each cell for obtaining centroidal gradient quantities, and hence the method is cheaper and easy to implement. The traditional ways of calculating cell centroid values of these two source terms are volumetric interpolation and the traditional Green Gauss (GG) method. Using the traditional Green Gauss method, the cell centroid reconstruction of the above mentioned two different source terms can be expressed in the following way,

$$\mathbf{S}_\phi \mathrm{V_P} = \boldsymbol{\eta} \mathrm{V_P} + \psi_\mathrm{P} \sum_f \{\chi_f \mathbf{S}_f\} \tag{4.3}$$

4.1.2 Pressure velocity coupling

Similar to the momentum interpolation technique used in the previous algorithm, here we again explain the procedure using the above mentioned generalized source terms. Initially provisional momentum is obtained at each cell centroid by solving the following set of linear equations iteratively,

$$V_{\mathrm{P}}\frac{(\rho\mathbf{u})^{*}_{\mathrm{P}}-(\rho\mathbf{u})^{n}_{\mathrm{P}}}{\Delta t}+\sum_{f}F^{n}_{f}(\rho\mathbf{u})^{*}_{f}-\sum_{f}F^{*}_{d\mathbf{u}f}=0 \tag{4.4}$$

It is to be noted that, similar to the previous algorithm, we drop all the source terms including pressure gradient from the momentum equations to get the provisional fluxes. Using the two generalized source terms, pressure Poisson equation (PPE) can be written as,

$$\nabla\cdot\left(\frac{\nabla p}{\rho}\right)=\frac{\nabla\cdot\mathbf{u}^{*}}{\Delta t}+\nabla\cdot\left(\frac{\boldsymbol{\eta}}{\rho}\right)+\nabla\cdot\left(\frac{\psi\nabla\chi}{\rho}\right) \tag{4.5}$$

In discrete form, it can be written as,

$$\Delta t\sum_{f}\left(\frac{\nabla p^{*}}{\rho}\right)_{f}\cdot\mathbf{S}_{f}=\sum_{f}F^{*}_{0f}+\Delta t\sum_{f}\left(\frac{\boldsymbol{\eta}}{\rho}\right)_{f}\cdot\mathbf{S}_{f}+\Delta t\sum_{f}\left(\frac{\psi\nabla\chi}{\rho}\right)_{f}\cdot\mathbf{S}_{f} \tag{4.6}$$

where

$$F^{*}_{0f}=\mathbf{u}^{*}_{f}\cdot\mathbf{S}_{f} \tag{4.7}$$

Once the pressure field is obtained, fluxes at each face is then corrected by following,

$$F^{n+1}_{f}=F^{*}_{0f}-\Delta t\left(\frac{\nabla p^{*}}{\rho}\right)_{f}\cdot\mathbf{S}_{f}+\Delta t\left(\frac{\boldsymbol{\eta}}{\rho}\right)_{f}\cdot\mathbf{S}_{f}+\Delta t\left(\frac{\psi\nabla\chi}{\rho}\right)_{f}\cdot\mathbf{S}_{f} \tag{4.8}$$

Finally, we update the cell centroid velocities in the following way

$$\mathbf{u}^{n+1}_{\mathrm{P}}=\mathbf{u}^{*}_{\mathrm{P}}+\Delta t\left(-\frac{\nabla p}{\rho}+\frac{\boldsymbol{\eta}}{\rho}+\frac{\psi\nabla\chi}{\rho}\right)_{\mathrm{P}} \tag{4.9}$$

In order to get the cell centroidal momentum, the obtained velocities are multiplied by density of the respective cells. The stepwise solution procedure followed in this work is summarized below.

Solution algorithm:

1) Initialize all the variables appropriately.
2) Assume $F_f^n = F_f^{n-1}$
3) Obtain provisional momentum by solving Eq. 4.4 iteratively.
4) After calculating provisional fluxes from the newly obtained mass momentum, iterate Eq. 4.5 for getting pressure field.
5) Correct the fluxes at each face and use Eq. 4.9 to get the cell centroidal velocities.
6) Solve Eq. 2.4 iteratively to advect the volume fraction and then calculate the fluid properties.
7) Repeat the same procedure starting from step 3 until stopping criterion is met.

4.2 Results and Discussion

We now present various test cases associated with different source terms using GG and MGG formulations. These formulations are implemented and tested in an in-house code which is inherently a three-dimensional solver over unstructured meshes.

4.2.1 Static droplet

The first problem we consider is the case of a static droplet which is also studied by [53, 54, 59]. In order to evaluate the ability of GG (Green Gauss)and MGG (Modified Green Gauss) reconstruction algorithms on the generation of spurious currents, the present test case is being performed. The test problem consists of a droplet of diameter D placed in an initially quiescent medium where the viscous effects are completely ignored. In the absence of gravity, we carry out studies specifying both the exact curvature at the interface as well as calculated curvature. The computational domain chosen for the study is $8 \times 8 \times 8$ cubical box with a droplet of size $D = 4$ placed at its center. Specifying the value of surface tension coefficient to be 73 and taking a constant time step of 0.001, the maximum magnitude of the velocity vector $|\mathbf{u}|_{max}$ after time $t{=}\Delta t$ and 50 Δt in the entire domain is shown in Table 4.1.

Interestingly, both the methods yield machine precise values of spurious currents, when exact value of curvature is specified. On the contrary, when the curvature is

grid	ρ_1/ρ_2	method	$\|\mathbf{u}\|_{max}(\Delta t)$	$\|\mathbf{u}\|_{max}(50\Delta t)$
uniform 40^3 meshes	10^1	GG	4.84×10^{-16}	4.78×10^{-15}
		MGG	1.71×10^{-16}	6.30×10^{-16}
	10^3	GG	5.18×10^{-16}	5.67×10^{-15}
		MGG	4.51×10^{-15}	8.96×10^{-15}
clustered 40^3 meshes	10^1	GG	7.45×10^{-16}	5.22×10^{-15}
		MGG	4.83×10^{-16}	8.64×10^{-16}
	10^3	GG	5.93×10^{-16}	4.95×10^{-15}
		MGG	3.66×10^{-15}	7.76×10^{-15}
tetrahedral $\approx$77000 meshes	10^1	GG	1.83×10^{-15}	7.67×10^{-15}
		MGG	1.60×10^{-15}	2.47×10^{-15}
	10^3	GG	1.31×10^{-15}	7.34×10^{-15}
		MGG	1.00×10^{-15}	3.98×10^{-15}

Table 4.1: Maximum magnitude of spurious currents at t=Δt and t=$50\Delta t$ for two different density ratio and by employing different grids. Interface curvature is specified exactly.

calculated numerically, GG outperforms, as it can be seen from Table 4.2. This is obvious, as for the case when exact curvature is specified, the values of curvature at the cell and its faces are same. But for the case when curvature is calculated numerically, the values of curvature differ. MGG method reconstructs back the cell centroid quantities using their respective value at faces, and hence, it is in accordance with the discretization procedure adopted for pressure Poisson equation. This makes the MGG method superior than the GG reconstruction algorithm for handling surface tension dominant problems. Also, in Fig. 4.1 we present the pictorial representation of the spurious currents generated inside the domain employing both the formulations.

Method	$t = \Delta t$	$t = 50\Delta t$
GG	0.045	1.471
MGG	0.0061	0.3383
Williams et al.[6]	0.0855	0.386

Table 4.2: Maximum magnitude of spurious currents using calculated curvature at t=Δt and t=$50\Delta t$ for two different formulations and by employing clustered 40^3 meshes. Along with the results of the present study, the published solutions of Williams et al.[6] has also been shown, where they employed finite differenced normals along with a parabolic delta functions.

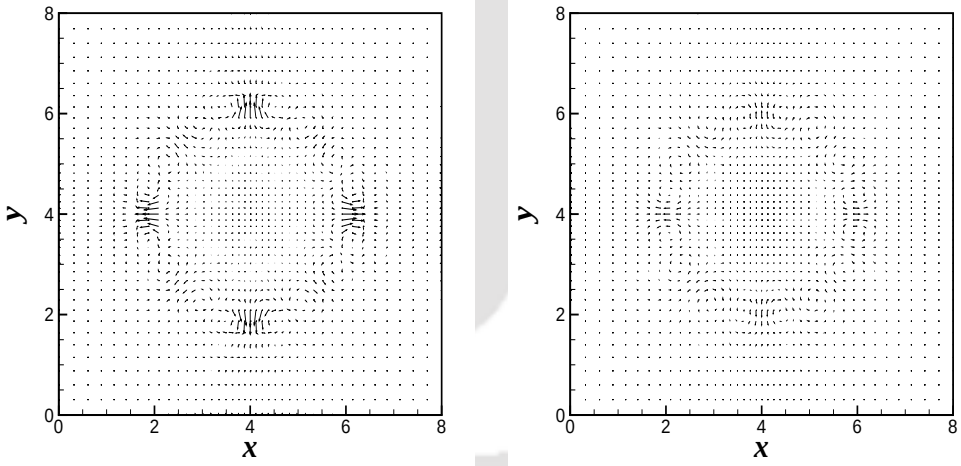

(a) (b)

Figure 4.1: Pictorial representation of the spurious currents generated inside the domain at time $t = 50\ \Delta t$ for static inviscid drop along the mid plane of the computational geometry by employing (a) GG and (b) MGG formulations. Clustered mesh with size 40×40×40 is used and the curvature is calculated numerically.

4.2.2 Static tank

While the previous test case considered the effect of surface tension forces, we now study the problem of handling of body forces, in particular, the gravitational force in a partially filled static tank. While the problem appears to be extremely trivial, having a known exact solution, it forms an important test case to test the ability of different numerical approaches to maintain the steady static solutions at all times. It has been proven earlier [61] that, maintaining a zero velocity at all times over the grid with collocated arrangements of variables is a challenging task unless a special care is taken to do so. The problem definition includes a two-dimensional tank partially filled with heavy liquid. The domain chosen for the study is a square cavity of size 1×1 and is half filled with the heavy liquid during the initial stage. All the boundaries are specified as walls except for the top boundary, which is treated as open to atmosphere. In the present work, we handle the gravity force in the following two different ways.

Piezometric approach

In piezometric approach, gravitational forcing term contains the gradient of density. The benefit of using a piezometric approach is that the two competing terms viz. pressure gradient and the gravity can be treated in a similar way at discrete level. Using this approach in the present problem, the exact value of the jump in pressure across the interface (considering bottom wall as the datum) can be calculated as,

$$\Delta p_{max} = 0.5 \ |\mathbf{g}| \ (\rho_1 - \rho_2)$$

Ideally, after single time step and even at higher times, the jump in pressure should be constant and exact with machine precise values of velocities generated in the entire domain. For the quantitative evaluation of GG and MGG formulations, we measure the maximum magnitude of velocities generated in the entire domain along with a relative error in pressure jump across the interface. The following expression is utilized for calculating the error in pressure jump.

$$E(\Delta p)_{max} = \frac{|\Delta p_{max} - \Delta p_{exact}|}{\Delta p_{exact}}$$

where p_{max} is defined as,

$$\Delta p_{max} = p_{max} - p_{min}$$

here, p_{max} and p_{min} are the maximum and minimum values of pressure in the entire domain. A constant time step of $\Delta t = 0.001$ is chosen for the study and we present the performance of GG and MGG formulations for two different density ratios over uniform, clustered and triangular meshes at time $t = \Delta t$ and $t = 50\Delta t$ in Table 4.3. The MGG formulation is able to maintain machine accurate values of velocities in the entire domain along with an exact value of pressure jump even at higher time $t = 50\Delta t$. But in case of GG formulation, for both the density ratios, a considerable amount of spurious currents are generated near to the interface along with an error of the order of $\approx 10^{-3}$ in pressure. This is mainly because of the selection of density and y coordinate value during velocity update. In MGG formulation, face value of coordinate y and density are taken for reconstructing the cell centroidal gradient quantities, while for GG formulation it is the cell centroidal value. Figure 4.2 shows the vector plot of the spurious currents generated in the domain at $t = 50\Delta t$ employing GG and MGG formulations.

Volumetric approach

In this approach, the form of the gravitational forcing term does not hold any similarity with the pressure gradient term, as one appears to be in gradient form, while the other one has a volumetric appearance. For achieving a perfect balancing between these two associated terms, it is necessary to take extreme care while reconstructing back the centroidal pressure gradient, which will be later used during momentum update. Ideally, at initial time and even during later stages of the computations, the developed pressure field should exactly balance the gravitational force, leading to machine accurate values of velocities in the entire domain. Table 4.4 shows the maximum amount of spurious velocities generated inside the domain at time $t = \Delta t$ and $t = 50\Delta t$. As expected, MGG formulation results in achieving a complete balance between the gravitational force term and its associated presure gradient, while GG formulation leads to the generation of a considerable amount of spurious currents, showing its unbalanced nature.

4.2.3 Thermo-capillary drop

The performance evaluation of the two methods for handling strong interfacial forces like marangoni stress is now examined. The problem under consideration is the

Grid	Method	ρ_1/ρ_2	$\|\mathbf{u}\|_{max}$		$E(\Delta p_{max})$	
			t=Δt	t=50Δt	t=Δt	t=50Δt
50×50 uniform	GG	10^1	2.21×10^{-02}	3.11×10^{-01}	2.00×10^{-15}	1.68×10^{-02}
		10^3	2.45	34.8	5.10×10^{-17}	1.68×10^{-02}
	MGG	10^1	1.55×10^{-14}	1.30×10^{-14}	2.00×10^{-15}	2.26×10^{-15}
		10^3	1.47×10^{-15}	2.19×10^{-15}	5.10×10^{-17}	2.69×10^{-17}
50×50 clustered	GG	10^1	2.21×10^{-02}	2.95×10^{-01}	2.74×10^{-15}	1.04×10^{-02}
		10^3	2.45	32.75	6.33×10^{-18}	1.04×10^{-02}
	MGG	10^1	4.11×10^{-15}	4.82×10^{-15}	2.74×10^{-15}	2.35×10^{-15}
		10^3	1.37×10^{-15}	3.07×10^{-15}	6.33×10^{-18}	1.44×10^{-17}
100×100 uniform	GG	10^1	2.21×10^{-02}	3.11×10^{-01}	2.60×10^{-14}	8.45×10^{-03}
		10^3	2.45	34.48	4.18×10^{-16}	8.41×10^{-03}
	MGG	10^1	4.10×10^{-15}	6.69×10^{-15}	2.60×10^{-14}	7.93×10^{-14}
		10^3	7.78×10^{-15}	9.47×10^{-15}	4.18×10^{-16}	2.93×10^{-16}
100×100 clustered	GG	10^1	2.21×10^{-02}	3.03×10^{-01}	9.04×10^{-15}	5.04×10^{-03}
		10^3	2.45	33.61	3.10×10^{-16}	5.03×10^{-03}
	MGG	10^1	2.46×10^{-15}	5.64×10^{-15}	9.04×10^{-15}	8.69×10^{-15}
		10^3	1.39×10^{-14}	1.79×10^{-14}	3.10×10^{-16}	7.30×10^{-16}
≈8000 prism	GG	10^1	3.19×10^{-02}	7.51×10^{-01}	1.00×10^{-14}	8.27×10^{-03}
		10^3	3.54	71.55	7.36×10^{-16}	8.11×10^{-03}
	MGG	10^1	4.09×10^{-15}	5.74×10^{-15}	1.00×10^{-14}	1.71×10^{-14}
		10^3	1.35×10^{-14}	1.54×10^{-14}	7.36×10^{-16}	4.16×10^{-16}

Table 4.3: Magnitude of maximum spurious velocity and error in pressure jump for a partially filled two-dimensional static tank after Δt and $50\Delta t$ using GG and MGG formulations. The gravitational forcing term in piezometric formulation is employed for the study.

Grid	Method	ρ_1/ρ_2	$\|\mathbf{u}\|_{max}$	
			$t{=}\Delta t$	$t{=}50\Delta t$
50×50 uniform	GG	10^1	2.20×10^{-03}	3.14×10^{-03}
		10^3	2.45×10^{-01}	3.487
	MGG	10^1	1.14×10^{-16}	2.10×10^{-16}
		10^3	6.63×10^{-17}	1.69×10^{-16}
50×50 clustered	GG	10^1	2.20×10^{-03}	2.98×10^{-02}
		10^3	4.27×10^{-01}	3.310
	MGG	10^1	1.14×10^{-16}	2.10×10^{-16}
		10^3	4.70×10^{-17}	1.76×10^{-16}
100×100 uniform	GG	10^1	2.21×10^{-03}	3.14×10^{-02}
		10^3	2.45×10^{-01}	3.487
	MGG	10^1	2.97×10^{-16}	5.54×10^{-16}
		10^3	1.58×10^{-16}	3.04×10^{-16}
100×100 clustered	GG	10^1	2.21×10^{-03}	3.06×10^{-02}
		10^3	2.45×10^{-01}	3.398
	MGG	10^1	1.17×10^{-16}	3.29×10^{-16}
		10^3	1.61×10^{-16}	4.08×10^{-16}
≈8000 prism	GG	10^1	3.54×10^{-03}	9.74×10^{-02}
		10^3	3.79×10^{-01}	7.348
	MGG	10^1	3.53×10^{-16}	4.69×10^{-15}
		10^3	1.94×10^{-16}	3.45×10^{-15}

Table 4.4: Magnitude of maximum spurious velocity for a partially filled two-dimensional static tank after Δt and $50\Delta t$ using GG and MGG formulations. The gravitational forcing term is treated volumetrically.

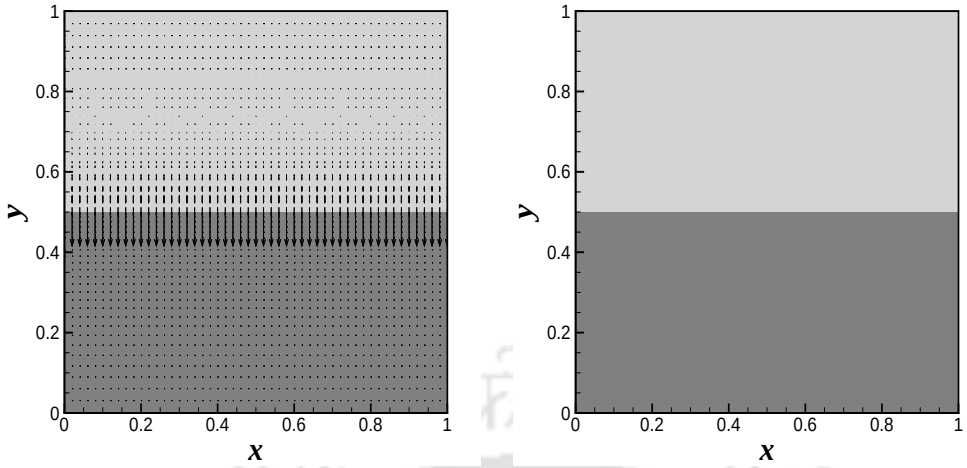

Figure 4.2: Pictorial representation of the spurious currents generated inside the domain at time $t = 50\ \Delta t$ for the case of static tank partially filled with heavy liquid by employing (a) GG and (b) MGG formulations. The density ratio is 1000.

rise of a spherical droplet having diameter $D = 1$ and is subjected to a constant temperature gradient field of $0.1\overline{3}$. Considering the surface tension to be linearly dependent on temperature, we assume the surface tension coefficient as,

$$\sigma = 0.1 - 0.1T$$

If the densities and viscosities of both the fluids are assumed to be constant and are equal to 0.2 and 0.1, respectively, then according to Young et al. [121], the analytical rise velocity of the droplet at steady state is $\overline{v} = 8.\overline{8} \times 10^{-3}$. Since the theoretical velocity is based on the assumption that the droplet does not deform with time, hence, in the present calculations, the volume fractions are not allowed to evolve with time. The normalized rise velocity of the droplet for this particular case can be numerically calculated as,

$$\upsilon_{normalized} = \frac{\int vf\ dV}{8.888 \times 10^{-3} \int f\ dV}$$

Employing different formulations, the steady state value of the normalized velocity is shown in Table 4.5 for various clustered grids. The time step restriction as

grid	method	$v_{normalized}$
50×50×50	MGG	0.925
	GG	0.70
80×80×80	MGG	0.945
	GG	0.775
110×110×110	MGG	0.96
	GG	0.79

Table 4.5: Comparison of the normalized rise velocity of a drop due to the thermo-capillary effect using different formulations and by employing different clustered grids.

proposed in [122] is followed. With the use of the MGG method, the steady state normalized velocity is found to be 0.96 on 110 × 110 × 110 clustered grid, which is comparable with the earlier studies [61, 122]. But the use of GG formulation does not lead to the balanced framework and is reflected in the fact that it leads to much lower values of rise velocity even on the finer meshes. We see that the results improve with mesh refinement, but the normalized rise velocity obtained on the finest grid with GG formulation is way lower than that of the value obtained by MGG formulation on the coarsest grid. On sufficiently fine grids, MGG formulation gives the value close to the theoretical results, whereas the GG approach has an error of 21%.

4.2.4 Two-dimensional bubble rise

The present two-dimensional benchmark problem serves as a test case for evaluating the performance of MGG method under the circumstances where both surface tension and gravitational forces are equally important. The test case involves the simulation of the rise of a two-dimensional bubble in an initially stagnant fluid. As per [1], various parameters involved in determining the bubble shape, its rise velocity and mass center includes ρ_1=1000, ρ_2=100, μ_1=10, μ_2=1, $|\mathbf{g}|$=0.98 and σ=24.5. Subscripts 1 and 2 denote heavier and lighter fluids, respectively. Simulations are performed inside a 1 × 2 rectangular domain with symmetry boundary conditions

grid	v_{max}	$t(v_{max})$	$y_c(t=3)$
50×100 [a]	0.2381	0.934	1.054
100×200 [a]	0.2391	0.9335	1.064
40×160 [b]	0.2429	0.941	1.056
≈ 20000 [c]	0.2368	0.913	1.050
≈ 45000 [c]	0.2384	0.925	1.0626
Published solutions			
Hysing et al. [1]	0.2419	0.927	1.081
Klostermann et al. [5]	0.2348	0.9516	1.0696
Strubelj et al. [123]	0.2457	0.9235	1.0679

Table 4.6: Comparison of various benchmark quantities of the two-dimensional bubble rise problem with the available published results. Superscripts a, b and c represent uniform orthogonal, non-uniform orthogonal and prism cells, respectively, used for the discretization of computational domain.

applied on the side walls whereas top and bottom walls are specified as no slip walls. Using different mesh resolutions, comparisons of the present results with the benchmark solutions are shown in Table 4.6. Also, the temporal variation of the rise velocity of the bubble and its mass center is shown in Fig. 4.3. Along with these comparisons, the shape of the bubble at time $t = 3.0$ is also compared in Fig. 4.4 with the result of Hysing et al. [1]. A reasonably good match of the present work with the published articles illustrates the efficacy of the proposed method to handle the situations where both surface tension and gravitational forces are significant. The mass conservation error is also calculated for this case by employing BC algorithm and its value is less than 0.03 %.

4.2.5 Three-dimensional droplet splashing

Finally, the proposed MGG formulation is tested for a three-dimensional problem involving the falling of a droplet over thin liquid film. This particular case is selected because of its dominant surface tension and gravitational forces. The dynamics of

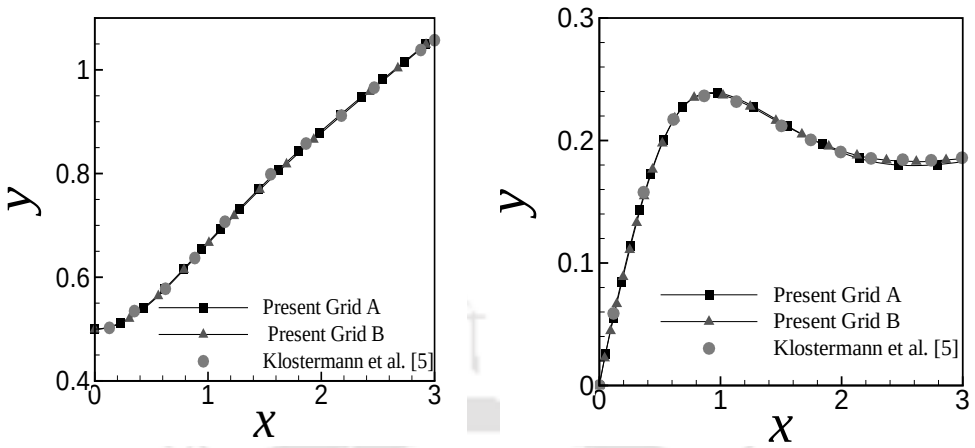

Figure 4.3: Temporal evolution of (a) center of mass and (b) rising velocity for two-dimensional bubble rise problem. Grid A represents 100 × 200 uniform orthogonal meshes, while Grid B represents ≈ 45000 prism cells used for the discretization of computational domain.

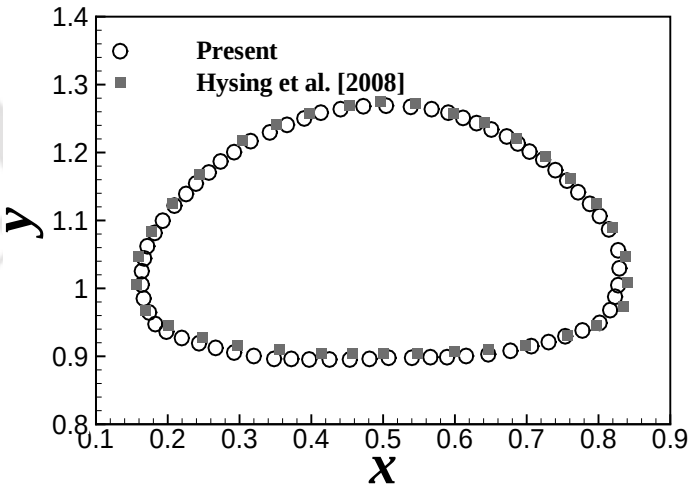

Figure 4.4: Comparison of the bubble shape at time $t = 3.0$ with the benchmark solution of Hysing et al. [1].

the splashing droplet is governed by various non-dimensional parameters viz. Weber number (We), Reynolds number (Re), Froude Number (Fr) and non-dimensional film thickness (H) which are chosen according to [4].

The problem defines a droplet having diameter $D = 1$ with an initial height of $2.8D$ above the liquid film and is allowed to fall with an initial velocity of U_0. The computational domain under consideration is a $6D \times 6D \times 6D$ cubical box with 512000 non-uniform hexahedral discrete elements. A constant time step of $\Delta t = 0.001$ is used for the simulations and the boundaries are specified as walls except for the top boundary, which is treated as open to atmosphere. Various non-dimensional parameters associated with this test case are We=250, Re=11294, Fr=363 and H=0.116. The formation of crown ring and its propagation are well captured by the present simulation and in Fig. 4.5 we show the quantitative comparision of the temporal evolution of radial distance at the bottom of the rim ($R_{l,b}/D$) with the available experimental and numerical findings. Comparisons are found to be in good agreement. Also, pictorial representation of the splashing process is shown in Fig. 4.6. However, the formation of secondary droplets could not be captured by the present simulation, but we believe that it can be captured by employing much finer grids or by adaptive meshing.

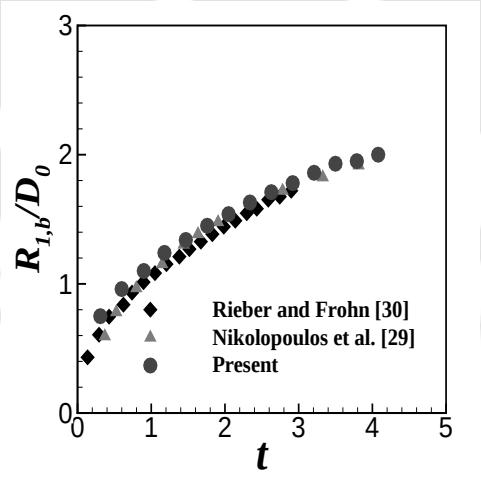

Figure 4.5: Temporal evolution of radial distance at the bottom of the rim along with the published results [2, 4] using MGG method.

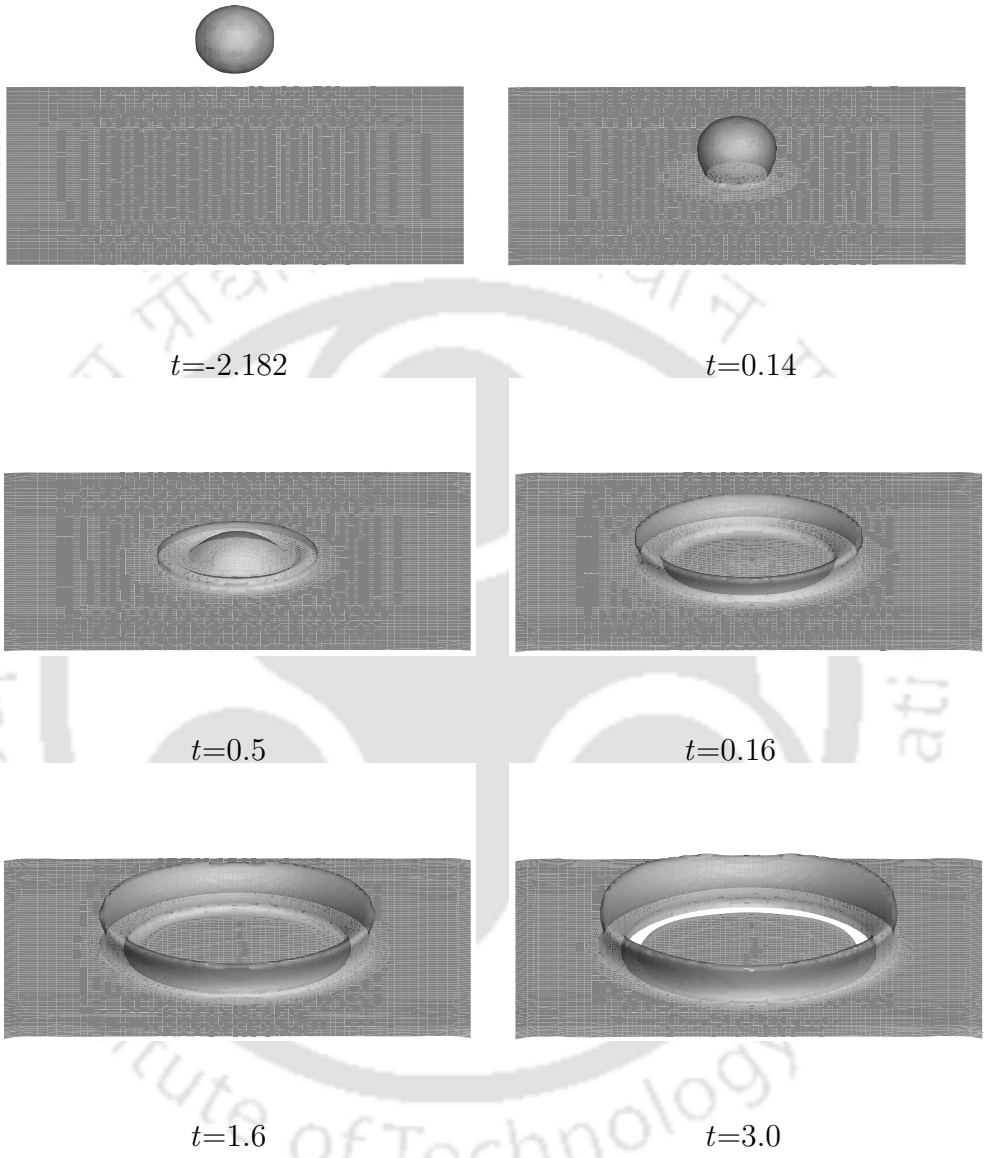

Figure 4.6: Pictorial representation of droplet falling over thin liquid film at various time instances. Results are shown by employing MGG formulation.

4.3 Closure

We have explained in this chapter that how a computationally cheaper method can be employed to achieve necessary force balancing. The benefit of the method lies in the fact that it can handle various types of forces and it does not pose any restriction on the type of source term. With the help of various test cases both in two and three-dimensions, we have presented the capabilities of this alternative method in the context of multiphase flows.

Chapter 5

A Parametric Study On The Droplet Detachment Process From The Ceiling Under The Effect of Gravity

5.1 Introduction

In this chapter, using the final developed solver, we present a parametric study on the detachment of a droplet placed over a horizontal solid substrate. The present study can be considered as an extension to the work of Tilehboni et al. [92]. They simulated the droplet behavior for a very low value of density and viscosity ratios. Also, in their study, the sole effect of contact angle has not been shown separately. Keeping these motivations in mind, herein, in this chapter, we discuss about the sole effect of various parameters including density ratio, contact angle and the effect of Weber number on the droplet dripping and detachment process. Apart from this, a separate study has been devoted to consider the effect of the presence of an adjacent droplet as well.

5.2 Problem Specification And Validation

In the following two subsections, the details of the problem set up and a validation test case has been presented.

5.2.1 Problem specification

In the present problem, as depicted in Fig. 5.1, two different computational domains with different initial conditions are used. The smaller domain is for studying the detachment of single droplet while the bigger domain is for two droplets, so that the effect of multiple droplets can be considered. The smaller domain is of size $4w \times 4w$, while the bigger domain is of $6w \times 4w$ in $x-$ and $y-$directions, respectively. We considered w=1 for all the simulations. Initially, the droplets are introduced on the top surface with gravity acting downwards. Computational domain is discretized into 400 $\times$ 400 and 600 $\times$ 400 non-uniform hexahedral cells for smaller and bigger domains, respectively. The top wall is specified with a static contact angle θ, while the other three boundaries are treated as open to atmosphere. Despite of the usage of a high resolution scheme for the advection of volume fractions, the interface separating the two fluids gets smeared to a few cell widths, and therefore, the volume fraction contour corresponding to $f = 0.5$ is considered as the fluid-fluid interface. We discuss the results in Section 5 with the aid of temporal evolution of droplet centroid y_c, its downward velocity v, elongated length before detachment l and the wetted length w as shown in Fig. 5.1 (a). It is to be noted that, for the calculation of droplet velocity, the following relation has been used.

$$\overline{v} = \frac{\int v f \; dA}{\int f \; dA}$$

As the problem includes contact line dynamics of the moving interface, a slip model needs to be incorporated to avoid force singularity. Similar to the work of Renardy et al. [124], Navier slip condition is usually adopted, wherein, the contact line velocity U_{cl} is expressed as a function of the derivative of the tangential velocity in the direction normal to the wall,

$$U_{\text{cl}} = \beta \frac{\partial u}{\partial n}$$

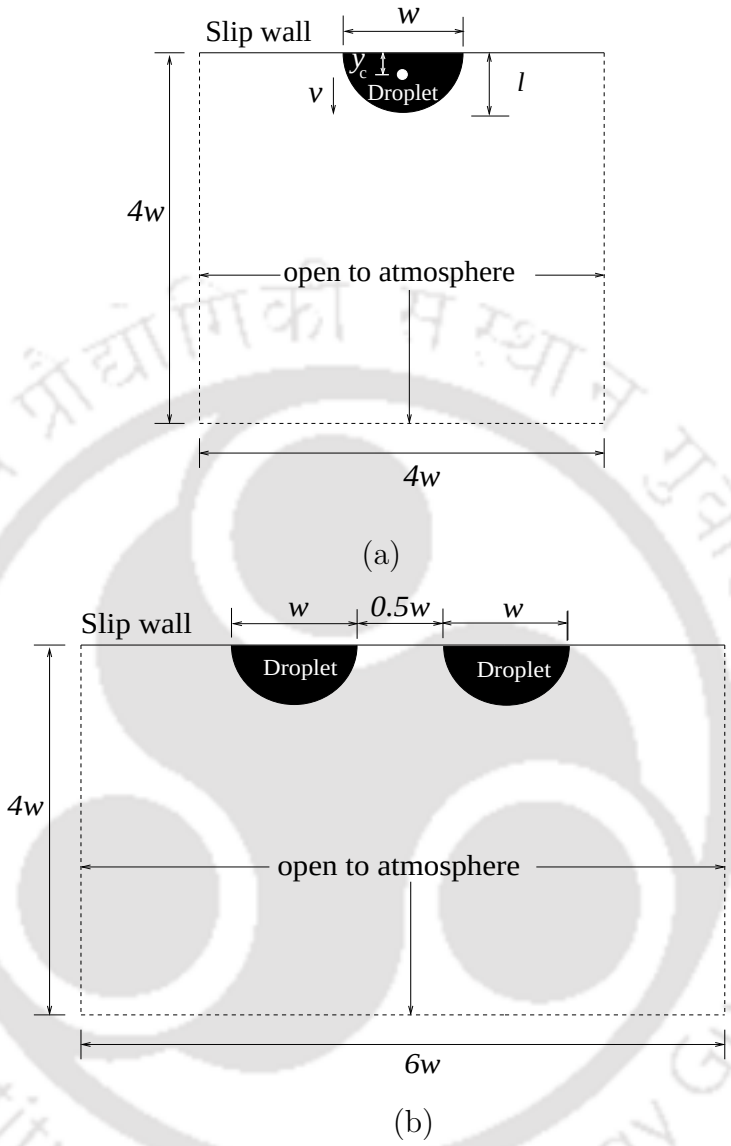

Figure 5.1: Computational domain with initial and boundary conditions for single and multiple droplet arrangements. Various geometrical properties for quantitative evaluation of the droplet detachment process are also shown in single droplet arrangement case.

where, β is the slip length. However, in the present study, a different approach has been incorporated. Following the work of Salih and Moulick [125], the normal derivative of velocity with slip can be written as,

$$\left.\frac{\partial u}{\partial n}\right|_{slip} = (1-\chi)\left.\frac{\partial u}{\partial n}\right|_{noslip} \tag{5.1}$$

where χ is the slip coefficient and it ranges in between 0-1. For getting the no slip condition, its value is 0, whereas for a free slip condition, its value is 1.

5.2.2 Validation

In order to validate the time dependent solutions of the droplet motion, this test case has been performed. The problem has been taken from the work of Renardy et al. [124], wherein the temporal evolution of a droplet placed over a solid surface is being monitored. Computations are performed in a square domain of size 1×1, wherein, a droplet of diameter D=0.2 initially centered at $(x, y) = (0.5, 0.85)$ is placed on the top wall. The densities and dynamic viscosities of both the fluids are identical and are equal to 0.01 and 0.001, respectively. Surface tension coefficient and the wall contact angle are specified as 0.03 and $\theta = 70.53°$, respectively. Our simulation resuts and the outcome of OpenFOAM [126] has been reported in Table 5.1. Also, the comparison of the snapshots of the droplet shape at different time instances are shown in Fig. 5.2. Results are found to be in good agreement with the solutions obtained from OpenFOAM [126].

t	OpenFOAM [126]	Present
0	0.633	0.633
0.05	0.697	0.703
0.1	0.735	0.744
0.15	0.769	0.778
0.2	0.797	0.806
0.25	0.815	0.820

Table 5.1: Position of contact line.

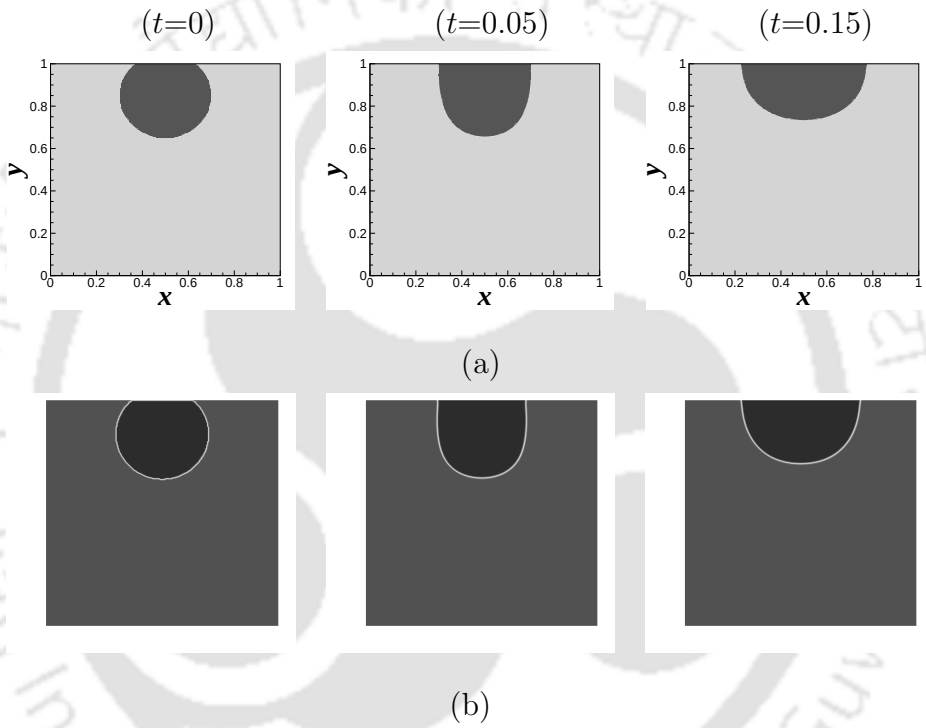

Figure 5.2: Droplet shape at different time instances using (a) present solver and the (b) OpenFOAM results.

5.3 Non-dimensionalization

The non-dimensionalization has been performed by utilizing the following dimensionless characteristic variables,

$$x^* = \frac{x}{D_0}; \quad \mathbf{u}^* = \frac{\mathbf{u}}{\sqrt{|\mathbf{g}|\ D_0}}; \quad t^* = \frac{t}{D_0/\sqrt{|\mathbf{g}|\ D_0}}; \quad \rho^* = \frac{\rho}{\rho_1}; \quad \mu^* = \frac{\mu}{\mu_1};$$

$$p^* = \frac{p}{\rho_1\ |\mathbf{g}|D_0}; \quad \kappa^* = \frac{\kappa}{D_0^{-1}}$$

where x^*, $\mathbf{u}^*$ and t^* are the non-dimensional length, velocity and time, respectively. D_0 is the initial diameter of the droplet and the fluid properties has been non-dimensionalized by the properties of heavier liquid. The resulting non-dimensional momentum equation takes the form as,

$$\frac{\partial\left(\rho^*\mathbf{u}^*\right)}{\partial t^*} + \nabla\cdot\left(\rho^*\mathbf{u}^*\mathbf{u}^*\right) = -\nabla p^* + \frac{1}{Re}\nabla\cdot\left[\mu^*\left(\nabla\mathbf{u}^* + \nabla(\mathbf{u}^*)^T\right)\right] + \hat{\mathbf{g}}\cdot\mathbf{x}^*\nabla\rho^* + \frac{1}{We}\kappa^*\nabla f \tag{5.2}$$

where, Re and We are the Reynolds number and the Weber number, respectively.

$$Re = \frac{\rho_1 D_0\sqrt{|\mathbf{g}|\ D_0}}{\mu_1} \qquad We = \frac{\rho_1 D_0^2|\mathbf{g}|}{\sigma}$$

The non-dimensional density and viscosity can be expressed as a function of density ratio (λ) and viscosity ratio (μ_r) in the following manner,

$$\rho = f + \frac{1}{\lambda}(1-f) \tag{5.3}$$

$$\mu = f + \frac{1}{\mu_r}(1-f) \tag{5.4}$$

5.4 Results and Discussion

Three forces gravity, surface tension and surface adherence, act simultaneously over the droplet and dictate the droplet dynamics along with the viscous effects. In order to consider the varying proportions of these forces, in the following sub-sections, we investigate the effect of density ratio (λ), Weber number, surface wettabilities (effect of contact angle θ) and the presence of adjacent droplet on the droplet detachment process.

The temporal evolution of various geometrical properties, as shown in Fig. 5.1 (a) related to droplet dynamics are monitored. We remark here that for all the cases where detachment occurs, the geometrical properties are calculated only upto that time interval where breakup occurs. It is also to be noted that for all the simulations, the values of Reynolds number, Weber number and wall static contact angle are fixed and are equal to $Re = 500$, $We = 15$ and $\theta = 90°$, unless otherwise stated.

5.4.1 Effect of density ratio

The effect of density ratio on the droplet detachment has been considered by taking three different values of λ viz 1.5, 10 and 1000. In this study, the aim is to analyse the effect of bulk fluid density on the behavior of the droplet. The temporal evolution of the droplet for $\lambda = 10$ is shown in Fig. 5.3. As the surface is neutral ($\theta = 90°$), it can be noticed from the snapshots that the droplet does not tries to stick to the wall and also do not leave on its own. Initially due to the weight of the droplet it travels downward and changes its shape from spherical to a pear like object. These pear shaped droplet has also been reported experimentally and numerically [81, 127, 91] for the cases of both droplet dripping from the nozzle as well as wall bounded pendant droplets. With the advancement of time, it necks in the region near to the wall and ultimately detaches off the wall completely. Similar behavior has been observed even for the case of $\lambda = 1000$. But the elongation of the droplet before detachment is more in case of higher density ratio. It is to be noted that for these cases, as the surface is neutral, the droplet completely detaches off the wall. But for the hydrophobic surfaces, the droplet may not completely detach and the formation of liquid bridge may be noticed. This has been studied later in this section.

Figures 5.4 (a)-(c) show the droplet shape at $t = 2.0$ for all the three density ratios. Temporal evolution of various parameters including centroid y_c, downward velocity v and width w is plotted in Figs. 5.5 (a)-(c). It has been seen earlier that for the value of $\lambda = 10$ and 1000, no residual amount of liquid was left on to the surface. But for very low density contrast i.e $\lambda = 1.5$, the weight of the droplet is not sufficient enough to overcome the effect of the wall adherence and hence no detachment occurs. For this case, initially the droplet tries to detach due to the

gravitational pull, but, the elongation of the droplet causes the surface tension force to dominate and eventually results in the backward motion of the droplet towards the wall. The process of elongation and retraction of the droplet continues until the viscous effects completely damps out the motion of the droplet and a steady state is achieved.

After studying the effect of density ratio on the the droplet detachment process, the question arises that whether can there be other parameters for $\lambda = 1.5$, which can cause the droplet to detach off the surface. In order to understand this, we now present a study on the effect of Weber number.

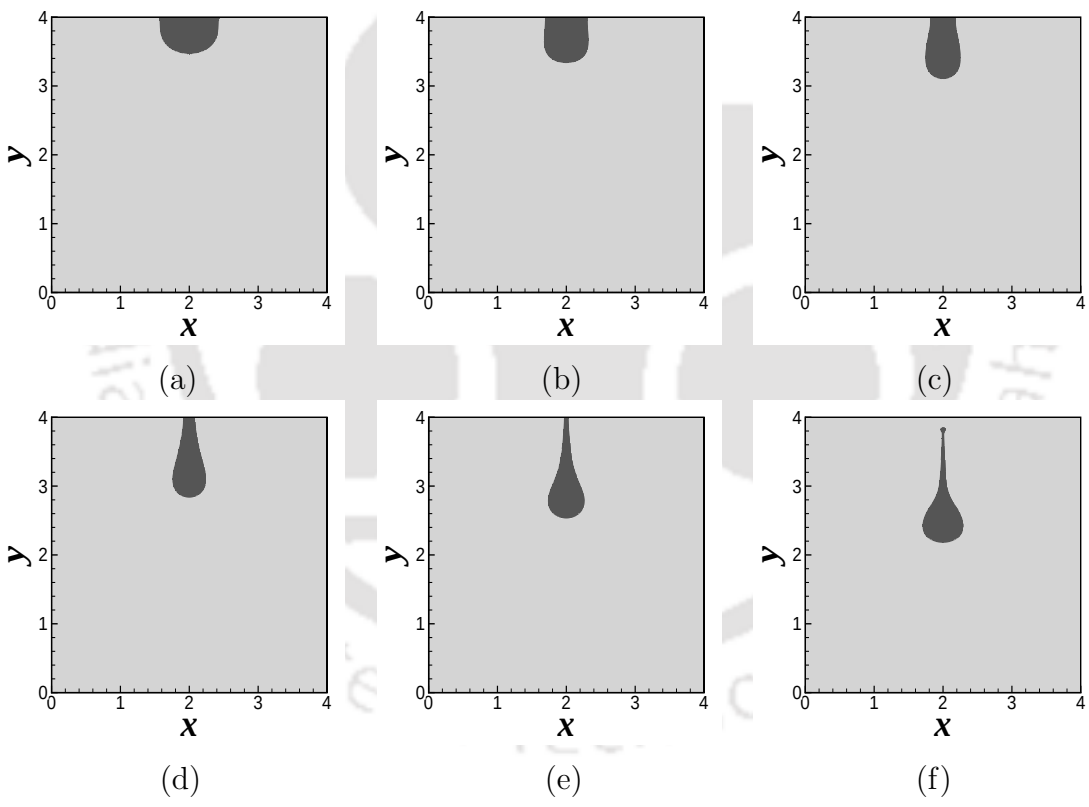

Figure 5.3: Evolution of the droplet for the case of $\lambda = 10$ and $\theta = 90°$. Snapshots are shown at time $t = 0.4$, 0.8, 1.2, 1.6, 2.0 and 2.4 .

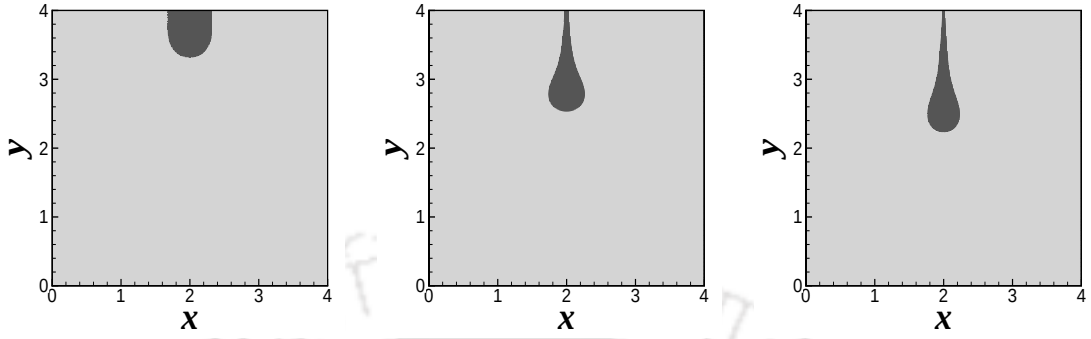

(a) (b) (c)

Figure 5.4: Snapshots of droplet shape at time $t = 2.0$ for (a) $\lambda = 1.5$, (b) $\lambda = 10$ and (c) $\lambda = 1000$.

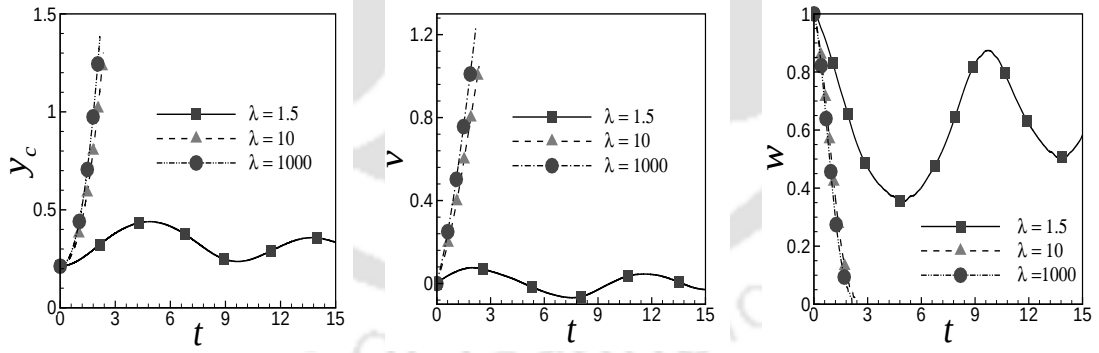

(a) (b) (c)

Figure 5.5: Temporal evolution of (a) droplet centroid y_c, (b) downward velocity v and (c) wetted length w for studying the effect of density ratio.

5.4.2 Effect of Weber number

We have shown earlier that a droplet of very low density ratio of 1.5 and $We = 15$, adheres to the wall. We now consider the effect of Weber number on the droplet behavior. For this case only, five different values of Weber number ($We = 10$, 20, 50, 100 and 150) are investigated for their effects on droplet motion. We remark that, for the case of We=10, which is lesser than 15 (considered in the previous study), the droplet behavior is similar to those shown in Fig. 5.5 (a)-(c). It is clear that a decrease in We would mean an increase in the surface tension effects and hence the droplet does not elongate further, and retracts back to the wall. However, for all the values of $We > 15$ considered in this study, the droplet leaves the wall. Tilehboni et al. [92] also reported that, at lower values of θ and We, the droplet do not leave the wall. However, in the present study, we do not reduce the contact angle, rather we keep it constant at $\theta = 90°$ only and observe the sole effect of We number.

Figure. 5.6 shows the temporal evolution of droplet for $We = 50$. Initially, similar to the lower Weber number case (We=15), droplet moves downward due to gravitational pull, but for the cases when Weber number is higher, the surface tension force is not just sufficient enough to retract the droplet back towards wall, and hence the droplet continues to move downward. As time progresses, formation of a thin liquid bridge is observed followed by the occurrence of droplet necking near to the region where it touches the solid surface (Fig. 5.6 (e)). Soon the primary breakup occurs and the liquid bridge gets completely separated out from the wall. Again, with the passage of time, this liquid bridge undergoes secondary breakup and the formation of multiple satellite droplets are observed. These secondary breakup and the formation of satellite droplets has also been reported in some of the earlier works [81, 82]. In the present study, formation of satellite droplets has been observed for the cases, when $We = 50$, 100 and 150 and is shown in Fig. 5.7. It is to be noted that the number of satellite droplets increases with the increase in the We. Figure 5.8 shows the temporal variation of various geometrical properties for $We = 20$, 50, 100 and 150.

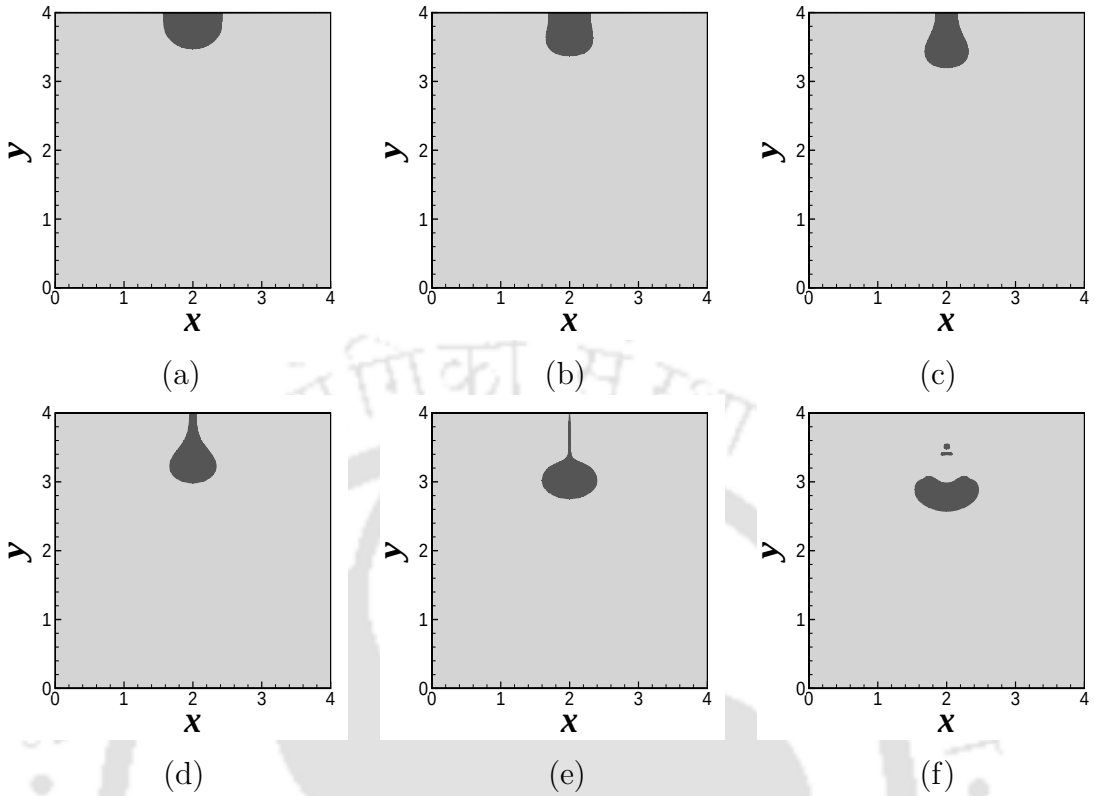

Figure 5.6: Evolution of droplet for the case of $\lambda = 1.5$ and $We = 50$. Snapshots are shown at time $t = 0.8$, 1.6, 2.4, 3.2, 4.0 and 4.6.

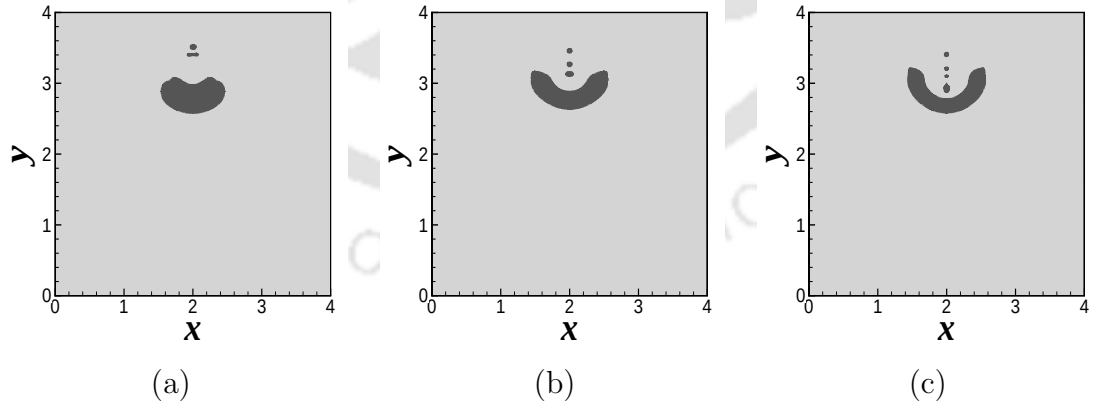

Figure 5.7: Snapshots showing the formation of satellite droplets for (a) $We = 50$, (b) $We = 100$ and (c) $We = 150$.

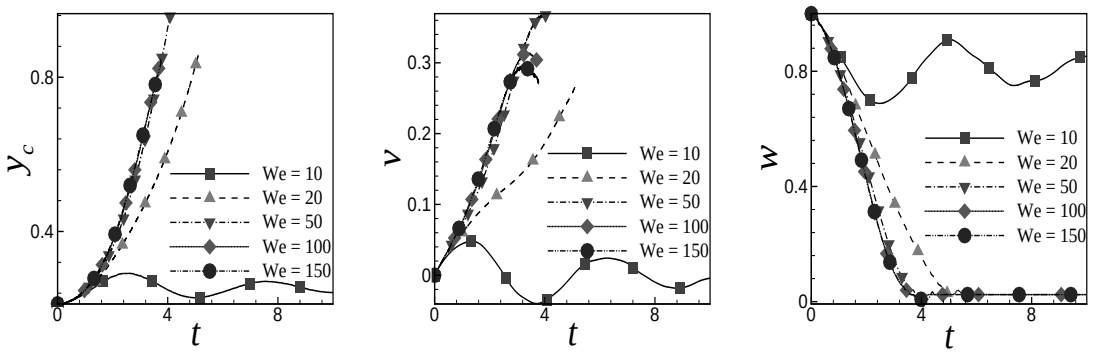

(a) (b) (c)

Figure 5.8: Temporal evolution of (a) droplet centroid y_c, (b) downward velocity v and (c) wetted length w for studying the effect of Weber number.

5.4.3 Effect of contact angle

Whenever a liquid droplet is in contact with a solid, the surface properties play a major role in dictating the dynamics. In order to study the effect of wall adherence, we considered four different values of wall contact angle, $\theta = 30°, 60°, 90°$ and $120°$. While $\theta < 90°$ indicate a hydrophilic surface, values of $\theta > 90°$ refers to a hydrophobic surface. The effect of these different contact angles has been studied in conjunction with two different density ratios i.e $\lambda = 1.5$ and 10. For $\lambda = 1.5$, the shape of the droplet at time $t = 2.5$ for four different contact angles has been shown in Figs. 5.9 (a)-(d). While for $\lambda = 10$, it is shown in Figs. 5.10 (a)-(d) at $t = 1.2$. Contour plots with $\lambda = 10$ (Fig. 5.10) show the faster movement of the droplet in the downward direction when compared against the case with $\lambda = 1.5$ (Fig. 5.9). For hydrophobic surface i.e for $\theta = 120°$, both the forces viz gravitational pull and wall adherence act in favor of the droplet removal, but for hydrophilic wall ($\theta = 30°, 60°$), wall adherence acts opposite to the gravitational pull. Hence, for the case when $\theta = 120°$, irrespective of the density ratio chosen, droplet gets detached form the wall. But in case of hydrophilic wall, i.e when the wall adherence tries to hold the droplet and gravity tries to pull it down, the density ratio plays a significant role in the detachment process. This can be seen from the Figs. 5.11 and 5.12, where the quantitative variations of the geometrical parameters for $\lambda = 1.5$ and 10 have been plotted. For the case, when $\lambda = 1.5$ and $\theta = 30°, 60°$ and $90°$, the droplet remains stick to the surface. But, for $\lambda = 10$, the dominant gravitational force pulls out the droplet off the surface irrespective of the value of contact angle.

Figure 5.13 shows the temporal evolution of the droplet for the case when $\lambda = 10$ and $\theta = 30°$. At time $t = 0$, the droplet interface makes an angle $\theta = 90°$ with the wall and hence during the initial evolution of the droplet, it spreads over the surface quickly, so as to make an angle $\theta \approx 30°$. But later, with time, the droplet moves away from the surface at a faster rate and forms a pear like shape (Fig. 5.13(c)). This pear shaped droplet is a double cone like structure which changes to single cone structure for $\theta = 90°$ and $120°$. Soon a liquid bridge forms separating a nearly spherical shaped droplet at its bottom and the remaining of the liquid attached to the surface. This liquid bridge elongates with time and finally a first rupture is noticed which separates the lower droplet. Due to the force unbalance created after liquid thread rupture, the liquid bridge accelerates and rolls back to form a small local spherical shape droplet at the bottom of the liquid thread (Fig. 5.13(e)). Also due to this local force unbalance, a flattened surface is noticed over the separated liquid drop (Fig. 5.13). The presence of dominant capillary waves after initial rupture on the liquid thread breaks it up again to form satellite droplets whose shape oscillates with time. The amount of liquid volume which remains stick to the surface reduces with the increase in the value of contact angle ($\theta = 60°$). However, for the other two cases i.e $\theta = 90°$ and $120°$, no residual amount of liquid is noticed on the surface. This can be seen from Fig. 5.12 (c), where the value of w reaches to zero with time for $\theta = 90°$ and $120°$, but for the other two cases it reaches to a finite value after initial oscillations.

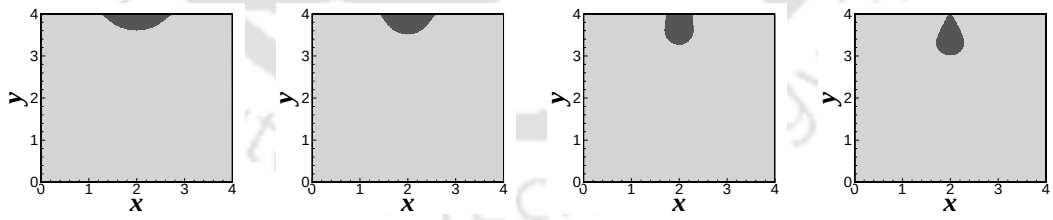

(a) (b) (c) (d)

Figure 5.9: Snapshots of droplet shape at time $t = 2.5$ for (a) $\theta = 30°$, (b) $\theta = 60°$, (c) $\theta = 90°$ and (d) $\theta = 120°$. The density ratio in this case is $\lambda = 1.5$.

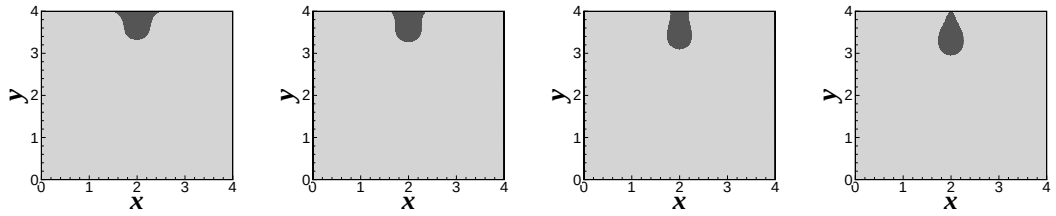

Figure 5.10: Snapshots of droplet shape at time $t = 1.2$ for (a) $\theta = 30°$, (b) $\theta = 60°$, (c) $\theta = 90°$ and (d) $\theta = 120°$. The density ratio in this case is $\lambda = 10$.

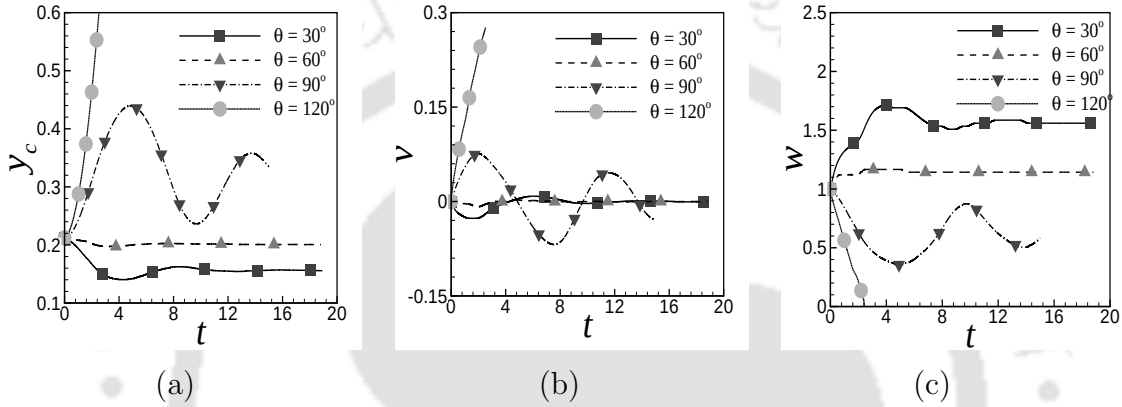

Figure 5.11: Temporal evolution of (a) droplet centroid y_c, (b) downward velocity v and (c) wetted length w for studying the effect of contact angle θ along with $\lambda = 1.5$.

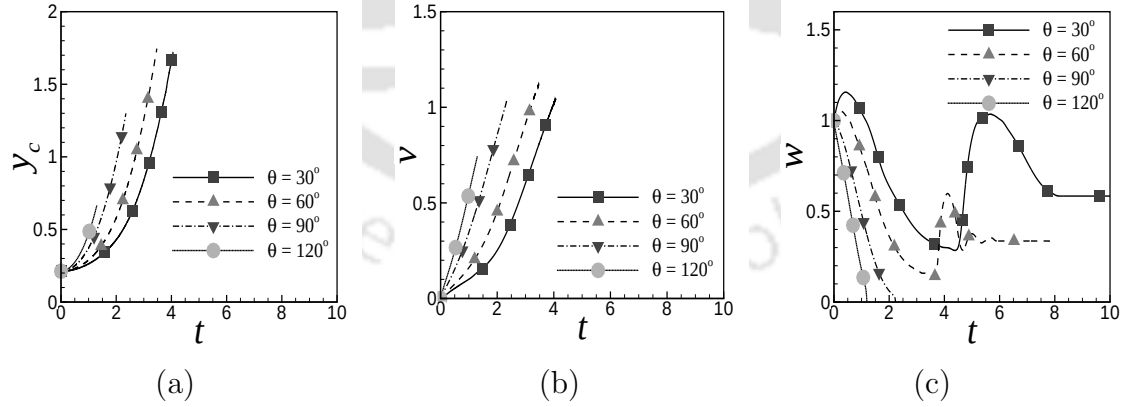

Figure 5.12: Temporal evolution of (a) droplet centroid y_c, (b) downward velocity v and (c) wetted length w for studying the effect of contact angle θ along with $\lambda = 10$.

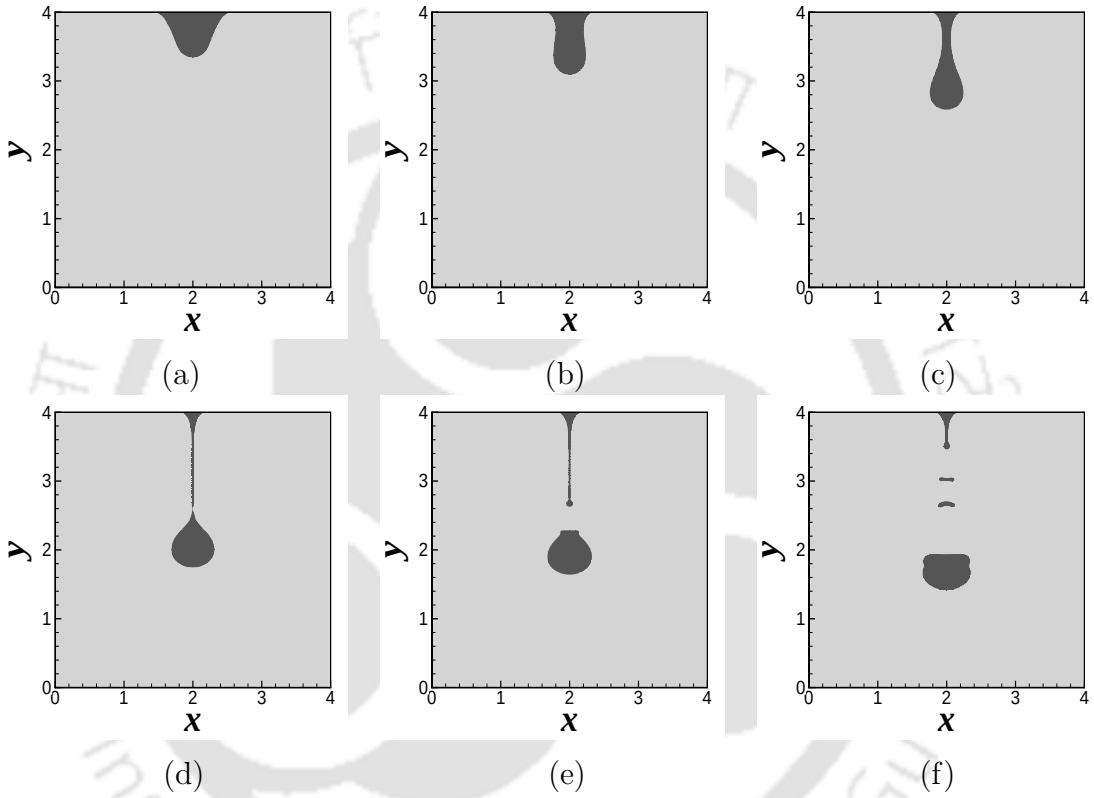

Figure 5.13: Evolution of droplet for the case of $\lambda = 10$ and $\theta = 30°$. Snapshots are shown at time $t = 1.0$, 2.0, 3.0, 4.0, 4.1 and 4.3.

5.4.4 Effect of multiple droplets

In the subsection 5.4.1, we noticed that at $\lambda = 1.5$, $We = 15$ and $\theta = 90°$, the droplet remained stick to the wall. While looking at the effects of We in subsection 5.4.2, we observed that, if the magnitude of surface tension is reduced by increasing the Weber number, the single droplet detaches from the wall. In this subsection, we reflect the droplet detachment process at lower contact angle for the case of two droplets. The dynamics of the same droplet at $\lambda = 1.5$, $We = 15$ and $\theta = 30°$ is analyzed in presence of another identical droplet in its vicinity (refer Fig. 5.1 (b)). Figure 5.14 shows the temporal evolution of the droplet shape in double droplet arrangement at time $t = 0$, 2.5, 5, 15, 30 and 35.7. The initial distance between the two droplets is equal to the radius of the droplet itself. The temporal evolution of various parameters for single and double droplet arrangements has been shown in Fig. 5.15. As it can be seen from the plots, upto time = 2.4, the behavior of double droplets is similar to that of the single droplet. The deviation begins with the two droplets merging into a single one at time $t = 2.30$. The single droplet attains to an equilibrium position after initial oscillations, while in the double droplet arrangement, the larger coalesced droplet detaches off the wall (after getting merged). From the plots (Fig. 5.15) it can be noticed that for the single droplet arrangement, droplet velocity damps out with time, whereas, its centroid y_c and vertical length l reach to a steady state value, leading to no detachment. But, for the double droplet arrangement, all the three geometrical quantities (y_c, l and v) increase with time until the droplet got separated into two parts. With the double droplet arrangement, we performed various simulations at higher contact angle as well. The droplet shapes after t = 2.5 are shown in Fig. 5.16. In all of these cases, the behavior of single and double droplets arrangement are identical and hence it can be said that, there is no effect of the surrounding droplet in these cases.

5.5 Closure

Apart from the solver development activities discussed in the previous chapters, herein, in this chapter, we presented a parametric study on the detachment of a droplet from horizontal surface. The effect of droplet affinity for two droplets is also studied using the simulations. Our results indicate that, for small densities of droplet, it adheres to the surface except when the surface is hydrophobic, while an

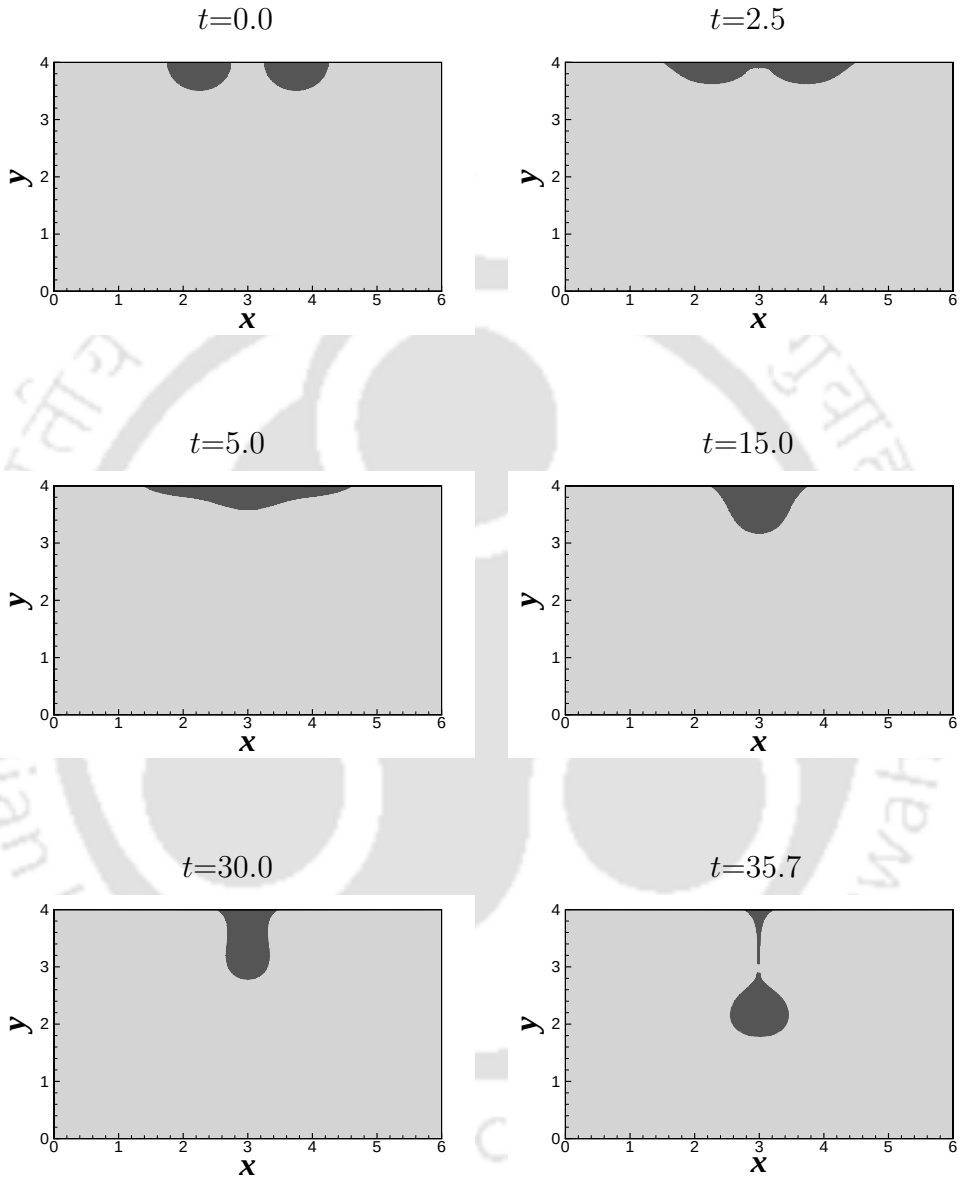

Figure 5.14: Snapshots of droplet shape with double droplet arrangement at different time instances for $\lambda = 1.5$ and $\theta = 30^{\circ}$

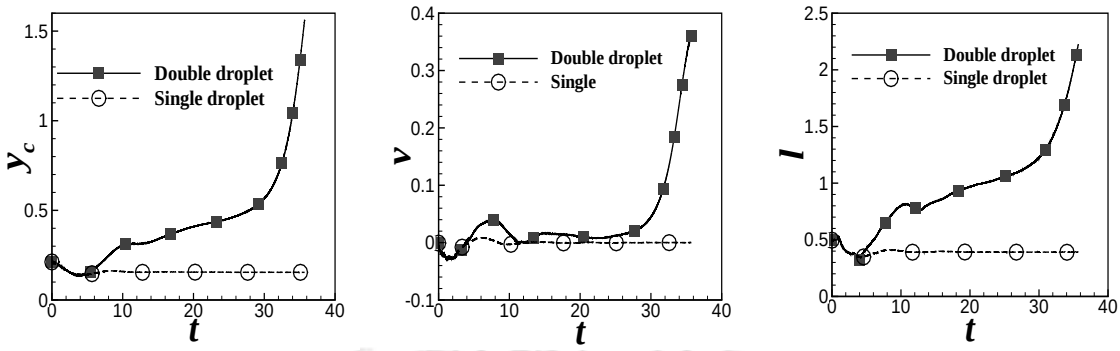

(a) (b) (c)

Figure 5.15: Temporal evolution of (a) droplet centroid y_c, (b) downward velocity v and (c) elongated length before detachment l for single and double droplet arrangements.

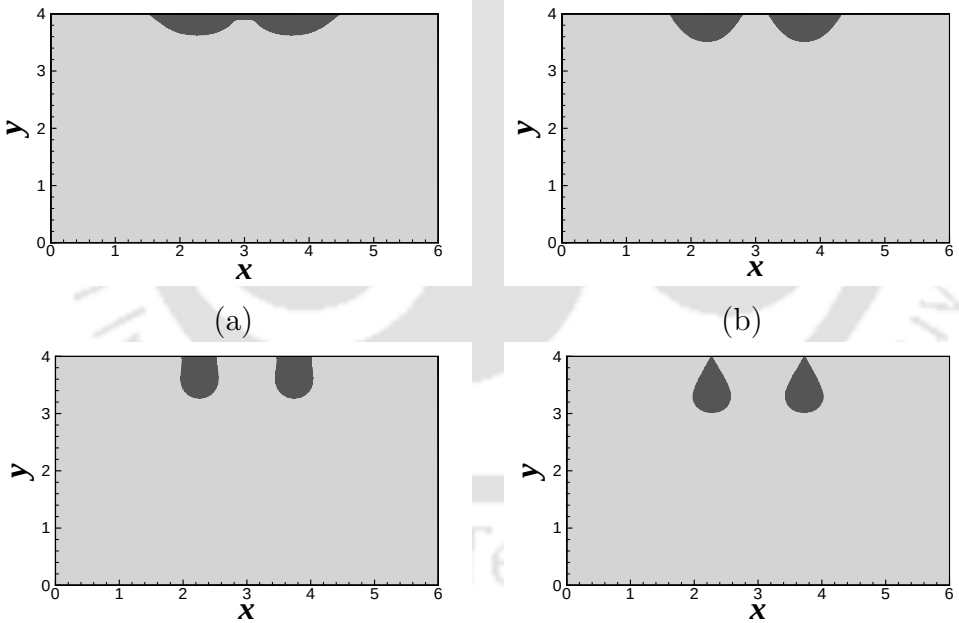

(a) (b)

(c) (d)

Figure 5.16: Snapshots of droplet shape at time $t = 2.5$ for (a) $\theta = 30°$, (b) $\theta = 60°$, (c) $\theta = 90°$ and (d) $\theta = 120°$. Density ratio in this case is $\lambda = 1.5$.

increase in Weber number or presence of an additional droplet in the vicinity led to detachment. The detachment is also observed for a given initial droplet size, as it become more denser in an uniform gravitational field.

Chapter 6

Droplet Falling Over Thin Liquid Film

6.1 Introduction

As in the droplet detachment study carried out in the previous chapter, the simulations were carried out over orthogonal meshes, herein, in this chapter we assess the capabilities of the solver to handle the droplet dynamics over non-orthogonal meshes. The problem considered in this work is the impingement of a droplet over thin liquid film with variable thickness. A lot of work has already been carried out to reveal the facinating dynamics of droplet impinging over thin liquid film with constant thickness. Hence, the aim of the present work is to study the behavior of liquid sheet due to the impingement of a droplet over variable thickess films. Also, later in the chapter, the effect of the angle with which the droplet impinges the liquid film is also considered.

6.2 Problem Specification

In this problem, we have considered three different geometrical arrangements as shown in Fig. 6.1 and in all the upcoming discussions, these will be referred to as arrangements or cases A, B and C. Apart from the flat horizontal surface case, in one situation, the droplet hits the trough region of the sinusoidally varying bottom

wall, whereas in the the other scenario, the droplet hits the crest portion. For the arrangements B and C, the bottom wall is considered to vary sinusoidally with an amplitude of 0.5. The width and height of the computational domain for all the arrangements are 5 and 3 units, respectively and is discretized using $\approx$ 50000 prism cells. The initial condition is shown in Fig. 6.1 and for the boundary conditions, a no slip wall is specified at the bottom wall, whereas, the other three boundaries are treated as open to atmosphere. The non-dimensionalization has been performed in the following way.

The relevant dimensionless characteristic variables are,

$$x^* = \frac{x}{D}; \quad \mathbf{u}^* = \frac{\mathbf{u}}{U}; \quad t^* = \frac{t}{D/U}; \quad \rho^* = \frac{\rho}{\rho_1}; \quad \mu^* = \frac{\mu}{\mu_1};$$

$$p^* = \frac{p}{\rho_1 \, U^2}; \quad \kappa^* = \frac{\kappa}{D^{-1}}$$

where D and U are the initial diameter and magnitude of impact velocity of the droplet, respectively. Fluid properties have been non-dimensionalized by the properties of heavier liquid. The resulting non-dimensional momentum equation takes the following form.

$$\frac{\partial \left(\rho^* \mathbf{u}^*\right)}{\partial t^*} + \nabla \cdot \left(\rho^* \mathbf{u}^* \mathbf{u}^*\right) = -\nabla p^* + \frac{1}{Re} \nabla \cdot \left[\mu^* \Big(\nabla \mathbf{u}^* + \nabla (\mathbf{u}^*)^T \Big)\right] + \frac{1}{We} \kappa^* \nabla f \quad (6.1)$$

where,

$$We = \frac{\rho_1 D U^2}{\sigma} \qquad Re = \frac{\rho_1 D U}{\mu_1}$$

6.3 Results and Discussion

In the following subsections, discussion is presented for normal ($\theta = 0°$) and oblique impact ($\theta > 0°$) of the droplet over varying thin liquid films. As per [128], the values of various non-dimensional parameters chosen for the study are Reynolds number as 100, Weber number as 800, non-dimensional minimum film thickness as 0.15, density ratio as 1000 and viscosity ratio as 100.

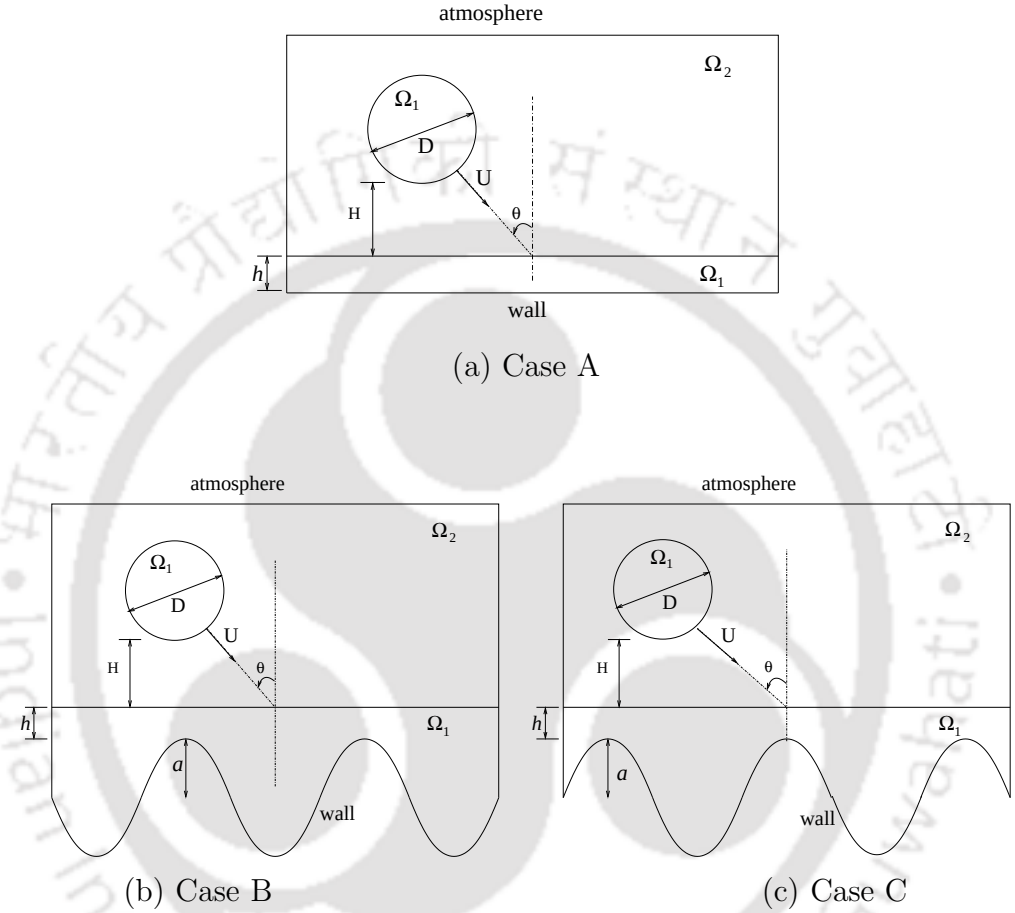

Figure 6.1: Computational geometry for droplet impinging over thin liquid film with constant and varying film thickness. Bottom wall is considered to be (a) straight horizontal surface or to vary sinusoidally with droplet either hitting (b) trough or (c) crest region.

6.3.1 Normal droplet impingement to the film surface

Here we discuss about the effect of the variable film thickness on the dynamics of crown formation by considering the impact to be normal to the film surface. Figure 6.2 shows the pictorial representation of droplet impingement at two different time instances $t^* = 0.2$ and 1.0 for all the three geometrical arrangements. Along with the contour plots of volume fraction, velocity vectors are also plotted and due to the symmetric nature of the problem, only one half of the domain is shown. Considering the case of constant film thickness (arrangement A), initially, when the droplet hits the liquid film, a gas jet is formed in the region between the droplet and the film (Fig. 6.2 (a) at $t^* = 0.2$). The pressure at the point of impingement increases with time and the deformation of the liquid film starts occurring. The deformation later leads to the formation of a liquid jet which gets assisted by the vortex formed on the lighter side of the liquid to produce a crown like structure. The vortex which is noticed near to the droplet on the lighter side of the liquid has earlier been reported as well [3, 128]. While maintaining the contact with both the droplet and the liquid film, the diameter and height of the liquid sheet or jet increase with time. Along with this, in addition to the primary vortex (attached to the droplet and above the jet), a secondary vortex has also been noticed in the region between the undisturbed liquid film and the lower portion of the liquid sheet (Fig. 6.3 (a)). However, the formation of this secondary vortex takes place only after a certain time interval or in other words, when the jet height reaches to a certain limit.

In the case of arrangement B, i.e. when the droplet hits the trough portion of the sinusoidally varying bottom wall, a similar initial gas jet and the formation of primary and secondary vortices has been noticed. In this case, since the film is varying sinusoidally, the depth of film is maximum under the location where droplet initially hits the film. Once the droplet sufficiently merges with the film, the initial stationary liquid of the film is pushed through the sinusoidal wall and is guided to move upward. This vertical momentum is responsible for the increase in the height of the jets and also to some extent, for retarding the radial growth of the liquid sheets as well. For normal impinging droplets, in order to make a quantative comparison between the three cases, the temporal evolution of various geometrical properties (refer Fig. 6.4) is monitored and is shown in Fig. 6.5. We can clearly notice that, when compared against case A, the rate of the increase in height of the jets for case

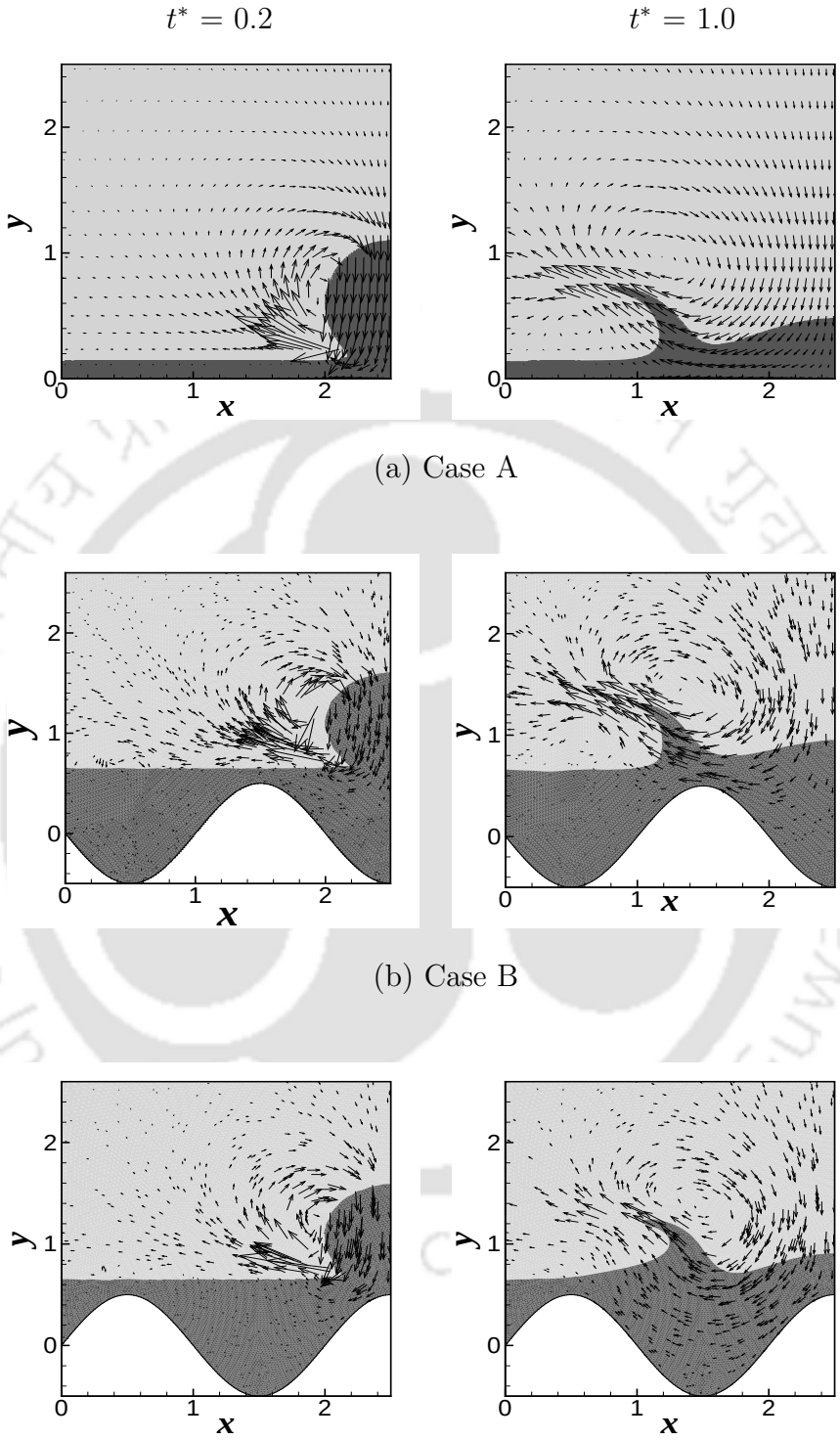

(a) Case A

(b) Case B

(c) Case C

Figure 6.2: Contour plots of volume fraction along with the vector plots at two different time instances $t^* = 0.2$ and 1.0 for (a) constant film thickness and a sinusoidally varying film thickness with droplet either hitting (b) trough or (c) crest region.

B increases, while the rate at which these jets expands radially is decreased.

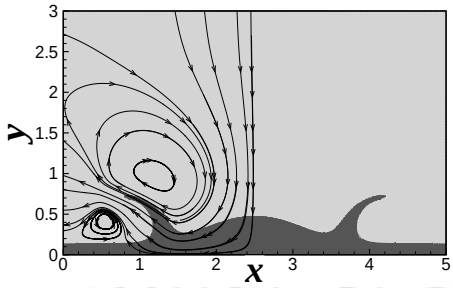

(a) Case A

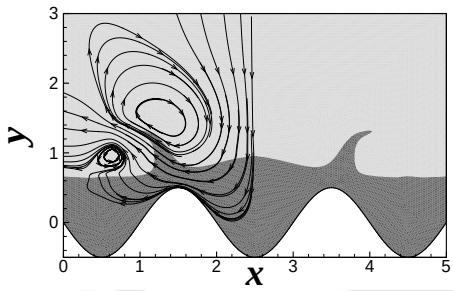

(b) Case B

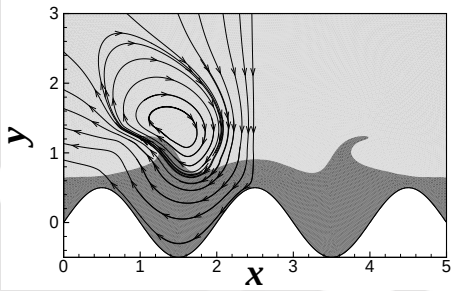

(c) Case C

Figure 6.3: Contour plots of volume fraction along with the streamlines at time t^* = 1.0 for all the three cases.

Considering the last case, i.e. when the droplet hits the peak portion of the sinusoidally varying bottom wall (case C), the droplet actually hits the film where the thickness is minimum. This is in contrast with the earlier case (case B), wherein the droplet was hitting at a location where the thickness of the film is maximum. Similar to the case B, in this case as well, the stationary liquid of the film is guided through the sinusoidal wall to move upward. But in this case, instead of assisting the jet to increase its height, this vertical momentum is responsible for lifting the film surface near to the base of the liquid sheet. Hence, the thickness of the base of the liquid jet increases with time. In order to quantify this upliftment, L is plotted for all the three cases at a distance of $x = 0.8$. It can be observed from Fig. 6.5 (b) that for case C, the value of L increases sharply with time and its value is sufficiently higher than the other two cases. From now onwards, this phenomenon, wherein the

vertical momentum lifts up the liquid surface near to the base of the liquid sheets will be termed as "$liftup$" phenomenon.

Also, from Fig. 6.3, wherein the contour plots along with the streamlines are shown for all the three cases at time $t^* = 1.0$, we can notice that in comparison to the other two cases, the secondary vortex is completely absent in case C. Initially, like the previous two cases, a gas jet and the formation of primary vortex is noticed, but later on, when the formation of secondary vortex is expected, the "$liftup$"phenomenon completely suppresses it. It is also to be noticed that this $liftup$ phenomenon is responsible for the retardation of the radial growth of the jets as well.

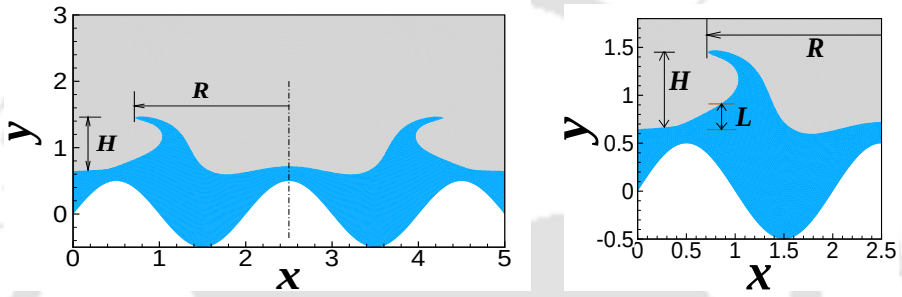

Figure 6.4: Various geometrical properties for quantitative evaluation of the normal droplet impingement over thin liquid film.

6.3.2 Droplet impingement at an angle to the film surface

In the previous subsection, effect of droplet impingement normal to the liquid surface has been studied. The changes in the crown dynamics due to the oblique impact of the droplet has now been considered in this subsection. It is to be noted that, in the earlier study, the evolution of the jet was symmetric about the vertical axis, but for an oblique impact, it is asymmetric in nature. In Fig. 6.6, according to the direction of the droplet impact, the two halves of the domain are defined as upstream and the downstream side. In order to qualitatively evaluate the changes in the jet dynamics, temporal evolution of the following parameters are considered.

1. Maximum reach of the jet in the radial direction on the upstream side (R_U).

2. Maximum reach of the jet in the radial direction on the downstream side (R_D).

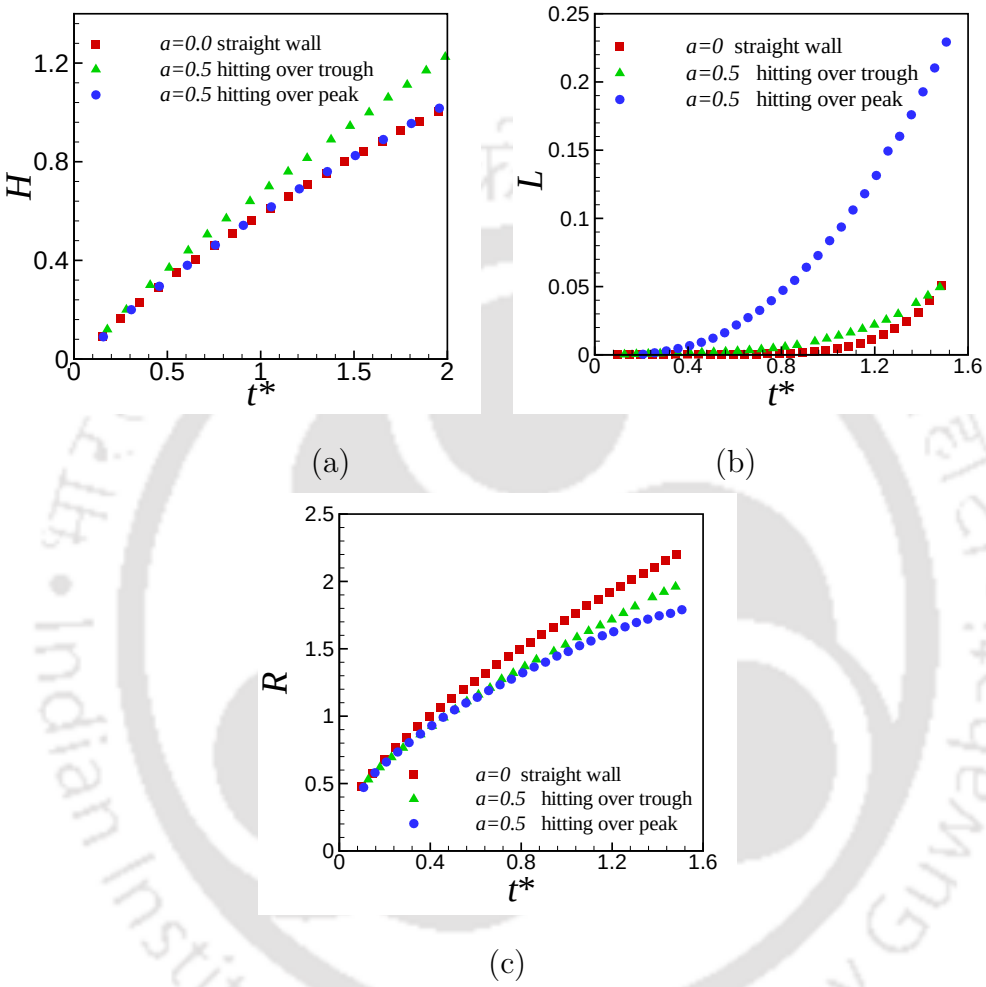

Figure 6.5: For the droplet impingement over varying film case, the variation of (a) height (H), (b) length (L) and (c) radius (R) are plotted with time.

3. Jet height on the upstream side (H_U).

4. Jet height on the downstream side (H_D).

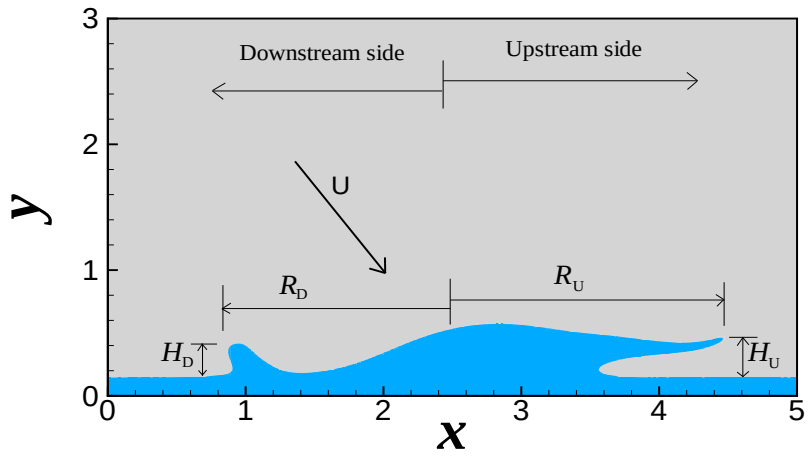

Figure 6.6: Various geometrical properties for quantitative evaluation of oblique droplet impact over thin liquid film.

For an impact angle of θ=30°, Figs. 6.7 (a)-(c) show the temporal evolution of liquid sheets for cases A, B and C, respectively. As compared to the previous study i.e normal droplet impact, in these cases the jet is asymmetric in nature and also its evolution on the upstream side is more. This is obvious, because of the fact that the flux which is fed from the droplet to the crown is larger on the upstream side. This unequal fluxes on the upstream and downstream side produce non-uniform velocity distribution and ultimately give rise to non-uniform jetting as well. For the case A, on either side of the growth of the liquid sheets, jetting phenomenon is observed. Due to this non-uniform jetting, the vortices formed on the upstream and downstream side are dissimilar in structure. Although, similar to the normal impact cases, these vortices initially remain attached to the droplet, but there are significant differences in the rate at which they moves horizonatlly (radially) and vertically. From the Fig. 6.7 (a), it can be noticed that the rate at which the vortex moves radially on the upstream side is more when compared with that of its movement in the downstream direction. Also, it has been noted that, with the evolution of the liquid sheet, these vortices remain in the region near to the tip of the jet.

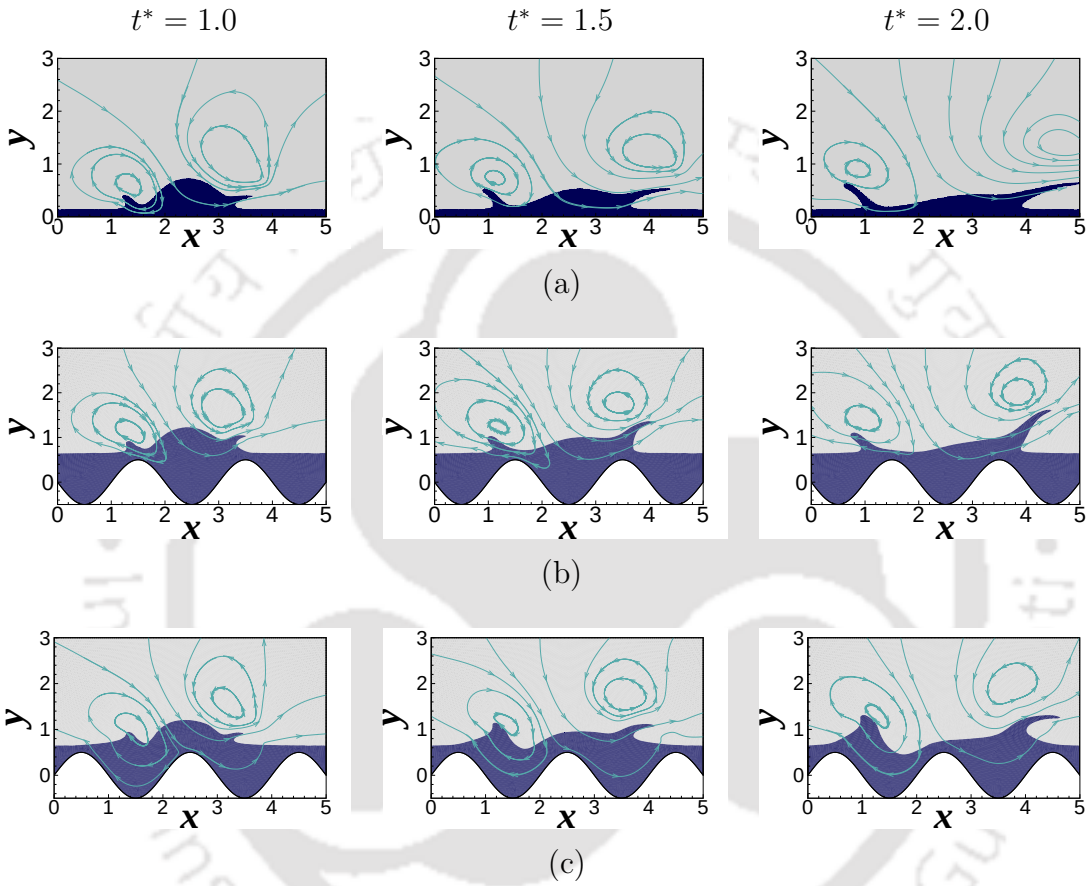

Figure 6.7: Snapshots of droplet impingement over constant and varying thin liquid film at different non-dimensional time instants. (a) Plain horizontal wall and (b) sinusoidally varying wall with droplet either hitting over trough or (c) peak portions. The angle with which the droplet is impinging the film is taken as 30°.

When the case B is considered, i.e. when the droplet hits the trough portion of the sinusoidally varying bottom wall, in comparison to the case A, a decrease in the radial growth of the liquid sheets or jets on the either sides has been noticed. But at the same time, an intensified rate of the growth of the jet height on the upstream side has been observed (refer Fig. 6.8). The primary reason behind this is the guidance of the liquid film from the sinusoidally rising bottom walls. As it can be seen from Fig. 6.7 (b), when the droplet suficiently merges with the film, the liquid present near to the wall is guided to move upward. This on the other hand assists the jet on the upstream side to rise even more. Hence, the upstream jet, which was comparitively horizontal for the case A, has now became a bit vertical.

Finally, in the case of arrangement C, instead of a sharp jet, phenomenon similar to deposition is observed on the downstream side. This may be attributed to the $liftup$ phenomenon, which is more dominant on the downstream side. Also, it can be noticed from Fig. 6.8, that due to this $liftup$ phenomenon only, the rate of the increase of vertical height of the liquid sheet on the downstream side is highest for case C. However, on the upstream side, this rate is marginally higher than the case A and lower than that of the case B.

Further, the studies are again carried out for an impact angle of θ=45°. In Figs. 6.9 (a)-(c), pictorial representations of the dynamics of the liquid sheet propagation are shown for all the three cases. Also, in Fig. 6.10, temporal evolution of all the relevant geometrical quantities has been plotted. The trends are alomost similar to that of the cases with θ=30°.

When the sole effect of the contact angle for each individual case is considered, it is noticed that, irrespective of the cases under consideration (case A, case B or case C), the rate of the increase of height of the liquid sheet on either side decreases with the increase in the value of impinging angle θ. A similar finding has been reported by Cheng and Lou [102] as well. Their study with three dimensional numerical simulations revealed that with the increase in the value of impinging angle, the jet height decreases. However, they have considered only constant film thickness, but in the present work, a similar trend is being observed even for varying film thickness. The variation of the height of the liquid sheet for different impact angle over different geometries is shown in Fig. 6.11. It can be easily observed that for all the three

cases, an increase in the impact angle decreases the jet height on either side.

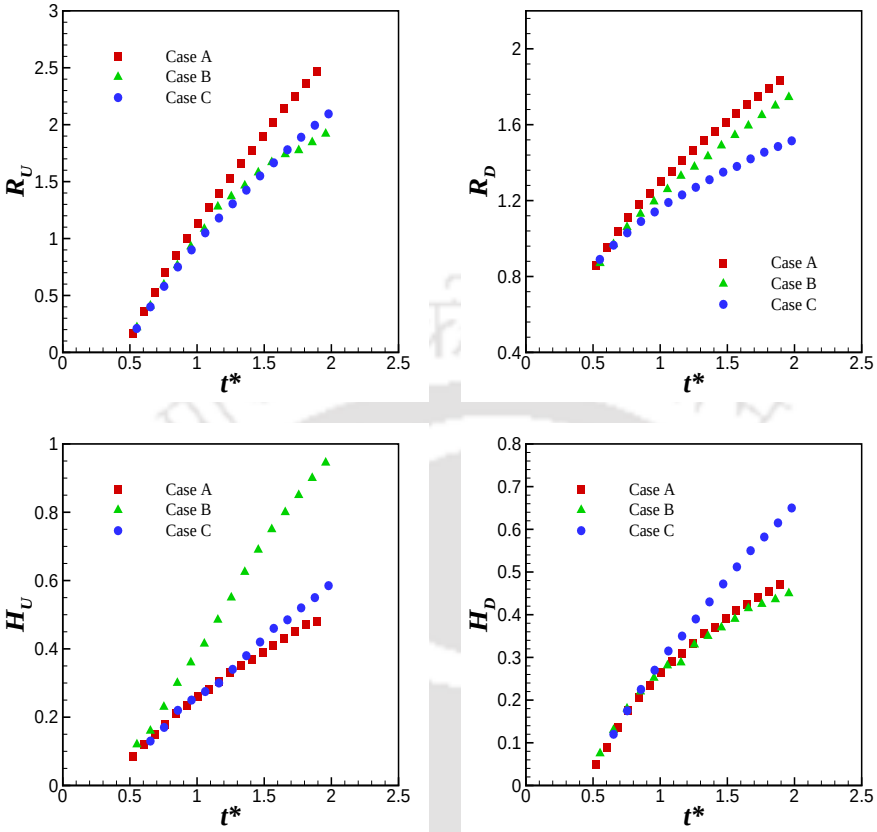

Figure 6.8: Comparision of the evolution of different geometrical parameters for different cases. The angle of impact is θ=30°.

6.4 Closure

In this chapter, we presented the results of droplet impinging over thin liquid film with varying thickness. In order to achieve this varying thickness, we considered the bottom wall to vary sinusoidally. Cases including droplet falling over peak and trough portion of the sinusoidally varying bottom wall has been compared against the constant film thickness case. Apart from the normal droplet impinging cases, effect of oblique impact has also been studied.

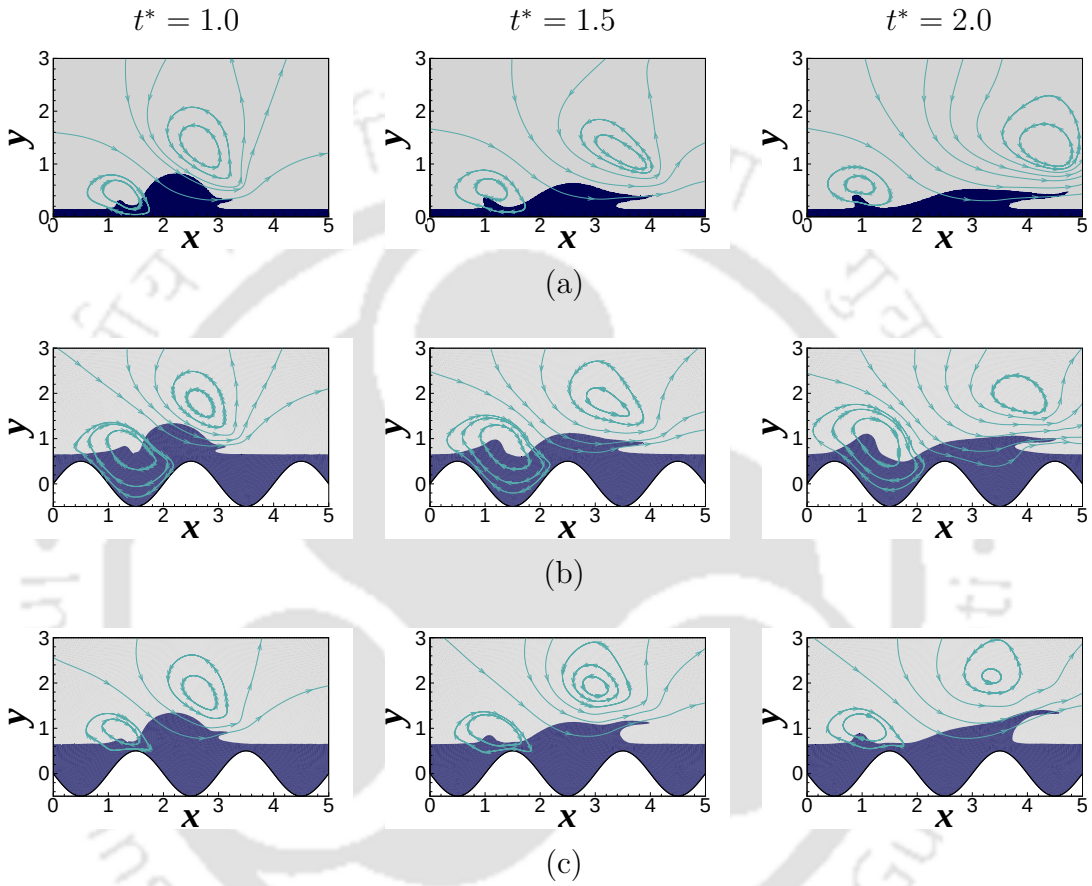

Figure 6.9: Snapshots of droplet impingement over constant and varying thin liquid film at different non-dimensional time instants. (a) Plain horizontal wall and (b) sinusoidally varying wall with droplet hittion over crest and (c) trough portions. The angle with which the droplet is impinging the film is taken as 45°.

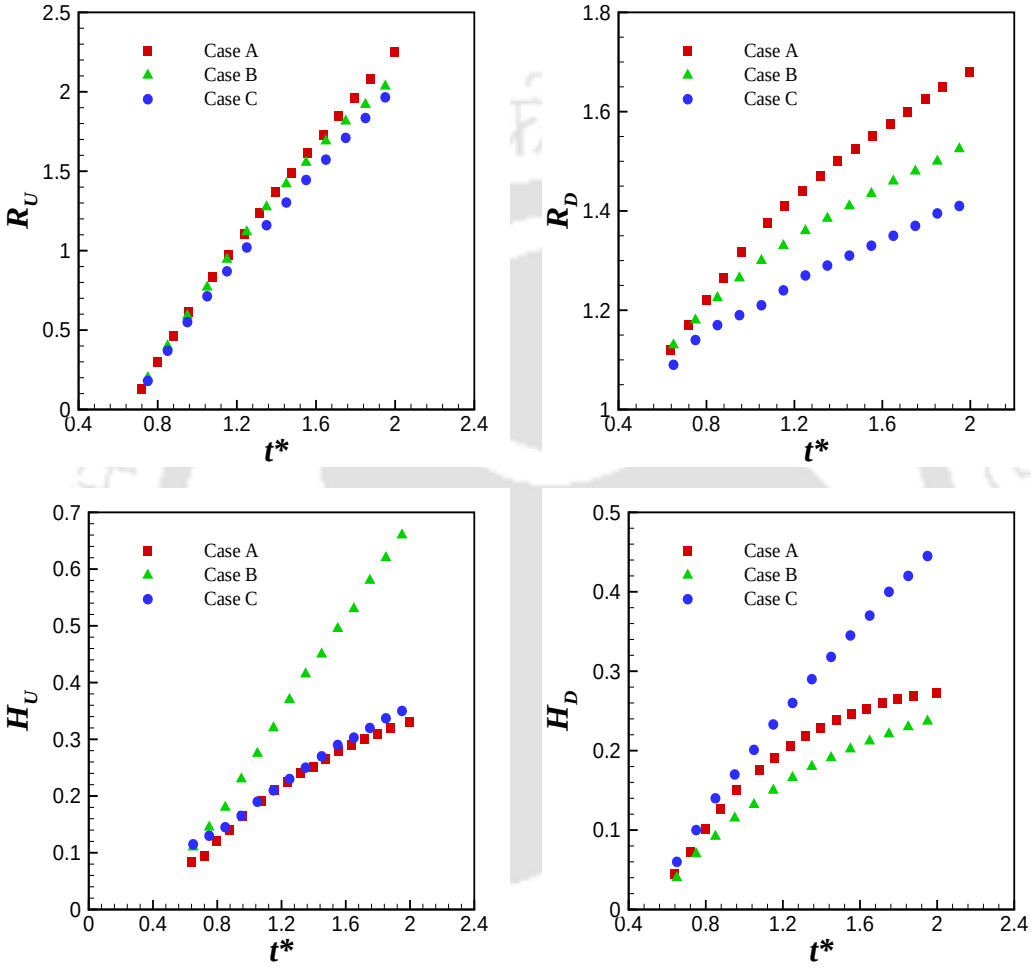

Figure 6.10: Comparision of the evolution of different geometrical parameters for different cases. The angle of impact is θ=45°.

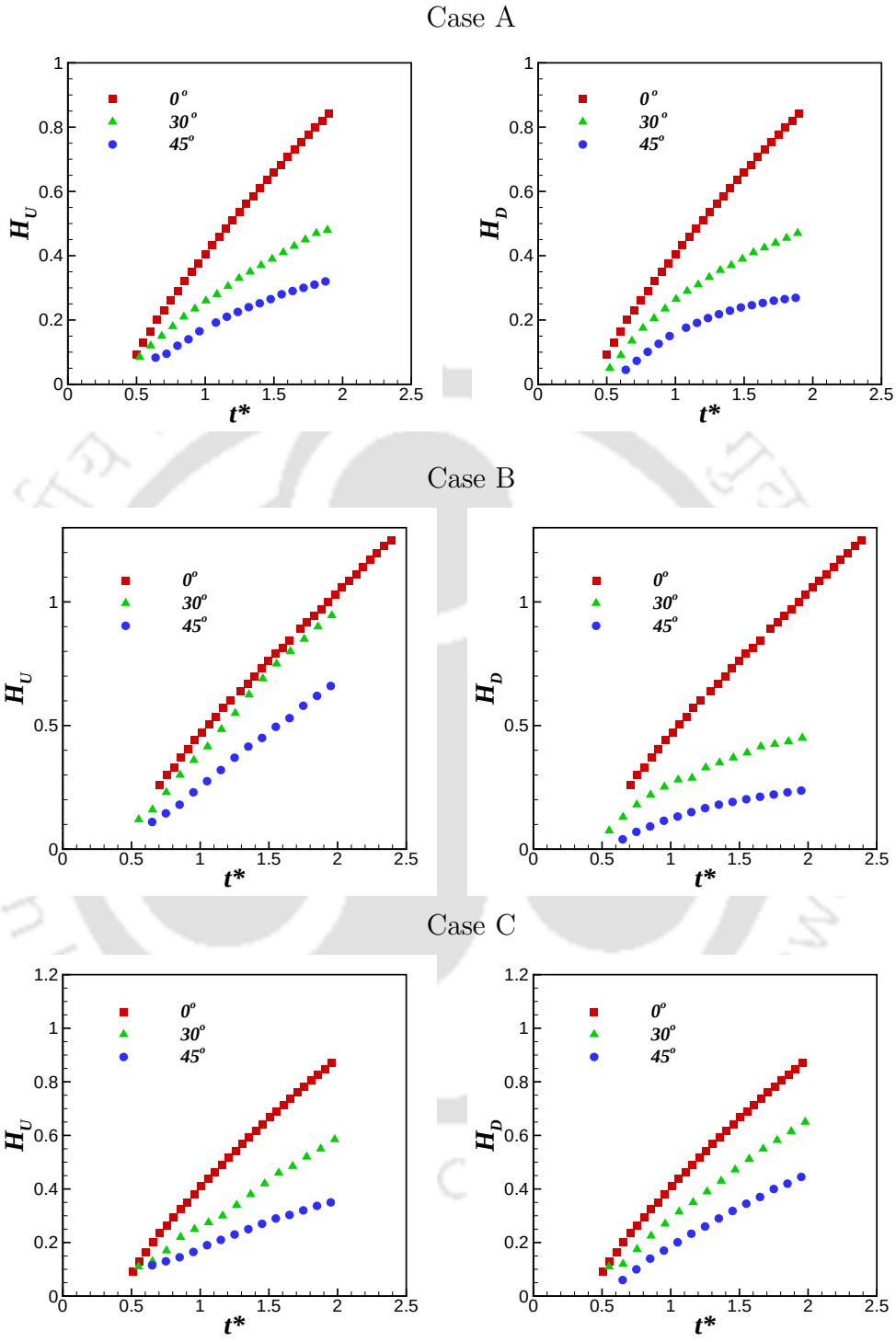

Figure 6.11: Comparision of the height of the jet on upstream and downstream side for different impact angle and for different geometries.

Chapter 7

Conclusions and Scope of Future Work

7.1 Conclusions

The thesis presents the development of a three-dimensional multiphase solver on hybrid unstructured grid. Well balanced and consistent algorithm for simulating interfacial flows with high-density ratio has been implemented. Usually, multiphase flow algorithms suffer from a lack of balance between the competing forcing terms and therefore, unnecessary flow field (spurious currents) is developed near to the interface. These spurious currents generally increase with the increase in density ratio. In order to address these challenges, we propose a simple and efficient algorithm which not only reduces the spurious currents but also comes with a framework which can be easily implemented in any of the existing solver. The conclusions of the present work are summarized below.

Chapter 1 introduces the binary fluid flows along with the challenges associated with its numerical simulation. It is followed by a detailed literature survey on the existing methodologies to capture the phase interface sharply as well as the available class of algorithms to handle large interfacial and body forces.

A general numerical methodology in the finite volume framework for handling hybrid unstructured meshes is presented in chapter 2. The applicability of these

numerical techniques is then tested by solving the benchmark three-dimensional lid driven cavity problem. Along with this, a separate testing has been performed for the advection of volume fractions.

In Chapter 3, we present a detailed formulation and results of the proposed well balanced and consistent algorithm for simulating interfacial flows with high-density ratio over hybrid unstructured meshes. We worked on with two aspects of the algorithm. First, we looked on to the force balancing needed at discrete level among different source terms of the momentum equations and secondly, on the treatment of convective terms appearing in momentum as well as advection equations. In order to achieve proper force balancing, we employed least squares method of gradient reconstruction at the cell centroid together with considering all the competing forces in a single equation i.e pressure Poisson equation. Next, we looked on to the effect of using similar and dissimilar convective scheme among different equations and termed them as consistent and inconsistent treatment, respectively. With the help of a series of test cases including static droplet, static tank, filling of a column, convection of an inviscid droplet, the benchmark case of rising of a bubble, dam break against an obstacle and the splashing of a droplet over thin liquid film, we demonstrated the effectiveness of the present solver to handle binary fluid flows involving high density and viscosity ratio.

Chapter 4 presents an alternative approach for achieving proper force balancing. This method, which we termed as modified Green Gauss method, is also an interpolation free approach similar to least squares method, but when compared on the grounds of implementation strategy, modified Green Gauss method appears to be a comparatively simple and cheaper method. In order to check the applicability of the proposed modified approach, in addition to the test cases performed using least squares method, problems including marangoni stress and gravitational force in volumetric form have also been solved and the results are found to be as accurate as those of the least squares method.

Then the developed solver has been applied to solve two pertinent problems related to two-components fluids and the results are presented in chapters 5 and 6.

In chapter 5, the investigations have been carried out to explore the fascinating

dynamics of droplets detachment from a horizontal wall. The effects of various parameters including density ratio, viscosity ratio, surface wettability, Weber number (We) and the presence of surrounding droplet have been considered. The salient conclusions from the droplet detachment study are summarized below,

- For the cases having low density ratio together with lower value of We, force due to gravitational pull is not sufficient enough to overcome the effect of wall adherence, leading to the sticking of droplet on the surface itself.
- We number plays a significant role in the droplet detachment process. Values of the We beyond a particular limit cause the droplet to leave the surface even at a very low density ratio.
- Lower values of density ratio together with higher values of We number yield satellite droplets while detachment. The number of satellite droplets increases with the increase in We number.
- Irrespective of the density ratio, detachment of the droplet has been observed for all the hydrophobic surfaces. But, when the surface is considered to be hydrophilic in nature, density ratio plays a major role in the detachment process. At higher density ratio, droplet detaches off the surface even at a very low value of contact angle.
- Effect of the presence of adjacent droplet has been observed only for a single case i.e when the value of contact angle and density ratio are very low. The two droplets got merged to form a larger coalesced droplet, which later split into two parts while detaching from the wall.

In chapter 6, the dynamics of the droplet impingement over thin liquid film with varying thickness has been explored. In order to vary the bottom film thickness, a sinusoidally varying wall with an amplitude of 0.5 is considered. The major findings of this study is summarized as follows.

- For normal droplet impact, the thickness of the crown base increases for the case when droplet hits the peak portion of the sinusoidally varying wall.
- As compared to constant film thickness case, a reduction in the crown growth rate in radial direction has been noticed for oblique impacts over sinusoidally varying wall.

- It has also been noticed that, as the angle with which the droplet impinges increases, the height of the crown decreases.

7.2 Scope of Future Work

Although the present work provides a detailed insights to the development of a well balanced algorithm for multiphase flows, still there are too many directions which can be explored in near future. Some of them are listed below,

- The present algorithm handles only isothermal flows and applications such as mould filling with molten metal need to resolve the temperature of the domain as well. Hence, in addition to the governing equations considered in this work, an additional equation for the conservation of energy needs to be clubbed with the present solver.
- Immiscible flow occurs in a wide variety of industrial problems and can be handled with the present approach, but in order to solve the problems of mixing of two fluids inside a micro channel, necessary changes has to be made in the present formulation. An additional term associated with the diffusion of the two fluids near to the interface needs to be accounted properly.
- There exists a huge number of applications where wall contact angle plays a major role. In the present study only static contact angle has been considered that too in two dimensional studies only. Therefore, proper attention needs to be focussed on the implementation of dynamic contact angle over three dimensional geometries.
- The existing solver runs on a single processor only and hence, in order solve some of the complex three dimensional industrial problems, it needs to be parallelized for getting faster solutions.
- Effect of density ratio on the generation of spurious currents has been studied in the present work. However, viscosity ratio also plays a significant role on the generation of unwanted flow fields. This study along with an alternative interpolation technique (harmonic mean) can be studied in the future course of action.

References

[1] Hysing S., Turek S., Kuzmin D., Parolini N., Burman E., Ganesan S., and Tobiska L. (2008) 'Quantitative benchmark computations of two-dimensional bubble dynamics', *International Journal for Numerical Methods in Fluids*, vol. 60, pp. 1259–1288.

[2] Rieber M. and Frohn A. (1999) 'A numerical study on the mechanism of splashing', *International Journal of Heat and Fluid Flow*, vol. 20, pp. 455–461.

[3] Nikolopoulos N., Theodorakakos A., and Bergeles G. (2005) 'Normal impingement onto a wall film: a numerical investigation', *International Journal of Heat and Fluid Flow*, vol. 26, pp. 119–132.

[4] Nikolopoulos N., Theodorakakos A., and Bergeles G. (2007) 'Three-dimensional numerical investigation of a droplet impinging normally onto a wall film', *Journal of Computational Physics*, vol. 225, pp. 322–341.

[5] Klostermann J., Schaake K., and Schwarze R. (2012) 'Numerical simulation of a single rising bubble by vof with surface compression', *International Journal for Numerical Methods in Fluids*, vol. 71, pp. 960–982.

[6] Williams M., Kothe D., and Puckett E. (1999) 'Convergence and accuracy of continuum surface tension models, in: W. shyy, r. narayanan (eds.)', *Fluid Dynamics at Interface, Cambridge University Press, Cambridge*, pp. 294–305.

[7] Renardy Y. and Renardy M. (2002) 'Prost: A parabolic reconstruction of surface tension for the volume of fluid method', *Journal of Computational Physics*, vol. 183, pp. 400–421.

[8] Aulisa E., Manservisi S., Scardovelli R., and Zaleski S. (2003) 'A geometrical area-preserving volume-of-fluid advection method', *Journal of Computational Physics*, vol. 192, pp. 355–364.

[9] Lopez J., Hernandez J., Gomez P., and Faura F. (2005) 'An improved plic-vof method for tracking thin fluid structures in incompressible two-phase flows', *Journal of Computational Physics*, vol. 208, pp. 51–74.

[10] Sussman M., Smereka P., and Osher S. (1994) 'A level set approach for computing solutions to incompressible two-phase flow', *Journal of Computational Physics*, vol. 114, pp. 146–159.

[11] Sussman M., Fatemi E., Smereka P., and Osher S. (1998) 'An improved level set method for incompressible two-phase flows', *Computers and Fluids*, vol. 27, pp. 663–680.

[12] Sussman M., Smith K., Hussaini M., Ohta M., and Zhi-Wei R. (2007) 'A sharp interface method for incompressible two-phase flows', *Journal of Computational Physics*, vol. 221, pp. 469–505.

[13] Sussman M. and Puckett E.G. (2000) 'A coupled level set and volume-of-fluid method for computing 3d and axisymmetric incompressible two-phase flows', *Journal of Computational Physics*, vol. 162, pp. 301–337.

[14] Albadawi A., Donoghue D., Robinson A., Murray D., and Delaure Y. (2013) 'On the analysis of bubble growth and detachment at low capillary and bond numbers using volume of fluid and level set methods', *Chemical Engineering Science*, vol. 90, pp. 77–91.

[15] Sun Y. and Beckermann C. (2007) 'Sharp interface tracking using the phase-field equation', *Journal of Computational Physics*, vol. 220, pp. 626–653.

[16] DeBar R. (1974) 'Fundamentals of the kraken code, technical report ucir-760, llnl', vol. 90, pp. 77–91.

[17] Noh W.F. and Woodward P.R. (1976) 'Slic (simple line interface method), in lecture notes in physics 59, edited by A. I. van de Vooren and P. J. Zandbergen', , pp. 330–340.

[18] Hirt C.W. and Nichols B.D. (1981) 'Volume of fluid (vof) method for the dynamics of free boundaries', *Journal of Computational Physics*, vol. 39, pp. 201–225.

[19] Youngs D.L. (1982) 'Time-dependent multi-material flow with large fluid distortion', *in Numerical Methods for Fluid Dynamics, edited by K. W. Morton and M. J. Baines*, pp. 273–285.

[20] Ginzburg I. and Wittum G. (2001) 'Two-phase flows on interface refined grids modeled with vof, staggered finite volumes, and spline interpolants', *Journal of Computational Physics*, vol. 166, pp. 302–335.

[21] Scardovelli R. and Zaleski S. (2003) 'Interface reconstruction with least-square fit and split eulerian-lagragian advection', *International Journal for Numerical Methods in Fluids*, vol. 41, pp. 251–274.

[22] Ubbink O. and Issa R.I. (1999) 'A method for capturing sharp fluid interfaces on arbitrary meshes', *Journal of Computational Physics*, vol. 153, pp. 26–50.

[23] Jasak H., Weller H., and Gosman A. (1999) 'High resolution nvd differencing scheme for arbitrarily unstructured meshes', *International Journal for Numerical Methods in Fluids*, vol. 31, pp. 431–449.

[24] Alves M.A., Oliveira P.J., and Pinho F.T. (2003) 'A convergent and universally bounded interpolation scheme for the treatment of advection', *International Journal for Numerical Methods in Fluids*, vol. 41, pp. 47–75.

[25] Tsui Y., Lin S., and Wu T. (2009) 'Flux-blending schemes for interface capture in two-fluid flows', *International Journal of Heat and Mass Transfer*, vol. 52, pp. 5547–5556.

[26] Darwish M. and Moukalled F. (2006) 'Convective schemes for capturing interfaces of free-surface flows on unstructured grids', *Numerical Heat Transfer, Part B*, vol. 49, pp. 19–42.

[27] Cassidy D.A., Edwards J.R., and Tian M. (2009) 'An investigation of interface-sharpening schemes for multi-phase mixture flows', *Journal of Computational Physics*, vol. 228, pp. 5628–5649.

[28] So K., Hu X., and Adams N. (2011) 'Anti-diffusion method for interface steepening in two-phase incompressible flow', *Journal of Computational Physics*, vol. 230, pp. 5155–5177.

[29] Patel J.K. and Natarajan G. (2015) 'A generic framework for design of interface capturing schemes for multi-fluid flows', *Computers and Fluids*, vol. 106, pp. 108–118.

[30] Osher S. and Sethian J.A. (1988) 'Front propagation with curvature dependent speed: Algorithm based on hamilton-jacobi formulations', *Journal of Computational Physics*, vol. 79, pp. 12–49.

[31] Sussman M., Smereka P., and Osher S. (1994) 'A level set approach for computing solutions to incompressible two phase flow', *Journal of Computational Physics*, vol. 114, pp. 146–159.

[32] Sussman M., Fatemi E., Smereka P., and Osher S. (1998) 'An improved level set method for incompressible two-phase flows', *Computers and Fluids*, vol. 27, pp. 663–680.

[33] Kees C., Akkerman I., Farthing M., and Bazilevs Y. (2011) 'A conservative level set method suitable for variable-order approximations and unstructured meshes', *Journal of Computational Physics*, vol. 230, pp. 4536–4558.

[34] Chang Y.C., Hou T.Y., Merriman B., and Osher S. (1996) 'A level set formulation of eulerian interface capturing methods for incompressible fluid flows', *Journal of Computational Physics*, vol. 124, pp. 449–464.

[35] Albadawi A., Donoghue D., Robinson A., Murray D., and Delaure Y. (2013) 'Influence of surface tension implementation in volume of fluid and coupled volume of fluid with level set methods for bubble growth and detachment', *International Journal of Multiphase Flow*, vol. 53, pp. 11–28.

[36] Chakraborty I., Biswas G., and Ghoshdastidar P. (2013) 'A coupled level-set and volume-of-fluid method for the buoyant rise of gas bubbles in liquids', *International Journal of Heat and Mass Transfer*, vol. 58, pp. 240–259.

[37] Li Q., Ouyang J., Yang B., and Li X. (2012) 'Numerical simulation of gas-assisted injection molding using clsvof method', *Applied Mathematical Modelling*, vol. 36, pp. 2262–2274.

[38] Sussman M. (2003) 'A second order coupled level set and volume-of-fluid method for computing growth and collapse of vapor bubbles', *Journal of Computational Physics*, pp. 110–136.

[39] Wang Z., Yang J., Koo B., and Stern F. (2009) 'A coupled level set and volume-of-fluid method for sharp interface simulationof plunging breaking waves', *International Journal of Multiphase Flow*, vol. 35, pp. 227–246.

[40] Yang X. and James A.J. (2006) 'Analytic relations for reconstructing piecewise linear interfaces in triangular and tetrahedral grids', *Journal of Computational Physics*, vol. 214, pp. 41–54.

[41] Lv X., Zou Q., Zhao Y., and Reeve D. (2010) 'A novel coupled level set and volume of fluid method for capturing on 3d tetrahedral grids', *Journal of Computational Physics*, vol. 229, pp. 2573–2604.

[42] Aulisa E., Manservisi S., and Scardovelli R. (2003) 'A mixed markers and volume of fluid method for the reconstruction and advection of interfaces in two phase and free boundary flows', *Journal of Computational Physics*, vol. 188, pp. 611–639.

[43] Menard T., Tanguy S., and Berlemont A. (2007) 'Coupling level set/vof/ghost fluid methods: Validation and application to 3d simulation of the primary break-up of a liquid jet', *International Journal of Multiphase Flow*, vol. 33, pp. 510–524.

[44] Desjardins O., Moureau V., and Pitsch H. (2008) 'An accurate conservative level set/ghost fluid method for simulating turbulent atomization', *Journal of Computational Physics*, vol. 227, pp. 8395–8416.

[45] Wang Y., Simakhina S., and Sussman M. (2012) 'A hybrid level set-volume constraint method for incompressible two-phase flow', *Journal of Computational Physics*, vol. 231, pp. 6438–6471.

[46] Chenadec V.L. and Pitsch H. (2013) 'A 3d unsplit forward/backward volume-of-fluid approach and coupling to the level set method', *Journal of Computational Physics*, vol. 233, pp. 10–33.

[47] Bao J. and Schaefer L. (2013) 'Lattice boltzmann equation model for multi-component multi-phase flow with high density ratios', *Applied Mathematical Modelling*, vol. 37, pp. 1860–1871.

[48] Ding H., Spelt P.D.M., and Shu C. (2007) 'Diffuse interface model for incompressible two-phase flows with large density ratios', *Journal of Computational Physics*, vol. 226, pp. 2078–2095.

[49] Brackbill J.U., Kothe D.B., and Zemach C. (1992) 'A continuum method for modeling surface tension', *Journal of Computational Physics*, vol. 100, pp. 335–354.

[50] Liu X.D., Fedkiw R.P., and Kang M. (2000) 'A boundary condition capturing method for poissons equation on irregular domains', *Journal of Computational Physics*, vol. 160, pp. 151–178.

[51] Gueyffier D., Nadim A., Li J., Scardovelli R., and Zaleski S. (1999) 'Volume of fluid interface tracking with smoothed surface stress methods for three-dimensional flows', *Journal of Computational Physics*, vol. 152, pp. 423–456.

[52] Lafaurie B., Nardone C., Scardovelli R., Zaleski S., and Zanetti G. (1994) 'Modelling merging and fragmentation in multiphase flows with surfer', *Journal of Computational Physics*, vol. 113, pp. 134–147.

[53] Francois M.M. and Swartz B.K. (2010) 'Interface curvature via volume fractions, heights, and mean values on nonuniform rectangular grids', *Journal of Computational Physics*, vol. 229, pp. 527–540.

[54] Herrmann M. (2008) 'A balanced force refined level set grid method for two-phase flows on unstructured flow solver grids', *Journal of Computational Physics*, vol. 227, pp. 2674–2706.

[55] Mahesh K., Constantinescu G., and Moin P. (2004) 'A numerical method for large-eddy simulation in complex geometries', *Journal of Computational Physics*, vol. 197, pp. 215–240.

[56] Mencinger J. and Zun I. (2007) 'On the finite volume discretization of discontinuous body force field on collocated grid: Application to vof method', *Journal of Computational Physics*, vol. 221, pp. 524–538.

[57] Rudman M. (1998) 'A volume-tracking method for incompressible multifluid flows with large density variations', *International Journal for Numerical Methods in Fluids*, vol. 28, pp. 357–378.

[58] Lorstad D., Francois M.M., Shyy W., and Fuchs L. (2004) 'Assessment of volume of fluid and immersed boundary methods for droplet computations', *International Journal for Numerical Methods in Fluids*, vol. 46, pp. 109–125.

[59] Denner F. and van Wachem B.G.M. (2014) 'Fully-coupled balanced-force vof framework for arbitrary meshes with least-squares curvature evaluation from volume fractions', *Numerical Heat Transfer, Part B*, vol. 65, pp. 218–255.

[60] Montazeri H., Bussmann M., and Mostaghimi J. (2012) 'Accurate implementation of forcing terms for two-phase flows into simple algorithm', *International Journal of Multiphase Flow*, vol. 45, pp. 40–52.

[61] Montazeri H. and Ward C.A. (2014) 'A balanced-force algorithm for two-phase flows', *Journal of Computational Physics*, vol. 257, pp. 645–669.

[62] Dalal A., Eswaran V., and Biswas G. (2008) 'A finite-volume method for Navier-Stokes equation on unstructured meshes', *Numerical Heat Transfer,Part B*, vol. 54(2), pp. 238–259.

[63] Perot B. (2000) 'Conservation properties of unstructured staggered mesh schemes', *Journal of Computational Physics*, vol. 159, pp. 58–89.

[64] Bussmann M., Kothe D., and Sicilian J. (2002) 'Modeling high density ratio incompressible interfacial flows engineering division summer meeting, montreal, canada', *Proceedings of ASME 2002 Fluids*.

[65] Ghods S. and Herrmann M. (2013) 'A consistent rescaled momentum transport method for simulating large density ratio incompressible multiphase flows using level set methods', *Physica Scripta*, vol. T155, pp. 014–50.

[66] Cho S.C., Wang Y., and Chen K.S. (2012) 'Droplet dynamics in a polymer electrolyte fuel cell gas flow channel: Forces, deformation and detachment. ii: Comparisons of analytical solution with numerical and experimental results', *Journal of Power Sources*, vol. 210, pp. 191–197.

[67] Bhushan B., Kochab K., and Junga Y.C. (2008) 'Nanostructures for superhydrophobicity and low adhesion', *Soft Matter*, vol. 4, pp. 1799–1804.

[68] Furmidge C.G.L. (1962) 'Studies at phase interfaces i. the sliding of liquid drops on solid surfaces and a theory for spray retention', *Journal of Colloid Science*, vol. 17, pp. 309–324.

[69] Schleizer A. and Bonnecaze A. (1999) 'Displacement of a two-dimensional immiscible droplet adhering to a wall in shear and pressure-driven flows', *Journal of Fluid Mechanics*, vol. 383, pp. 29–54.

[70] Kang Q., Zhang D., and Chen S. (2002) 'Displacement of a two-dimensional immiscible droplet in a channel', *Physics of Fluids*, vol. 14, p. 3203.

[71] Sui Y., Ding H., and Spelt P.D. (2014) 'Numerical simulations of flows with moving contact lines', *Annual Review of Fluid Mechanics*, vol. 46, pp. 97–119.

[72] Legendre D. and Maglio M. (2015) 'Comparison between numerical models for the simulation of moving contact lines', *Computers and Fluids*, vol. 113, pp. 2–13.

[73] Cox R.G. (1986) 'The dynamics of the spreading of liquids on a solid surface. part 1. viscous flow', *Journal of Fluid Mechanics*, vol. 168, pp. 169–194.

[74] Afkhami S., Zaleski S., and Bussmann M. (2009) 'A mesh-dependent model for applying dynamic contact angles to vof simulations', *Journal of Computational Physics*, vol. 228, pp. 5370–5389.

[75] Randive P., Dalal A., and Mukherjee P.P. (2014) 'Probing the influence of superhydrophobicity and mixed wettability on droplet displacement behavior', *Microfluid Nanofluid*, vol. 17, pp. 657–674.

[76] Randive P., Dalal A., Sahu K.C., Biswas G., and Mukherjee P.P. (2015) 'Lattice boltzmann method for modelling droplets on chemically heterogeneous and microstructured surfaces with large liquid-gas density ratio', *Physical Review E*, vol. 91, p. 053006.

[77] Norman C.E. and Miksis M.J. (2005) 'Dynamics of a gas bubble rising in an inclined channel at finite reynolds number', *Physics of Fluids*, vol. 17, p. 022102.

[78] Spelt P.D.M. (2006) 'Shear flow past two-dimensional droplets pinned or moving on an adhering channel wall at moderate reynolds numbers: a numerical study', *Journal of Fluid Mechanics*, vol. 561, pp. 439–436.

[79] Ahmed G., Sellier M., Jermy M., and Taylor M. (2014) 'Modeling the effects of contact angle hysteresis on the sliding of droplets down inclined surfaces', *European Journal of Mechanics B/Fluids*, vol. 48, pp. 218–230.

[80] Zhang J., Miksis M.J., and Bankoff S.G. (2006) 'Nonlinear dynamics of a two-dimensional viscous drop under shear flow', *Physics of Fluids*, vol. 18, p. 072106.

[81] Zhang X. and Basaran O.A. (1995) 'An experimental study of dynamics of drop formation', *Physics of Fluids*, vol. 7, p. 1184.

[82] Henderson D.M., Pritchard W.G., and Smolka L.B. (1997) 'On the pinch-off of a pendant drop of viscous fluid', *Physics of Fluids*, vol. 9, p. 3188.

[83] Theodorakakos A., Ous T., Gavaises M., Nouri J., Nikolopoulos N., and Yanagihara H. (2006) 'Dynamics of water droplets detached from porous surfaces of relevance to pem fuel cells', *Journal of Colloid and Interface Science*, vol. 300, pp. 673–687.

[84] Zhu X., Sui P., and Djilali N. (2007) 'Dynamic behaviour of liquid water emerging from a gdl pore into a pemfc gas flow channel', *Journal of Power Sources*, vol. 172, pp. 287–295.

[85] Zhu X., Sui P., and Djilali N. (2008) 'Three-dimensional numerical simulations of water droplet dynamics in a pemfc gas channel', *Journal of Power Sources*, vol. 181, pp. 101–115.

[86] Ahmadlouydarab M. and Feng J.J. (2014) 'Motion and coalescence of sessile drops driven by substrate wetting gradient and external flow', *Journal of Fluid Mechanics*, vol. 746, pp. 214–235.

[87] Dimitrakopoulos P. and Higdon J.J. (1997) 'Displacement of fluid droplets from solid surfaces in low-reynolds-number shear flows', *Journal of Fluid Mechanics*, vol. 336, pp. 351–378.

[88] Huang J., Huang H., and Wang X. (2014) 'Numerical study of drop motion on a surface with stepwise wettability gradient and contact angle hysteresis', *Physics of Fluids*, vol. 26, p. 062101.

[89] Zu Y.Q. and Yan Y.Y. (2011) 'Lattice boltzmann method for modelling droplets on chemically heterogeneous and microstructured surfaces with large liquidgas density ratio', *Journal of Applied Mathematics*, vol. 76, pp. 743–760.

[90] Randive P. and Dalal A. (2015) 'Influence of geometry on mobilization of trapped blob', *European Journal of Mechanics B/Fluids*, vol. 53, pp. 1–10.

[91] Lamorgese A. and Mauri R. (2015) 'Buoyancy-driven detachment of a wall-bound pendant drop:interface shape at pinchoff and nonequilibrium surface tension', *Physical Review E*, vol. 92, p. 032401.

[92] Tilehboni S.M., Fattahi E., Afrouzi H.H., and Farhadi M. (2015) 'Numerical simulation of droplet detachment from solid walls under gravity force using lattice boltzmann method', *Journal of Molecular Liquids*, vol. 212, pp. 544–556.

[93] Cossali G.E., Coghe A., and Marengo M. (1999) 'The impact of a single drop on a wetted solid surface', *Experiments in Fluids*, vol. 22, pp. 463–472.

[94] Yarin A.L. and Weiss D.A. (1995) 'Impact of drops on solid surfaces: Self-similar capillary waves and splashing as a new type of kinematics discontinuity', *Journal of Fluid Mechanics*, vol. 283, pp. 141–173.

[95] Weiss D.A. and Yarin L.A. (1999) 'Single drop impact onto liquid films neck distortion, jetting, tiny bubble entrainment, and crown formation', *International Journal of Fluid Mechanics*, vol. 385, pp. 229–254.

[96] Cossali G.E., Coghe A., Marengo M., and Zhdanov S. (2004) 'The role of time in single drop splash on thin film', *Experiments in Fluids*, vol. 22, pp. 888–900.

[97] Mukherjee S. and Abraham J. (2007) 'Crown behavior in drop impact on wet walls', *Physics of Fluids*, vol. 19, p. 052103.

[98] Shetabivash H., Ommi F., and Heidarinejad G. (2014) 'Numerical analysis of droplet impact onto liquid film', *Physics of Fluids*, vol. 26, p. 012102.

[99] Zhbankova S.L. and Kolpakov A.V. (1990) 'Collision of water drops with a plane water surface', *Fluid Dynamics*, vol. 25, pp. 470–473.

[100] Okawa T., Shiraishi T., and Mori T. (2008) 'Effect of impingement angle on the outcome of single water drop impact onto a plane water surface', *Experiments in Fluids*, vol. 44, pp. 331–339.

[101] Ray B., Biswas G., and Sharma A. (2012) 'Oblique drop impact on deep and shallow liquid', *Experiments in Fluids*, vol. 11, pp. 1386–1396.

[102] Cheng M. and Lou J. (2015) 'A numerical study on splash of oblique drop impact on wet walls', *Computers and Fluids*, vol. 115, pp. 11–24.

[103] Rhie C.M. and Chow W.L. (1983) 'Numerical study of the turbulent flow past an airfoil with trailing edge seperation', *AIAA Journal*, vol. 21, pp. 1525–1532.

[104] `www.ssisc.org/lis`.

[105] Ku H.C., Hirsh R.C., and Taylor T. (1987) 'A pseudospectral method for solution of the three-dimensional incompressible Navier-Stokes equation', *Journal of Computational Physics*, vol. 70, pp. 439–462.

[106] Biswas G., Breuer M., and Durst F. (2004) 'Backward-facing step flows forvarious expansion ratios at low and moderate reynolds numbers', *ASME Juornal of Fluids Engineering*, vol. 126, pp. 362–374.

[107] Zalesak S. (1979) 'Fully multi-dimensional flux corrected transport algorithm for fluid flow', *Journal of Computational Physics*, vol. 31, pp. 335–362.

[108] Rider W.J. and Kothe D.B. (1998) 'Reconstructing volume tracking', *Journal of Computational Physics*, vol. 141, pp. 112–152.

[109] Ubbink O. (1997) 'Numerical prediction of two fluid systems with sharp interfaces', *Ph.D. Thesis, Imperial College of Science, Technology and Medicine.*

[110] Gerlach D., Tomar G., Biswas G., and Durst F. (2006) 'Comparison of volume-of-fluid methods for surface tension-dominant two-phase flows', *International Journal of Heat and Mass Transfer*, vol. 49, pp. 740–754.

[111] Tsui Y.Y. and Pan Y.F. (2006) 'A pressure-correction method for incompressible flows using unstructured meshes', *Numerical Heat Transfer, Part B*, vol. 49, pp. 43–65.

[112] Kleefsman K., Fekken G., Veldman A., Iwanowski B., and Buchner B. (2005) 'A volume-of-fluid based simulation method for wave impact problems', *Journal of Computational Physics*, vol. 206, pp. 363–393.

[113] Mokos A., Rogers B.D., Stansby P.K., and Dominguez J.M. (2015) 'Multi-phase sph modelling of violent hydrodynamics on gpus', *Computer Physics Communications*, vol. 196, pp. 304–316.

[114] Dumbser M. (2013) 'A diffuse interface method for complex three-dimensional free surface flows', *Computer Methods in Applied Mechanics and Engineering*, vol. 257, pp. 47–64.

[115] Ramirez J.M.C., Cruz J.R., Vazquez M.S., Rodriguez W.V., Espinosa E.M., and Cortes C.L. (2016) 'Efficient two-phase mass-conserving level set method for simulation of incompressible turbulent free surface flows with large density ratio', *Computers and Fluids*, vol. 136, pp. 212–227.

[116] Marsooli R. and Wu W. (2014) '3-d finite-volume model of dam-break flow over uneven beds based on vof method', *Advances in Water Resources*, vol. 70, pp. 104–117.

[117] Larese A., Rossi R., Onate E., and Idelsohn S.R. (2014) 'Validation of the particle finite element method (pfem) for simulation of free surface flows', *Engineering Computations*, vol. 25, pp. 385–425.

[118] Park I.R., Kim K.S., Kim J., and Van S.H. (2009) 'A volume-of-fluid method for incompressible free surface flows', *International Journal for Numerical Methods in Fluids*, vol. 61, pp. 1331–1362.

[119] Lins E.F., Elias R.N., Rochinha F.A., and Coutinho A.L.G.A. (2010) 'Residual-based variational multiscale simulation of free surface flows', *Computational Mechanics*, vol. 46, pp. 545–557.

[120] Golay F., M.Ersoy, Yushchenko L., and Sous D. (2015) 'Block-based adaptive mesh refinement scheme using numerical density of entropy production

for three-dimensional two-fluid flows', *International Journal of Computational Fluid Dynamics*, vol. 29, pp. 67–81.

[121] Young N.O., Goldstein J.S., and Block M.J. (1959) 'The motion of bubbles in a vertical temperature gradient', *Journal of Fluid Mechanics*, vol. 6, pp. 350–356.

[122] Herrmann M., Lopez J.M., Brady P., and Raessi M. (2008) 'Thermocapillary motion of deformable drops and bubbles', *in: Center for Turbulence Research Proceedings of the Summer Program*, vol. 155.

[123] Štrubelj L., Tiselj I., and Mavko B. (2009) 'Simulations of free surface flows with implementation of surface tension and interface sharpening in the two-fluid model', *International Journal of Heat and Fluid Flow*, vol. 30, pp. 741–750.

[124] Renardy M., Renardy Y., and Li J. (2001) 'Numerical simulation of moving contact line problems using a volume-of-fluid method', *Journal of Computational Physics*, vol. 171, pp. 243–263.

[125] Salih A. (2007) *Numerical simulation of two-fluid flows with sharp interfaces using level set method*, Phd thesis, Indian Institute of Technology, Kharagpur, Kharagpur, India.

[126] OpenFOAM, The Open Source CFD Toolbox, User Guide Version 2.3.0, `www.openfoam.org`.

[127] Fawehinmi B., Gaskell P.H., Jimack P., Kapur N., and Thompson H.M. (2005) 'A combined experimental and computational fluid dynamics analysis of the dynamics of drop formation', *Journal of Mechanical Engineering Science*, vol. 219, pp. 933–948.

[128] Raman K., Jaiman R., Lee T., and Low H. (2015) 'On the dynamics of crown structure in simultaneous two droplets impact onto stationary and moving liquid film', *Computers and Fluids*, vol. 107, pp. 285–300.

List of Publications

Journal

- **J. Manik**, A. Dalal and G. Natarajan, "A generic algorithm for three-dimensional multi-phase flows on unstructured meshes"submitted after first review to International Journal of Multiphase Flows.
- **J. Manik**, A. Dalal and G. Natarajan, "A parametric study on the droplet detachment process from the ceiling under the effect of gravity"submitted after second review to European Journal of Mechanics B/Fluids
- **J. Manik**, A. Dalal and G. Natarajan, "A generic well balanced algorithm for incompressible flows on unstructured meshes"to be submitted to Journal of Computational Physics.
- **J. Manik**, A. Dalal and G. Natarajan, "Numerical simulation of droplet splashing over varying thin liquid film"under preparation.

International conference

- **J. Manik**, M. Parmananda, A. Dalal and G. Natarajan, 2013 "Development of 3-D Navier-Stokes Solver Over a Hybrid Unstructured Grid"22nd National and 11th International ISHMT-ASME Heat and Mass Transfer Conference, IIT Kharagpur, India
- S. Dusad, **J. Manik**, A. Dalal and G. Natarajan, 2014 "Evaluating Turbulence Model on Hybrid Unstructured Meshes for Wall Bounded Flows"5th International and 41st National Conference on Fluid Mechanics and Fluid Power, IIT Kanpur, India
- A. Dalal, **J. Manik** and G. Natarajan, 2016, "Numerical Simulation of Droplet Splashing Over Varying Thin Liquid Film", The 69th Annual Meeting of The American Physical Society - Division of Fluid Dynamics (Fall), Portland, OR, USA. (Oral Presentation Only)

- A. Dalal, A. Kulkarni, **J. Manik** and G. Natarajan, 2016, "A Parametric Study on the Rise of a Pair of Bubbles Using Algebraic Volume of Fluid Method: Effect of Diameter and Viscosity Ratio", The 69th Annual Meeting of The American Physical Society - Division of Fluid Dynamics (Fall), Portland, OR, USA. (Oral Presentation Only)

- **J. Manik**, M. Parmananda, S. Kotoky, P. Borgohain, A. Dalal and G. Natarajan, 2017, "Lessons from Anupravaha: Towards a General Purpose Computational Framework on Hybrid Unstructured Meshes for Multi-Physics Applications", Paper No. CHT-17-209, ICHMT International Symposium on Advances in Computational Heat Transfer, Napoli, Italy

Book chapter

- A. Bajpai, **J. Manik**, M. Parmananda, A. Dalal, G. Natarajan, "Computation of Variable Density Flows on Hybrid Unstructured Grids"Fluid Mechanics and Fluid Power Contemporary Research, 09/2017: pages 431-437; ISBN: 978-81-322-2741-0, DOI:10.1007/978-81-322-2743-4_41

- **J. Manik**, A. Dalal, G. Natarajan, "A Hybrid Grid Based Algebraic Volume of Fluid Method for Interfacial Flows"Fluid Mechanics and Fluid Power Contemporary Research, 09/2017: pages 1111-1119; , ISBN: 978-81-322-2741-0, DOI:10.1007/978-81-322-2743-4_105